Topological $\mathbf{k} \cdot \mathbf{p}$ Hamiltonians and their applications to uniaxially strained Mercury telluride

Dissertation
zur Erlangung des akademischen Grades
Doctor rerum naturalium
(Dr. rer. nat.)

vorgelegt von

Dipl.-Phys.
Frank Kirtschig
geboren am 02.10.1987 in Dresden

Institut für Theoretische Physik
Technische Universität Dresden

Institut für Theoretische Festkörperphysik
Leibniz-Institut für Festkörper- und Werkstoffforschung Dresden

2017

Eingereicht am 31. Januar 2017

Gutachter:	
Prof. Dr. Jeroen van den Brink	(Universitätsprofessor TU Dresden)
Dr. Carmine Ortix	(Universitair Docent Universiteit Utrecht)

Le savant n'étudie pas la nature parce que cela est utile, il l'étudie parce qu'il y prend plaisir et il y prend plaisir parce qu'elle est belle. – Jules Henri Poincaré, Science et méthode (1908).

Overview

Topological insulators (TIs) are new states of quantum matter that have fundamentally challenged our knowledge of insulators and metals. They are insulators in the bulk, but metallic on the edge. A TI is characterized by a so-called topological invariant. This characteristic integer number is associated to a mapping between two topological spaces and can be safely defined in lattice models of electronic systems. Due to the bulk-edge correspondence a non-trivial value of the topological invariant leads to topologically protected edge or surface states. To get insight into the electronic characteristics of these edge/surface states, however, an effective continuum theory is often needed. In this thesis we will address the suitability of continuum low-energy theories to describe both the topological bulk properties and the surface state characteristics of TIs. The models which are topologically well-defined are called topological $\mathbf{k}\cdot\mathbf{p}$ Hamiltonians. After introducing a necessary background in chapter 1 and 2, we will discuss in the methodological chapter 3 the strategies that have to be taken into account to study the presence of topological surface states when using the topological $\mathbf{k}\cdot\mathbf{p}$ Hamiltonians. In chapter 4 we will study two different model classes associated to a spherical basis manifold. Both have an integer topological invariant, but one shows a marginal bulk-edge correspondence. In chapter 5 we will study a different continuum theory where the basis manifold corresponds to a hemisphere. We then apply all these ideas to a time-reversal invariant TI – uniaxially strained Mercury Telluride (HgTe). We determine the spin textures of the topological surface states of strained HgTe using their close relations with the mirror Chern numbers of the system and the orbital composition of the surface states. We show that at surfaces with symmetry lower than C_{2v}, an increase in the strain magnitude triggers a topological phase transition where the winding number of the surface state spin texture is flipped while the four topological invariants characterizing the bulk band structure are unchanged. In the last chapter we will give a summary.

Contents

1 Introduction

Topology is a mathematical field related to geometry which concerns with the properties of space that are preserved under continuous deformations [1]. A topological space is simply a space of points (position x or momentum p) with a canonical metric measuring the distance between them. Topology comes into play by considering the two fundamental properties of these spaces: *connectness* and *compactness*. The first one describes whether the space consists of two or more separated subspaces. The other property describes whether there are boundaries or not. The most important implication is that one can associate to the mappings between topological spaces *topological invariants*. Mathematical examples are the compact manifolds which can be classified topologically according to their genus. This number does not change under invertible transformations, excluding *tearing* and *gluing* processes. This *homeomorphism* is a function from one topological space to another where the inverse image of any element is again an element of the same topological space. In many physical situations this is satisfied and thus topology has journeyed from the purely mathematical arena to feature in nearly all fields of physics. In particular, the discovery of topological insulators (TIs) has disclosed a new state of quantum matter that has a tremendous impact in the field of condensed matter physics with potential applications in *quantum computation* and *spintronics* [2]. TIs are bulk insulators with a conducting surface. The surface carriers are Dirac particles with an energy which increases linearly with momentum. These metallic edge states are topologically protected against generic perturbations preserving the bulk symmetries of the underlying topological class and the intrinsic insulating behavior. The robustness of these metallic edge states is encoded precisely in a topological invariant classifying the ground state of the insulating system.

With non-interacting lattice Hamiltonians at work, the band structure of an insulator can be viewed as a mapping from the periodic Brillouin zone, which has the topology of a torus $\mathcal{T}^d$ in d-dimensions to the space of Bloch Hamiltonians with an energy gap. It is this mapping that generally allows for the definition of a topological invariant in an insulating system.

Combining the idea of topology and an effective low-energy continuum description of an insulating system is the subject we want to deal in this thesis. However, there is a hidden

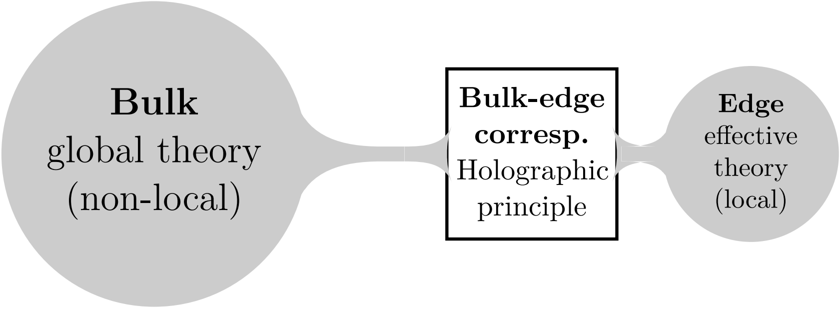

Figure 1.1: Illustration of the holographic principle connecting the theory on the edge with the bulk theory.

dichotomy in this idea which is quite important. On the one hand we can write down a generalized *low-energy theory* as an expansion of the momentum p_j

$$H = A + \sum_i B_i \hat{p}_i + \sum_{i \leq j} C_{ij} \hat{p}_i \hat{p}_j + ..., \tag{1.1}$$

where the structure of the matrices A, B, C collects the internal degree of freedoms. This is an expansion around a local minimum. On the other hand, we destroy the non-local topological features from the underlying theory since the compact manifold turns into the non-compact plane. At a first sight, topology needs information up to an infinite order.

The presence of edge states can be instead well described by such a local low-energy continuum theory. In other words, the defining property of topological insulating states of matter can be well described by a local theory but its existence can be only predicted by a non-local bulk theory. The non-local (bulk) and the local (edge) description are related by a *holographic principle* similarly to the *AdS/CFT correspondence* combining general relativity and quantum field theory. Here we find an equivalence between the bulk theory and the physically relevant edge part. This is the so-called *bulk-edge correspondence* [3, 4] (illustrated in Fig. 1.1) which is a one-to-one correspondence between the bulk topological invariant and its local (most Dirac-like) Hamiltonian on the boundary or surface with a topologically trivial material.

We are going to highlight the idea of topological $\mathbf{k} \cdot \mathbf{p}$ Hamiltonians. This means we want to study under which circumstances it is possible to use a continuum treatment to understand the underlying edge physics from an approximate bulk theory. These continuum theories are local in the sense of describing the low-energy bulk excitations around a local minimum of the band gap, but they have to be global in a topological sense ensuring a well-defined mapping.

2 Topological states of matter

Research in the interdisciplinary field of topology and physics is quite old and started already in the beginning of the twentieth century [5]. However, the hype of *Topological states of matter* started in the 80's. Before this, it was commonly believed that the existence of an energy gap uniquely defines an insulating ground state. Therefore, it was quite surprising that one could find new properties associated to insulating states/phases, which distinguish them. These new properties are stored in a *global* (and *topological*) quantity, in contrast to Landau's conventional theory of a *local* order parameter distinguishing phases with different symmetries. This additional concept had a huge impact in the physics community – especially in condensed matter physics – and lead to the discovery of *topological insulators* (TIs). The fundamental property of a TI is the presence of (gapless) boundary or edge excitations: only the bulk is truly insulating and the number of *topologically protected* edge states corresponds directly to a global bulk topological invariant via the *bulk-edge correspondence*. This *topological invariant* does not change if one smoothly deforms the system without destroying its symmetries and/or closing the gap.

The most important symmetries are the three *discrete* symmetries: $\mathcal{C} = \mathcal{P}\mathcal{T}$ sublattice/chiral symmetry, $\mathcal{P}$ charge conjugation/particle-hole symmetry and $\mathcal{T}$ time reversal symmetry. Let us consider a general Hamiltonian of fermions *without interactions*

$$\mathcal{H} = \sum_{\alpha\beta} \hat{\psi}_\alpha^\dagger H_{\alpha\beta} \hat{\psi}_\beta = \hat{\Psi}^\dagger H \hat{\Psi}, \tag{2.1}$$

where $\hat{\Psi}$ is a spinor collecting all N fermionic annihilation operators $\hat{\psi}_\alpha$ in a vector form. The parameters α, β are multi-indices for all degrees of freedom of the system, such as spin, orbital and sublattice degrees of freedom. The fermionic operators fulfill the anti-commutator relations

$$\{\hat{\psi}_\alpha, \hat{\psi}_\beta\} = 0 \text{ and } \{\hat{\psi}_\alpha, \hat{\psi}_\beta^\dagger\} = \delta_{\alpha\beta}. \tag{2.2}$$

The important point is that this relation connects the second-quantized Hamiltonian $\mathcal{H}$ with a first-quantized (or single-particle) one H. This also affects the three generic symmetries which can commute with the second-quantized Hamiltonian. The fermionic character together with the antiunitary and unitary representation of the symmetry operators lead then to

$$\{\mathcal{C}, H\} = 0,\ \{\mathcal{P}, H\} = 0 \text{ and } [\mathcal{T}, H] = 0 \tag{2.3}$$

on the first-quantized level. One can show that they have to square as [6]

$$\mathcal{C}^2 = +1,\ \mathcal{P}^2 = \pm 1 \text{ and } \mathcal{T}^2 = \pm 1. \tag{2.4}$$

This gives the possibility to distinguish all Hamiltonians in a *tenfold way*, originally found in the random matrix approach of Altland and Zirnbauer [7], by the signature $(\mathcal{C}^2, \mathcal{P}^2, \mathcal{T}^2)$ (see Tab. 2.1). In a lattice-periodic system described by the reciprocal lattice vectors $\mathbf{G}$ the relations above change to

$$\mathcal{C}_{\mathbf{k}} H(+\mathbf{k}) = -H(+\mathbf{k})\mathcal{C}_{\mathbf{k}}, P_{\mathbf{k}} H(+\mathbf{k})^* = -H(-\mathbf{k}) P_{\mathbf{k}} \text{ and } T_{\mathbf{k}} H(+\mathbf{k})^* = +H(-\mathbf{k}) T_{\mathbf{k}}, \tag{2.5}$$

where we used the definitions $\mathcal{P}_{\mathbf{k}} = P_{\mathbf{k}}\mathcal{K}$ and $\mathcal{T}_{\mathbf{k}} = T_{\mathbf{k}}\mathcal{K}$, with $\mathcal{K}$ the complex conjugation. The definition of time reversal and particle-hole symmetry allows to construct the chiral operator as $\mathcal{C}_{\mathbf{k}} \propto P_{-\mathbf{k}} T^*_{\mathbf{k}}$ up to a phase. A unitary change of the Hamiltonian: $\tilde{H}(\mathbf{k}) = U(\mathbf{k})^\dagger H(\mathbf{k}) U(\mathbf{k})$, leads then to the following transformation of the discrete symmetry operators

$$\mathcal{C}_{\mathbf{k}} = U(\mathbf{k})^\dagger \tilde{\mathcal{C}}_{\mathbf{k}} U(\mathbf{k}), P_{\mathbf{k}} = U(-\mathbf{k})^\dagger \tilde{P}_{\mathbf{k}} U(\mathbf{k})^* \text{ and } T_{\mathbf{k}} = U(-\mathbf{k})^\dagger \tilde{T}_{\mathbf{k}} U(\mathbf{k})^*. \tag{2.6}$$

An important consequence of this is that a unitary transformation leaves the triple of the signs of the squares of $\mathcal{C}_{\mathbf{k}}$, $\mathcal{P}_{\mathbf{k}}$ and $\mathcal{T}_{\mathbf{k}}$ invariant. However, the unitary transformation can introduce an explicit $\mathbf{k}$ dependence in the symmetry operators. To have a $\mathbf{k}$-independent definition of the symmetry operators, one generally has to find a proper lattice-periodic unitary operation. If this is possible while leaving the Hamiltonian in the *Bloch*-form $H_{\mathbf{k}+\mathbf{G}} = H_{\mathbf{k}}$, the model has $\mathcal{C}$-, $\mathcal{P}$- and/or $\mathcal{T}$-symmetry.

Symmetry-protection is one aspect of topological phases. Another one is the insulating behavior of the fermionic system. For insulators it is possible to distinguish bands (or band bundles) from each other over a *basis manifold*. These are the occupied bands and the non-occupied bands, and the manifold is the Brillouin zone (BZ) , which has the shape of a torus. However, one can extend this argument. One can adiabatically transform the band structure of an insulating system to a metallic system with electron and hole pockets

Table 2.1: Part of the *periodic table of topological insulators and superconductors* [3]. The first column contains the names of the symmetry classes of disordered system after Altland and Zirnbauer [8, 7]. The second column indicates the signature of the three discrete symmetries. The absence of a symmetry is marked by a zero. The last column contains the possible topological indices with respect to the dimension $d = 1, 2, 3$ where $\mathbb{Z}$ are the integers and $\mathbb{Z}_2 = \{0, 1\}$. The classes $2\mathbb{Z}$ indicate even integers .

classes	symmetries			dimensions		
	$\mathcal{C}$	$\mathcal{P}$	$\mathcal{T}$	1	2	3
A	0	0	0	0	$\mathbb{Z}$	0
AIII	1	0	0	$\mathbb{Z}$	0	$\mathbb{Z}$
AI	0	0	+1	0	0	0
BDI	1	+1	+1	$\mathbb{Z}$	0	0
D	0	+1	0	$\mathbb{Z}_2$	$\mathbb{Z}$	0
DIII	1	+1	−1	$\mathbb{Z}_2$	$\mathbb{Z}_2$	$\mathbb{Z}$
AII	0	0	−1	0	$\mathbb{Z}_2$	$\mathbb{Z}_2$
CII	1	−1	−1	$2\mathbb{Z}$	0	$\mathbb{Z}_2$
C	0	−1	0	0	$2\mathbb{Z}$	0
CI	1	−1	+1	0	0	$2\mathbb{Z}$

sitting at different $\mathbf{k}$-points in the BZ via a warping. A warping is a change in the band structure such that there exists a finite energy difference between the two band bundles at each individual $\mathbf{k}$-point in the BZ. In other words the system has local (direct) gaps but does not have a full bulk band gap. This property of a system which we denote as the *warping gap* condition, allows to define a topological homotopy transformation between an insulator and a metal. The response of such a metallic system in an experiment, such as a Hall conductivity measurement, will be an overlap of the topologically induced edge contribution and bulk states contribution. Independently of that concern, there are methods such as ARPES measurements where such an extension is appropriate.

Topology allows us now to characterize all mappings between the basis manifold and the target manifold presented by the band bundles. This can be simply the number of occupied states, a winding number, a Chern number and so on, but it is always a topological invariant. For the three discrete symmetries, the topologically distinguishable classes are presented in Tab. 2.1 for dimensions $d = 1, 2, 3$. Schnyder et al. [9], Kitaev [3], and Ryu et al. [10] provided a classification in all dimensions according to the three generic symmetries of the ten *Altland-Zirnbauer* (AZ) classes [7], and found five different topologically non-trivial classes in any dimension.

In this chapter we will study selected TI models and touch upon the idea of effective models to describe them.

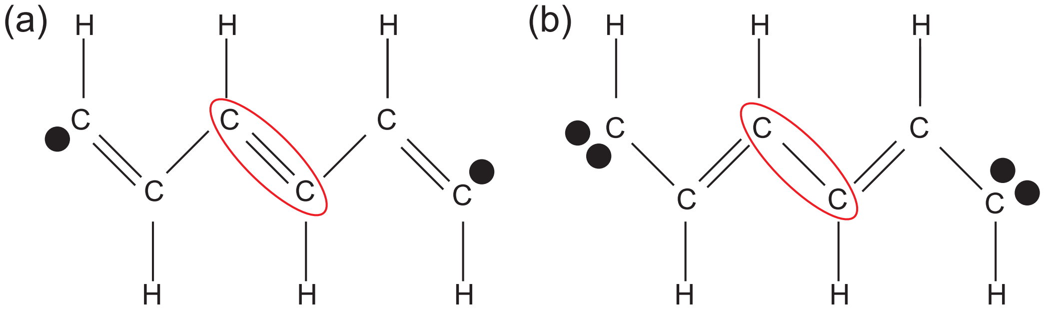

Figure 2.1: The two different topological insulating phases $\delta t > 0$ and $\delta t < 0$ of the SSH model are shown in (a) and (b) respectively. The Cs are the carbon atoms, whereas H represent hydrogen atoms using Lewis dot structures.

2.1 The SSH model and the Jackiw-Rebbi solution

The Su-Schrieffer-Heeger (SSH) model is the simplest example of a TI. It is a tight-binding (TB) model for a one-dimensional dimerized atomic chain originally introduced by Su, Schrieffer, and Heeger in 1979 to describe the organic polymer *polyacetylene*: an atomic chain of carbon atoms with alternating single and double bonds [11]. Fig. 2.1 illustrates such an open chain (unit cells $L = 3$) using the Lewis structure notation.

The SSH model is a realization of a spinless fermionic one-dimensional insulator belonging to the symmetry class BDI of the Altland-Zirnbauer classification. It indeed possesses time-reversal, particle-hole, and consequently chiral symmetry. Indicating with A and B the two atom basis of the lattice, the tight-binding Hamiltonian for L unit cells in real space can be written as

$$\mathcal{H} = -\sum_{i=1}^{L}\left[(t+\delta t)c^{\dagger}_{A,i}c_{B,i} + (t-\delta t)c^{\dagger}_{A,i+1}c_{B,i}\right] + h.c., \tag{2.7}$$

where $c^{\dagger}_{A/B,i}$, $c_{A/B,i}$ are operators creating and annihilating, respectively, an electron on the A and B sublattice at the i-th unit cell. In addition, *h.c.* stands for the hermitian-conjugate of the the first part of the Hamiltonian. The parameter $t > 0$ describes the homogeneous hopping amplitude, while δt is a dimerization term which can be positive or negative, but small as compared to t ($|\delta t| \ll t$). By choosing *periodic boundary conditions* (PBC), *i.e.* $c^{\dagger}_{A,L+1} = c^{\dagger}_{A,1}$ and $c^{\dagger}_{B,L+1} = c^{\dagger}_{B,1}$, we can express the Hamiltonian in momentum space by defining the Fourier transformed operators

$$c_{A/B,k} = \frac{1}{\sqrt{N}}\sum_{j=1}^{L} c_{A/B,j}e^{-ikaj}, \tag{2.8}$$

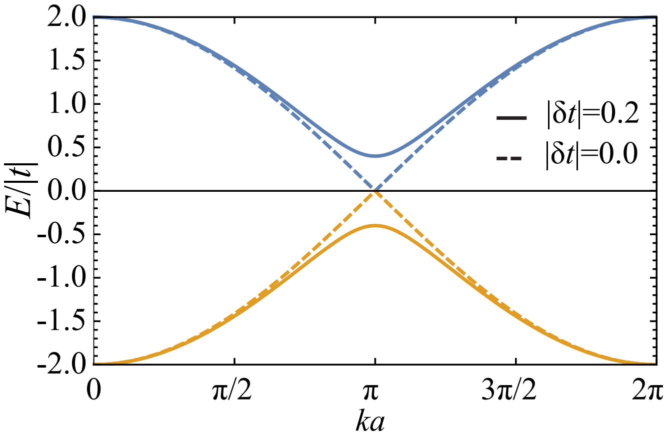

Figure 2.2: The bulk spectrum of the SSH model is plotted for different values of $|\delta t|$. At $\delta t = 0$ we find a gap-closing point at $ka = \pi$ which separates two different topologically insulating regimes.

where a is the lattice constant. By further using the *spinor* notation $\Psi_k^\dagger = \{c_{A,k}^\dagger, c_{B,k}^\dagger\}$, the Hamiltonian can be recast in the form $\mathcal{H} = \sum_{k\in BZ} \Psi_k^\dagger H(k)\Psi_k$ with the BZ $(-\pi/a, \pi/a]$, which has the topology of a one-dimensional circle $\mathbb{S}_1$. The 2×2 hermitian matrix $H(k)$ instead reads

$$H(k) = h_x(k)\sigma_x + h_y(k)\sigma_y, \tag{2.9}$$

where we introduced the usual *Pauli matrices* σ_i defined in the appendix (A), and

$$h_x(k) = -(t+\delta t) - (t-\delta t)\cos(ka)\ ,\ h_y(k) = -(t-\delta t)\sin(ka). \tag{2.10}$$

The energy spectrum of the SSH model then consists of two-bands with dispersion relation $E_\pm = \pm\sqrt{h_x^2(k)+h_y^2(k)} = \pm\sqrt{2(t^2+\delta t^2)+2(t^2-\delta t^2)\cos(ka)}$. It has a full band-gap except for $\delta t = 0$, in which case the gap closes at the BZ edge $k = \pi/a$. The spectrum is plotted in Fig. 2.2.

As one can see, the sign of the dimerization term has no effect on the spectrum. However, as we next show, $\delta t > 0$ and $\delta t < 0$ represent two topologically distinguishable states, with their difference encoded in the structure of the eigenstates $|E_\pm\rangle$.

It is important to notice that topology comes into play because of the presence of the *chiral symmetry*. Since the latter is represented by σ_z, the chiral symmetry implies the anticommutation relation: $\{\sigma_z, H(k)\} = 0$. This also implies that, as found in Eq. (2.9), a generic Hamiltonian in the BDI class is defined by the form of the coefficients (h_x, h_y) of a two-dimensional vector in the $\sigma_{x,y}$ space.

A general mapping $f : BZ \to |E_-\rangle$ characterizing the lowest energy band of a system can

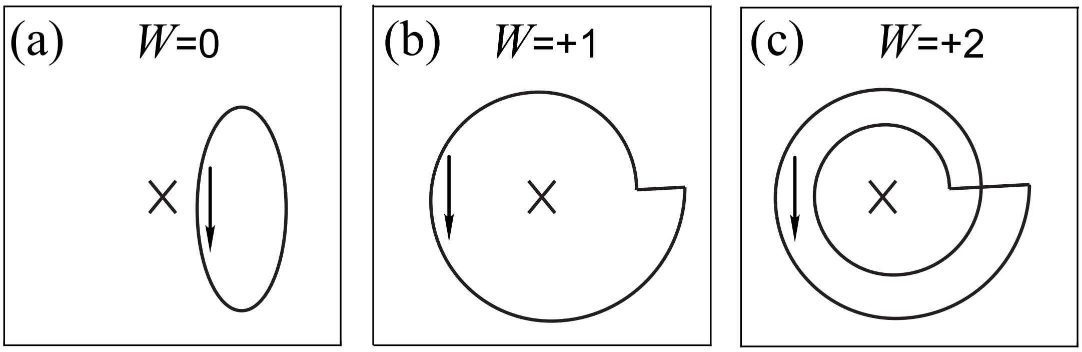

Figure 2.3: The winding number W counts how many times a closed path goes around the point $(0,0)$ representing the gap-closing point. The reason why all paths do not cross the center is the insulating behavior of this system with chiral symmetry. The winding number is integer.

be then written as a mapping $f' : BZ \to \mathbb{R}^2 \backslash \{(0,0)\}$ where the point $(0,0)$ corresponds to a gap closing point in the BZ. For an insulating system, this point cannot be present demonstrating that a generic insulating Hamiltonian with chiral symmetry is specified by a vector (h_x, h_y) living on a two-dimensional space with an excluded origin $(0,0)$.

We can now associate to every point in the space $\mathbb{R}^2 \backslash \{(0,0)\}$ a point on the circle (or 1-sphere) $\mathbb{S}_1$ using the transformation

$$(\hat{h}_x, \hat{h}_y) := \frac{1}{\sqrt{h_x^2 + h_y^2}} (h_x, h_y) \in \mathbb{R}^2 \text{ or } \hat{h} := \frac{h_x + i h_y}{|h_x + i h_y|} \in \mathbb{C}, \tag{2.11}$$

where in the latter formula we used the complex number space $\mathbb{C}$ such that $\hat{h} \in U(1)$. This transformation leads finally to a mapping $f'' : BZ \simeq \mathbb{S}_1 \to U(1) \simeq \mathbb{S}_1$ between two one-dimensional spheres, which, precisely as f, is a mapping between the BZ and the lowest energy band. The transformation we adopted is called an homotopy transformation, which simplified the geometry of the target space but leaves the topology unchanged.

The advantage of f'' is that one can naturally relate to this mapping a *winding number* W. This number counts how many times the path $\mathbb{S}_1$ of the BZ goes around the origin $(0,0)$ as illustrated in Fig. 2.3.

It can be derived using the formulation of the mapping in the complex plane and defining the *multivalued* logarithm $\log \hat{h} = i(\arg h + 2\pi n)$. We indeed have

$$W = \frac{1}{2\pi i} \int_{-\pi/a}^{+\pi/a} dk \frac{d}{dk} \log h(k). \tag{2.12}$$

For the SSH model we find either $|W| = 1$ for $\delta t < 0$ (non-trivial) or $W = 0$ for $\delta t > 0$

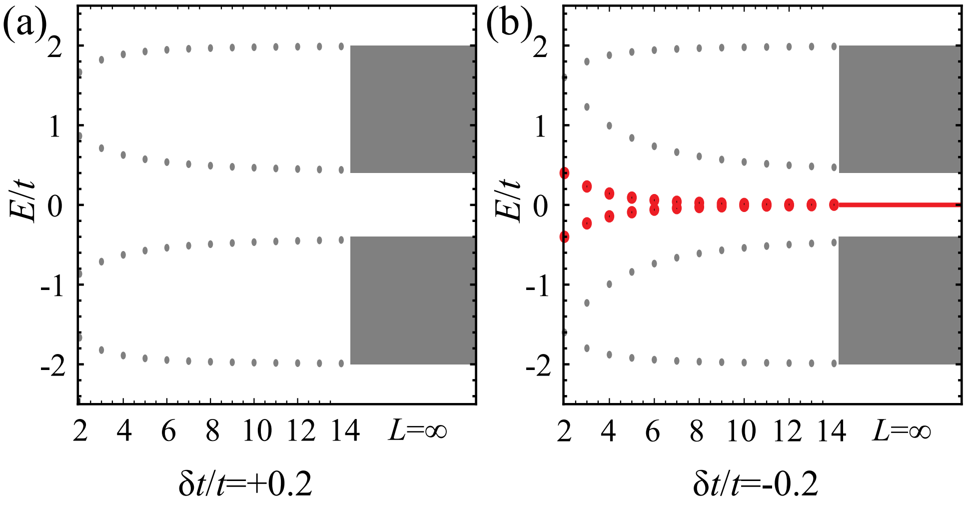

Figure 2.4: The spectrum of the TB Hamiltonian is shown for different system sizes L and $t > 0$. For small L we show only the band edges (gray) and the edge states (red), while in the infinite limit we plot the full spectrum. The two edge states are degenerate at $E = 0$ in the limit $L \to \infty$.

(trivial). To come from one chiral system to the other we have to close the gap or break the chiral symmetry. Without these changes this number is fixed. It is a *topological* quantity. It must be clear that this topological consideration only works due to the periodic arrangement in an infinite large system ($L \to \infty$) to have a continuous and compact **k** space. Going now to a finite system one can ask what are the consequences of the topological properties in the bulk.

For an open chain, the momentum k is no longer a good quantum number. Let us consider the corresponding TB model with an integer number of unit cells L. Fig. 2.4 shows the energy levels of the TB Hamiltonian with respect to L, which consists of two parts. The first part represents states of the so-called projected bulk spectrum. These states are given in the energy interval: $2|\delta t| < |E| < 2t$. The topologically non-trivial property has a physical consequence in the second part. For $\delta t < 0$ one finds zero-energy edge states which are not present for $\delta t > 0$. This is a manifestation of the *bulk-edge correspondence*. The presence of zero energy end states can be also studied using the low-energy continuum theory. The SSH model is the simplest example where we can use this technique. For this model the low-energy excitations are close to $k = \pi$ for $|\delta t|/t \ll 1$ and $a = 1$. Starting an expansion around this point up to the second-order gives us the effective Hamiltonian

$$H(\pi + k) = v_F k \sigma_y + m(k)\sigma_x + \mathcal{O}(k^3), \tag{2.13}$$

where the Fermi velocity $v_F = t - \delta t > 0$ and the mass term $m(k) = M - Bk^2$ with

$M = -2\delta t$ and $B = (t + \delta t)/2 > 0$. One can simply show that the application of the winding number definition to this approximate model leads to the winding number $W = (1 - \mathrm{sign}(\delta t))/2$ by integrating from $-\infty$ to $+\infty$ instead over the BZ. This winding number is now exactly the same as the one of the lattice model but without a momentum cutoff. It implies that the lattice structure of the SSH Hamiltonian is not essential in order to have an integer topological invariant. This is also reflected in the presence of zero-energy states. By substituting $k \to p_x = -i\partial_x$ in Eq. 2.13 and solving the Schrödinger equation for the half-line $x > 0$, one finds a zero energy evanescent wave

$$\Psi(x) \propto e^{-\frac{v_F}{2B}x} \left(e^{+\sqrt{\left(\frac{v_F}{2B}\right)^2 - \frac{M}{B}}x} - \frac{\nu e^{i\phi} + \sqrt{\left(\frac{v_F}{2B}\right)^2 - \frac{M}{B}}}{\nu e^{i\phi} - \sqrt{\left(\frac{v_F}{2B}\right)^2 - \frac{M}{B}}} e^{-\sqrt{\left(\frac{v_F}{2B}\right)^2 - \frac{M}{B}}x} \right) \begin{pmatrix} 1 \\ 0 \end{pmatrix} \tag{2.14}$$

for $M > 0$ using boundary conditions respecting the chiral symmetry

$$\left(i\sigma_x\partial_x + \frac{v_F}{2B}\sigma_y + i\nu(\cos\phi\sigma_x + \sin\phi\sigma_y) \right) \Psi(x) \Big|_{x=0} = 0. \tag{2.15}$$

Therefore the topological properties of the lattice model – the invariant and the edge states – are encoded in the low-energy model.

An alternative approach to study the topological difference between both insulating phases is to consider a domain-wall made separating the two insulating phases. The “heterostructure” is simulated by

$$H = v_F\sigma_y p_x + m(x)\sigma_x, \tag{2.16}$$

where $p_x = -i\partial_x$ is the momentum operator and $m(x)$ describes the variable mass changing from $m(x < 0) < 0$ to $m(x > 0) > 0$. This problem was first studied by Jackiw and Rebbi [12], and leads to the solitonic solution

$$\Psi_{zero} \propto e^{-\int_{x_0}^{x} dx' m(x')/v_F} \begin{pmatrix} 1 \\ 0 \end{pmatrix} \quad (x_0 \text{ arb.}) \tag{2.17}$$

with energy $E_{zero} = 0$, and thus describing the normalizable zero-mode living at the domain wall. The existence of this state is independent of the detailed form of $m(x)$ (see Fig. 2.5). The number of the edge states M in this domain wall description can also be related to the difference in the topological invariants of the left and the right side:

$$M = |W(x \to +\infty) - W(x \to -\infty)| \tag{2.18}$$

although the definition for each W (Eq. 2.12) of the effective Hamiltonian (Eq. 2.16) does

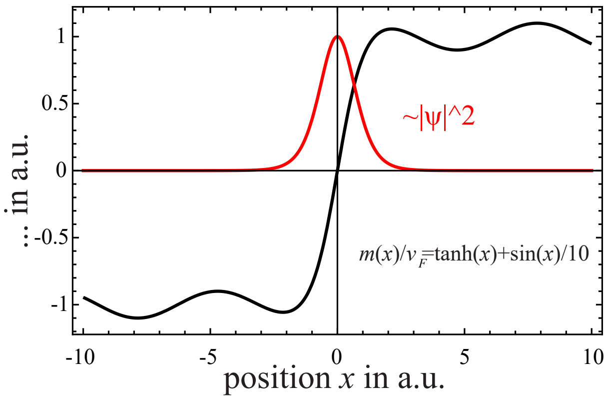

Figure 2.5: One example of a mass profile for the domain wall (black) and its localized zero mode (red) are plotted in arbitrary units.

not give integer values but only half-integers. This is a feature of the effective theory, and will be explained in the next chapter. In any case, the SSH model can be seen as the simplest lattice model combining both aspects of topological states of matter: the topological invariant and the edge states.

2.2 Quantum Hall effect and Landau levels

In 1980, Van Klitzing and coworkers measured the Hall conductivity of a two-dimensional electron gas (2DEG) realized in a silicon metal-oxide-semiconductor field-effect transistor [13]. By applying a magnetic field perpendicular to the electron gas the measurements show a precise quantization of the Hall conductivity along with a vanishing longitudinal conductivity. This *(integer) quantum Hall effect* (QHE) became the starting point for a new research area after it was realized that it has a topological origin [14, 15].
Let us start with the effective Hamiltonian of an electron coupled to a time-independent magnetic field $\mathbf{B}$ which can be written as

$$\mathcal{H} = \frac{1}{2m}(\hat{\mathbf{p}} - e\mathbf{A})^2 \text{ with } \nabla \times \mathbf{A} = \mathbf{B}, \tag{2.19}$$

the momentum operator $\hat{\mathbf{p}}$, the gauge field $\mathbf{A}$ minimally coupled to the electronic system and the coupling constant $e < 0$ describing the electronic charge. Fixing the magnetic field direction to be $\mathbf{B} = B_z\mathbf{e}_z$ reduces the problem to a harmonic oscillator. It is helpful to use two types of orthogonal annihilation and creation operators [16] with the commutator relations $[\hat{a}, \hat{a}^\dagger] = [\hat{b}, \hat{b}^\dagger] = 1$ defined by

$$\hat{a} = \frac{1}{\sqrt{2m\hbar\omega_c}}(\hat{p}_x - eA_x - i(\hat{p}_y - eA_y)),\ \hat{b} = i\hat{a}^\dagger + \sqrt{\frac{m\omega_c}{2\hbar}}(x + iy), \tag{2.20}$$

and their hermitian-conjugated partners to map the system *independent* of the gauge in the form of a harmonic oscillator $\mathcal{H}_{HO}$ with the cyclotron frequency $\omega_c = |e|B_z/m$

$$\mathcal{H}_{HO} = \hbar\omega_c(\hat{a}^\dagger\hat{a} + 1/2) \tag{2.21}$$

and a residual part in direction of the magnetic field: $H_{free} = (\hat{p}_z - eA_z)^2/(2m)$. The last term commutes with the Hamiltonian Eq. (2.21) and describes simply a free motion in the z direction, because A_z has to be a pure gradient $\partial_z\xi$ of a scalar function. This part describes the subband structure of the 2DEG and can be simply removed from the Hamiltonian using the *quantum well approximation*: $\langle\hat{p}_z - eA_z\rangle = 0$ and $\langle(\hat{p}_z - eA_z)^2\rangle > 0$. H_{free} contributes then with an irrelevant energy offset.

The energy levels of the harmonic oscillator part $\mathcal{H}_{HO}$ are generally referred to as *Landau levels* (LLs). Interestingly, the Hamiltonian describing the LLs comes from a two-dimensional problem, but we ended up with a simple form of a one-dimensional Hamiltonian. This shows that the LLs described by $\hat{a}$ must be infinitely degenerate. The boson $\hat{b}$ distinguishes the degenerate states in the same LL. Finally one can say that the eigenproblem of $\mathcal{H}_{HO}$ is solved by

$$\mathcal{H}_{HO}\,|k,p\rangle = \hbar\omega_c\left(k + \frac{1}{2}\right)|k,p\rangle\,,\ \hat{b}^\dagger\hat{b}\,|k,p\rangle = p\,|k,p\rangle \text{ and } k,p \in \mathbb{N}. \tag{2.22}$$

Using the vacuum condition $\hat{a}\,|0,p\rangle = 0$, we can get the representation of the lowest LL by

$$\langle\mathbf{r}|0,p\rangle \propto \left(\frac{x - iy}{\sqrt{2}l}\right)^p e^{-(x^2+y^2)/(4l^2)} \text{ for } \mathbf{A} = \frac{B_z}{2}(x\,\mathbf{e}_y - y\,\mathbf{e}_x) \tag{2.23}$$

which is characterized by the length $l^2 = \hbar/(|e|B_z)$. The boson $\hat{b}$ can be seen in this representation as an angular momentum so that the solutions are orbital-like. The other missing eigenstates can be generated by applying n-times the bosonic creation operator $\hat{a}^\dagger$ on the degenerate ground state. With this, the problem is solved for the bulk. The next thing is to ask what happens if we add an edge to the system. We want to consider the full problem in the half space $x > 0$.

For simplicity, we choose now a particular gauge known as the *Landau gauge* where $\mathbf{A} =$

$B_z x\, \mathbf{e}_y$ so that the Hamiltonian can be written as

$$\mathcal{H}_{HO} = \frac{1}{2m}(\hat{p}_x^2 + \hat{p}_y^2 - 2eB_z x\hat{p}_y + (eB_z)^2x^2). \tag{2.24}$$

Note that after introducing the edge we have still translational invariance parallel to the edge, that is $[\mathcal{H}_{HO}, \hat{p}_y] = 0$. We may write all eigenfunctions of $\mathcal{H}_{HO}$ as eigenfunctions of $\hat{p}_y$, namely

$$\Psi \propto Y(y)X(x), \text{ where } Y(y) = e^{ik_y y}. \tag{2.25}$$

After this substitution we find that $X(x)$ satisfies the equation

$$\left[\frac{1}{2m}p_x^2 + \frac{1}{2}m\omega_c^2(x - x_0(k_y))^2\right] X(x) = EX(x) \tag{2.26}$$

with $x_0(k_y) = \hbar k_y/(eB_z)$. This equation is exactly the form of a harmonic oscillator shifted by x_0. Following the calculation of Ref. [17], the last equation can be now compared with the *Weber equation*

$$\frac{d^2X(z)}{dz^2} + (\mu + \frac{1}{2} - \frac{1}{4}(z - z_0)^2)X(z) = 0, \tag{2.27}$$

where $z = (2m\omega_c/\hbar)x$ and $\mu = E/(\hbar\omega_c) - 1/2$. The generic solution for this differential equation is the *Weber function*

$$\begin{aligned} D_\mu(z) =& 2^{\mu/2} e^{-(z-z_0)^2/4} \left(\frac{\sqrt{\pi}}{\Gamma(\frac{1}{2} - \frac{\mu}{2})} F(-\frac{\mu}{2}, \frac{1}{2}, \frac{1}{2}(z - z_0)^2) - \right. \\ & \left. \frac{\sqrt{2\pi}(z - z_0)}{\Gamma(-\frac{\mu}{2})} F(\frac{1}{2} - \frac{1}{2}\mu, \frac{3}{2}, \frac{1}{2}(z - z_0)^2) \right), \end{aligned} \tag{2.28}$$

where $F(a, b, z)$ is the *confluent hypergeometric function* [18]

$$F(a, b, z) = \sum_{k=0}^{\infty} \frac{(a)_k}{(b)_k} \frac{z^k}{k!} \text{ with } (a)_k = a(a + 1) + ...(a + k - 1) \tag{2.29}$$

and $\Gamma(z)$ is the *gamma function*

$$\Gamma(z) = \int_0^\infty t^{z-1} e^{-t} dt. \tag{2.30}$$

In order to have a wavefunction which is quadratically integrable, μ has to be positive (≥ 0) and integer. This leads to the well-known *Hermite polynomials* for $x \in (-\infty, +\infty)$.

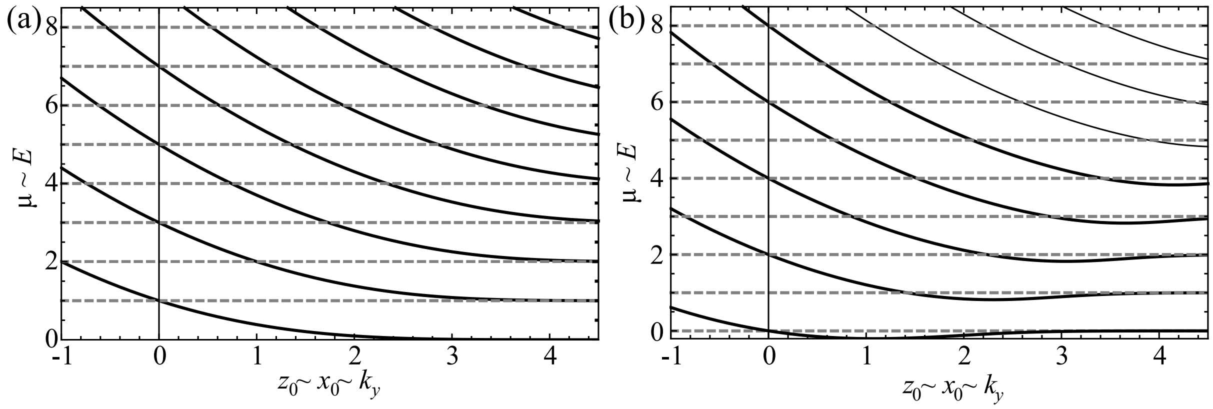

Figure 2.6: The graphical solution $\mu(z_0)$ of the transcendent equation is plotted in (a) showing the bending of the LLs. The panel (b) shows the same for NBC. The dashed lines are the LLs without edge and the solid lines are the results for $x > 0$.

However, we want to study the problem on the half space $x \in [0, +\infty)$ where the wave function should fulfill the fixed boundary condition (FBC) $X(x = 0) = 0$, equivalent to the quantization condition $D_\mu(0) = 0$, or natural boundary condition (NBC) $X'(x = 0) = 0$, equivalent to $D'_\mu(0) = 0$. Each equation is a *secular equation* and can be used to calculate the energy spectrum $\mu(z_0)$. It is interesting to consider two important limits of these spectra. The first one is $z_0 \to \infty$ where the boundary is far away from the minimum of the harmonic oscillator. The spectrum is then equivalent to the spectrum of the problem over the full space. We have $\mu \in \{0, 1, 2, 3, ...\}$. In the limit $z_0 = 0$ we have instead the *half-side* harmonic oscillator where only odd (FBC) or even (NBC) functions are allowed. This restricts the integer quantum numbers to be odd and even as well. The graphical solutions of the transcendent equation are plotted in Fig. 2.6.

These results are consistent with the qualitative discussion of Ref. [19]. Near the edge – where $z_0 \approx 0$ – the LLs bend upwards. The half-plane system acquires the properties of a one-dimensional metal. In contrast to the full-plane treatment, where we find a huge degeneracy at the energies $\mu = 1, 2, 3....$, the degeneracies are lifted. Nevertheless the density of states has still its maximum at the LL energies. We have to remark that in the momentum k_y we find a huge chiral imbalance. One finds the bending only for $k_y < 0$, but for $k_y \to \infty$ the extended LLs are flat. Considering the half-space $x < 0$ instead the roles are interchanged. If we introduce two edges to simulate a two-dimensional channel it is clear that we get bending of the states not only close to $z_0 \approx 0$, but also at $z_0 \approx L$ where L is the channel width.

This has a consequence if we switch our consideration to the real many-particle problem. Let us fill up this system with non-interacting, spinless fermions until the Fermi level E_F

lies in the “bulk" gap between the n-th and $(n+1)$-th LL. Nevertheless, for the finite size system, the spectrum close to the edges is bending upward such that the system is no longer insulating. At the left and the right edges each of the n LLs crosses E_F forming a *mobility edge*. The transport is dominated by the metallic edge while the bulk is insulating. The left edge state has negative k_y while the right edge state has positive k_y showing that the edge states are chiral. The presence of this mobiltity edge is the basis of the QHE and follows from the topologically non-trivial properties which will be discussed now.

2.3 Laughlin's Gedankenexperiment

In order to explain the quantization of the Hall conductivity, Laughlin considered a Gedankenexperiment [20] as shown in Fig. 2.7. The electron gas is confined in an annulus, known as *Corbino disk*. The x-y coordinates are chosen in this way: the x axis is in the radial direction of the Corbino disk and its coordinate runs from $0 < x \leq L_x$ while the y axis is in the tangential direction and L_y-periodic. The wavefunctions have to fulfill: $\Psi(x, y+L_y) = \Psi(x, y)$. The periodic boundary conditions (PBC) along y necessitate that the quantum number k_y assumes the discrete values $k_y \rightarrow k_n = 2\pi n/L_y$ where n is integer. We add now an additional magnetic flux Φ in the center of the Corbino disk $(x = 0)$. This flux penetrates in the hole of the disk, but not in the annulus. The vector potential $\mathbf{A}$ then is changed by

$$\mathbf{A} \rightarrow \mathbf{A} + \frac{\Phi}{L_y}\mathbf{e}_y, \tag{2.31}$$

which is equivalent to a change in the Hamiltonian Eq. 2.19

$$p_y \rightarrow p_y + \frac{2\pi\hbar}{L_y}\frac{\Phi}{\Phi_0}, \tag{2.32}$$

where Φ_0 is the flux quantum. In the LLs this insertion shifts the guiding center x_0. The wavefunction along k_y can be therefore simply written as

$$Y_\Phi(y) = e^{i2\pi\Phi/\Phi_0\, y/L_y} Y(y). \tag{2.33}$$

Interestingly the phase difference between the two gauges Y and Y_Φ is not single valued. Due to the PBC the phase difference has to fulfill

$$\Phi = n\Phi_0, \text{ where } \Phi_0 = \frac{2\pi\hbar}{e} \text{ and } n \in \mathbb{Z}. \tag{2.34}$$

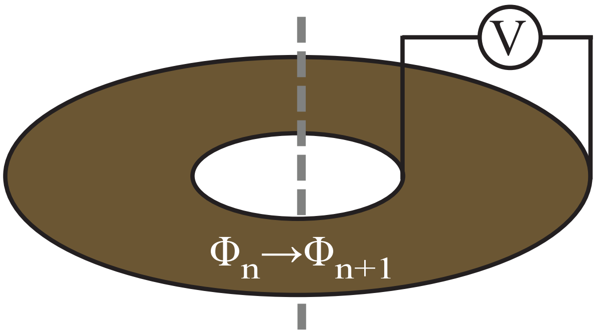

Figure 2.7: The Corbino disk represents the geometric specification to measure the QHE. The voltmeter is connected to the edges. The hole is assumed to be infinitesimally small where we add one quantum to the magnetic flux to induce a radial current in the disk.

The flux must be quantized to ensure gauge equivalence. All other values of Φ do not respect periodicity in the y-direction. By going adiabatically from Φ to $\Phi + \Phi_0$ we map the system on its own, but changing its energy due to the shift of x_0. A Φ_0 insertion is related to a process $|n, k_y\rangle \rightarrow |n, k_y - 2\pi/L_y\rangle$, which creates a charge imbalance between the inner and the outer boundary of the disk in one LL – a hole on one side and an electron on the other. If n bulk bands are filled then there are n edge electrons involved.

The total energetic difference ΔE given by this imbalance is then neV where the voltage V describes the electrostatic potential generated by moving one electron from the outer to the inner edge. One can write the current-voltage relation as

$$I = \frac{dE}{d\Phi} \rightarrow \frac{\Delta E}{\Phi_0} = \frac{neV}{h/e} = \sigma_H V \text{ with } \sigma_H = n\frac{e^2}{h}. \tag{2.35}$$

Every bulk LL gives a contribution of e^2/h to the *Hall conductivity* σ_H. This is a quite general result and independent on the boundaries, impurities or temperature up to some extent [20]. An alternative approach for calculating the Hall conductance using the Kubo formula on LLs leads to the same result and is given in Ref. [21]. As we will show, the number n in the Hall conductivity is a topological invariant and corresponds to the number of (topologically protected) edge states.

2.4 Quantum Hall effect on the lattice

The topological nature of the QHE becomes manifest also in a TB model where the effect of a magnetic field is incorporated. The simplest example is the *Hofstadter problem* [22], named after Douglas Richard Hofstadter who studied spinless electrons in a constant magnetic field on a square lattice. The corresponding TB Hamiltonian can be written as

$$\mathcal{H} = -t \sum_{<i,j>} \hat{c}_j^\dagger \hat{c}_i e^{i\theta_{ij}} + h.c., \tag{2.36}$$

where $\hat{c}_i$ is the fermion annihilation operator at site i of the two-dimensional square lattice, and t is the nearest-neighbor hopping amplitude. The phase factors $\theta_{ij} = -\theta_{ji}$ can be identified with the phase picked up by the electrons going from lattice site i to j

$$\theta_{ij} = \frac{2\pi}{\Phi_0} \int_i^j \mathbf{A} \cdot d\mathbf{l}. \tag{2.37}$$

By hopping around one *plaquette* the net flux is given by

$$\frac{2\pi}{\Phi_0} B_z \mathcal{F}_{plaq} \equiv 2\pi\alpha, \tag{2.38}$$

where B_z is the magnetic field strength, $\mathcal{F}_{plaq}$ is the area of the plaquette, Φ_0 the magnetic flux quantum, and α a dimensionless parameter.
At this point we are allowed by the gauge degree of freedom to freely distribute the net flux over the plaquette. Using the *Landau gauge* for each plaquette [23], we can rewrite the lattice Hamiltonian in the form

$$H = -t \sum_{m,n} (\hat{c}_{m+1,n}^\dagger \hat{c}_{m,n}^\dagger + e^{i2\pi\alpha m} \hat{c}_{m,n+1}^\dagger \hat{c}_{m,n}) + h.c., \tag{2.39}$$

where $\{m, n\}$ are the lattice coordinates in the $\{x, y\}$ directions.
For an infinitely large system the Fourier transform of the fermion operators is given by an integral over the first BZ as

$$\hat{c}_{m,n} = \int_0^{2\pi} dk_x \int_0^{2\pi} dk_y e^{imk_x + ink_y} \hat{c}_{\mathbf{k}}, \tag{2.40}$$

and therefore the Hamiltonian is

$$\mathcal{H} = \int_0^{2\pi} dk_x \int_0^{2\pi} dk_y H(\mathbf{k}) \tag{2.41}$$

with

$$H = -t \cos k_x \hat{c}_{\mathbf{k}}^\dagger \hat{c}_{\mathbf{k}} - te^{-ik_y} \hat{c}_{k_x+2\pi\alpha,k_y}^\dagger \hat{c}_{\mathbf{k}} - te^{+ik_y} \hat{c}_{k_x-2\pi\alpha,k_y}^\dagger \hat{c}_{\mathbf{k}}, \tag{2.42}$$

where we set the lattice constant $a = 1$.
To proceed further, it is helpful to represent α by a quotient of p and q being coprimes. This excludes irrational flux penetrating the unit cell but simplifies the upcoming considerations. For such parameters α the spectrum splits into q subbands. We define $\hat{c}_j(\tilde{k}_x, k_y) = \hat{c}(k_x = \tilde{k}_x + 2\pi\alpha j, k_y)$ where $(\tilde{k}_x, k_y)$ is the momentum of the magnetic Brillouin zone $[-\pi/q, \pi/q) \times [-\pi, \pi)$, and $j = 1...q$. This leads to the transformed Hamiltonian

$$\mathcal{H} = \int_{MBZ} d\tilde{k}_x dk_y \sum_{j=1}^{q} H_j(\tilde{k}_x, k_y) \tag{2.43}$$

with $H_j(\tilde{k}_x, k_y) := H(\tilde{k}_x + 2\pi\alpha j, k_y)$. The H_j can be written as

$$H_j = -\, 2t\cos(\tilde{k}_x + 2\pi\alpha j)\hat{c}_j^\dagger \hat{c}_j - te^{-ik_y}\hat{c}_{j+1}^\dagger \hat{c}_j - te^{+ik_y}\hat{c}_{j-1}^\dagger \hat{c}_j. \tag{2.44}$$

Since the Hamiltonian does not couple different momentum states, we can study a particular block of the Hamiltonian with fixed momentum quantum numbers. The eigenvalue equation of the operator

$$\sum_{j=1}^{q} H_j(\tilde{k}_x, k_y) \equiv H_{Harper}(\tilde{k}_x, k_y) \tag{2.45}$$

is the root of the so-called *Harper's equation* (or *Almost Mathieu equation*). Considering the Schrödinger problem of the Hamiltonian H_{Harper} in the q-dimensional complex vector space $\mathbb{C}^q$ with the representation $\{u_0, ...u_{q-1}\}$ leads to

$$-e^{-ik_y}u_{j-1} - 2\cos(\tilde{k}_x + 2\pi\alpha j)u_j - e^{+ik_y}u_{j+1} = \frac{E}{t}u_j, \tag{2.46}$$

where $u_0 = u_q$ and $u_1 = u_{q+1}$.
The energy spectrum of this secular equation leads to the well-known *Hofstadter butterfly* shown in Fig. 2.8. It is a *fractal* structure showing *self-similarity*. Small fragments in the structure contain copies of the entire structure.
Although the spectrum has only very little similarity to the LLs its electromagnetic behavior is nearly equal. Thouless et al. [14] showed that each band $1 < j < q$ carries an integer Hall conductance for the same topological reason of the LLs. In the next section, we will introduce the corresponding topological TKNN invariant.

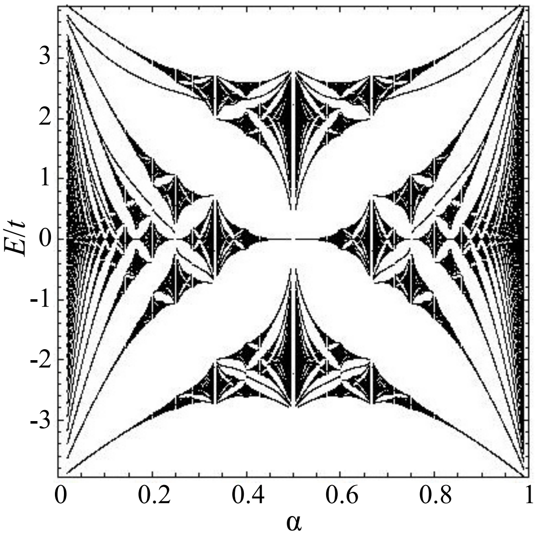

Figure 2.8: The *Hofstadter butterfly* represents the spectrum $E(\alpha)$ projected out for all $(\tilde{k}_x, k_y)$. The discretization is given by $\alpha = p/100$. The white regions describe the gaps and black the bulk.

2.5 TKNN invariant and the Chern response

We here introduce the topological invariant predicting the quantized Hall conductivity: the Chern number. We start with the generic *Green function* for fermions $G^{-1}(\omega, \mathbf{k}) = i\omega\mathbb{1} - \mathcal{H}(\mathbf{k})$ and a lattice Hamiltonian $\mathcal{H}(\mathbf{k})$ where ω is the frequency associated to imaginary time it. The quantum field theoretical problem is represented by the action

$$S = \int d^2k d\omega\, \mathcal{L},\, \mathcal{L} = \Psi^\dagger(G^{-1} + j_\alpha A^\alpha)\Psi \text{ and } j_\alpha = -q\frac{\partial G^{-1}}{\partial k^\alpha},\; (k_\alpha) = \{\omega, k_x, k_y\}, \tag{2.47}$$

where we minimally coupled an external electromagnetic field to the wave function Ψ via the charge q ($-e$ for electrons). The operator j_α is the related current operator. Assuming an electromagnetic response due some external field A_μ one can expand

$$\begin{aligned} S_{eff} &= -\log\det(G^{-1} + j_\alpha A^\alpha) \\ &= -\operatorname{tr}\log(G^{-1}) - \operatorname{tr}(G j_\alpha A^\alpha) - \frac{1}{2}\operatorname{tr}(G j_\alpha A^\alpha G j_\beta A^\beta) + ... \end{aligned} \tag{2.48}$$

after integrating out the electronic part. The zeroth order term in the expansion is an irrelevant offset, the first order one a *tadpole* which is a one-loop Feynman diagram with one external leg. This can give a contribution to a one-point correlation function, but for e.g. a Dirac fermion, this contribution vanishes due to the trace over Dirac matrices [24]. The next one is the second order term, which describes a fermion loop (illustrated in

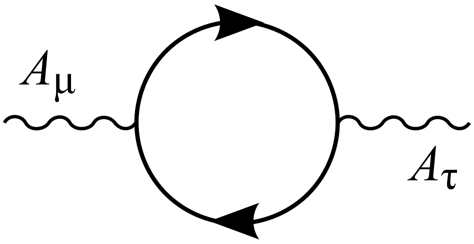

Figure 2.9: The one-loop *Feynman* diagram induces the *Chern-Simons* term in its long-wavelength limit.

Fig. 2.9) and contains the interesting long-wavelength limit.
One can write the physical relevant – topological – part as [25, 24]

$$S_{top} = \frac{\nu}{4\pi} \int d^2x \int dt \; A_\mu \varepsilon^{\mu\nu\tau} \partial_\nu A_\tau \tag{2.49}$$

with a constant ν and the units $e = \hbar = 1$. This form is equivalent to the electromagnetic response considered in the Laughlin argument, but now we have an invariant which is determined by the Green function of the electrons. The so-called *TKNN invariant* [14] named after Thouless, Kohmoto, Nightingale and den Nijs who gave the first closed expression of ν is defined in this formalism by [26, 27]

$$\nu = \frac{\varepsilon_{\alpha\beta\gamma}}{6} \int_{occ.} d\omega \int_{\mathcal{M}} \frac{d^2k}{(2\pi)^2} \mathrm{tr}(G^{-1}\partial_\alpha G G^{-1}\partial_\beta G G^{-1}\partial_\gamma G), \tag{2.50}$$

where the contour of ω is the line integral $(-\infty, +\infty)$ in the gap between occupied and non-occupied states, and $\mathcal{M}$ is the momentum manifold. This number can be deduced from the underlying fermionic theory directly which allows us to study now arbitrary systems. To restore the electromagnetic response of Eq. (2.35) we can use the variational approach on the action $\delta S_{top}/\delta A_\mu = j^\mu$. This leads to

$$j^\mu = \sigma_H \varepsilon^{\mu\nu\tau} \partial_\nu A_\tau \tag{2.51}$$

and the quantized Hall conductivity $\sigma_H = \nu/(2\pi)$. In the original TKNN paper the authors actually used the *Kubo formula* to compute the Hall conductance leading to the same result. However, the topological invariant can be also written in the more practical form

$$\nu = \sum_{m \in occ.} \sum_{n \in unocc.} \int_{\mathcal{M}} \frac{d^2k}{2\pi i} (\langle m|\nabla n\rangle \times \langle n|\nabla m\rangle)_z \tag{2.52}$$

by using the eigenstates of the Hamiltonian $\{|n\rangle\}$. The eigenstates are divided in states which are occupied and the one which are not occupied in the sense of the discussed *warping gap* condition.

If one has (n) bands and $(n-1)$ gaps then one can introduce new invariants describing the difference of the TKNN invariant between two neighboring gaps. The corresponding invariant is called *Chern number* of the band l and is defined via

$$\nu_l = \nu(\text{gap over band } l) - \nu(\text{gap below band } l) = \sum_{n \neq l} \int_{\mathcal{M}} \frac{d^2k}{2\pi i} (\langle l|\nabla n\rangle \times \langle n|\nabla l\rangle)_z. \quad (2.53)$$

Furthermore, this allows us to write the TKNN invariant as a sum over all Chern numbers corresponding to the occupied states. To simplify this more we use projectors $P_l = |l\rangle \langle l|$ to represent the eigenstates in the expression above. This allows us to write

$$\nu_l = \frac{1}{2\pi} \int_{\mathcal{M}} \hat{\Omega}_l, \text{ where } \hat{\Omega}_l = i\,\mathrm{tr}(P_l dP_l \wedge dP_l) \quad (2.54)$$

using *differential forms*. The form $\hat{\Omega}_l$ is here $\Omega_l \, dk_x \wedge dk_y$ where Ω_l is a scalar form of the well-known *Berry curvature* defined by the z-component of $\nabla_{\mathbf{k}} \times \mathbf{A}_l$ with $\mathbf{A}_l = i \langle l|\nabla_{\mathbf{k}}|l\rangle$. The Chern number is a gauge invariant quantity like the Berry curvature, but the Berry curvature can change if one adds a phase to every basis atom in the crystal. This allows us to use other definitions of the Berry curvature to describe the same phase in crystals. They are discussed in Ref. [28]. By making a general unitary transformation $U(k_x, k_y)$ we change the differential form of the Berry curvature to

$$-i\hat{\Omega}' = -i\hat{\Omega} + \mathrm{tr}((dP - PUdU^\dagger) \wedge UdU^\dagger) \quad (2.55)$$

using $dU^\dagger U = -U^\dagger dU$, $PdPP = 0$ and $\mathrm{tr}(A \wedge B) = -\mathrm{tr}(B \wedge A)$.

If we now consider the difference of the two integrals over Ω' and Ω we can find a non-zero contribution in general to ensure gauge invariance. To show an example that the definition of the Chern number depends on the basis choice we can take the unitary transformation diagonalizing the Hamiltonian. This is a transformation making all bands trivial which means that the projectors in the transformed picture show no $\mathbf{k}$-dependence and therefore $\nu_l' = 0$.

However one is more interested in the opposite case. The question should be which unitary transformation leaves the definition written in Eq. (2.54) invariant. For our purposes we want to show that a unitary transformation, chosen such that every basis vector of the Hamiltonian only gets a phase, fulfills this. The matrix U has then only diagonal elements of the form $U_{ii} = \exp(i\phi_i(k_x, k_y))$ so that we can find

$$\Omega' - \Omega = \sum_i d(P_{ii} \wedge d\phi_i) \tag{2.56}$$

after some elementary transformations where P_{ii} is the (i,i)-th component in the matrix of P. If we now integrate we get

$$\int_{\mathcal{M}} (\Omega' - \Omega) = \sum_i \oint_{\partial\mathcal{M}} P_{ii} d\phi_i = 0. \tag{2.57}$$

The integral vanishes because its integrand is analytical. This degree of freedom to choose our U ensuring the right Chern number is useful in many examples.

2.6 $\mathbb{Z}_2$ topological insulators

The previous two-dimensional fermionic systems have a *broken* time-reversal (TR) symmetry. If we preserve TR symmetry in a fermionic model, the topological invariant cannot be any longer the Chern number simply because it is always zero. Nevertheless, TI states of matter can also arise in TR invariant systems.

In a two-dimensional TR invariant system this can be simply achieved by a *doubling* of the Hilbert space. This is a technique to embed two TR broken Hamiltonians into a single TR invariant model, and it is the basis underlying the discovery of the *Quantum Spin Hall* (QSH) phase [29, 30]. In these systems one component of the spin operator (let us say S_z) commutes with the Hamiltonian, and thus each spin channel $S_z |\pm\rangle = \pm 1/2 |\pm\rangle$ can be treated independently. A generic TR Hamiltonian can be built from two Chern insulators through

$$\mathcal{H}_{TR} = \begin{pmatrix} \mathcal{H}(k_x, k_y) & 0 \\ 0 & \mathcal{H}^*(-k_x, -k_y) \end{pmatrix} \tag{2.58}$$

with the fermionic TR operator $\mathcal{T} = i\sigma_2 \otimes \mathbb{1}^{\mathcal{H}} \mathcal{K}$ where $\mathcal{K}$ is complex conjugation and $\mathbb{1}^{\mathcal{H}}$ is the identity operator in the Hilbert space of operator $\mathcal{H}$. Due to the $U(1) \times U(1)$ symmetry we can simply use the Chern number of one spin channel ν_+ to topologically characterize the full system. This invariant is called the *Spin Chern number*. The opposite spin channel has opposite spin Chern number $\nu_- = -\nu_+$. By lifting this $U(1)$ symmetry, one can show that the numbers (ν_+, ν_-) are no longer preserved. The invariant of such a system is therefore no longer an integer $\mathbb{Z} = \{0, \pm 1, \pm 2, ...\}$, but a $\mathbb{Z}_2 = \{0, 1\}$ number. This new invariant was found using the relation between the Chern number and the charge

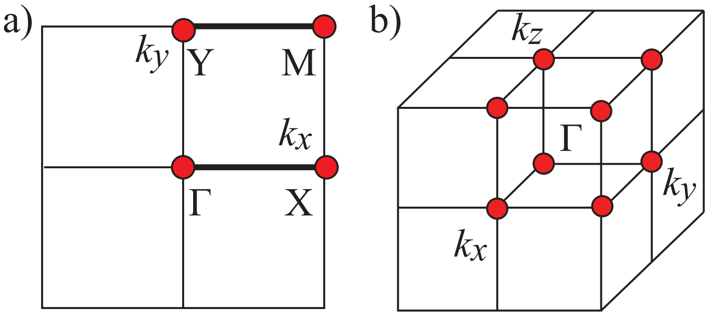

Figure 2.10: The TRIM points for a generic BZ $[-\pi,\pi) \times [-\pi,\pi)$ (a) and $[-\pi,\pi) \times [-\pi,\pi) \times [-\pi,\pi)$ (b) by setting the lattice spacing $a = 1$. The thick lines represent two TR invariant paths used in Eq. (2.74).

transferred in a one-dimensional topological pump, and was discovered by Fu and Kane [31] introducing the new concept of *TR polarizations.*

We start by recalling that at the so called *TR invariant momenta* (TRIM) Λ_i

$$\Lambda_i = \frac{1}{2}\sum_{j=1}^{d} c_i^{(j)} \mathbf{b}_j \text{ (where all } c_i^{(j)} \in \mathbb{Z}) \tag{2.59}$$

defined modulo a reciprocal lattice vector with the primitive vectors $\mathbf{b}_j$ in d dimensions, each fermionic band is doubly degenerate due the *Kramers theorem* [32]. For the Bloch wave functions

$$|\Psi_n(\mathbf{k})\rangle \propto e^{i\mathbf{k}\cdot\mathbf{r}} |u_n(\mathbf{k})\rangle \,, \tag{2.60}$$

with the envelope functions $|u_n(\mathbf{k})\rangle$ having the same periodicity as the crystal, Kramers theorem implies that $|u_n(\Lambda_i)\rangle$ and $\mathcal{T}\,|u_n(\Lambda_i)\rangle$ have the same energy and are orthogonal to each other at the TRIM. The TRIM are shown for $d = 2$ and $d = 3$ in Fig. 2.10.

Let us now consider envelope functions close to the TRIM Γ along k_x. Following Ref. [31] we can relabel the bands $m \cong (n, I/II)$ by the number n counting the Kramer pairs at the Γ point and a number I/II describing the two-dimensional subspace of the two TR partners. The identification is given by

$$|u_{(n,I)}(k_x)\rangle \text{ and } |u_{(n,II)}(-k_x)\rangle = e^{-i\chi(n,-k_x)}\mathcal{T}\,|u_{(n,I)}(k_x)\rangle \tag{2.61}$$

up to a phase factor $\chi(n, k_x)$. These important phases are also encoded in the *sewing* *matrix*

$$(B_{nl})_{\alpha\beta} = \langle u_{(n,\alpha)}(-k_x)|\mathcal{T}|u_{(l,\beta)}(k_x)\rangle = \delta_{nl} \begin{pmatrix} 0 & -e^{i\chi(n,k_x)} \\ e^{i\chi(n,-k_x)} & 0 \end{pmatrix}_{\alpha\beta} , \tag{2.62}$$

where $\alpha, \beta \in \{I, II\}$. This separation of bulk states allows to track the charge polarization of each individual band as explained below.

From the Bloch wave functions we construct another complete set of orthogonal functions. This new set was introduced by G. H. Wannier [33] and are called *Wannier functions*. They are lattice-periodic generalizations of the non-orthogonal atomic/molecular orbitals in a crystal defined by

$$|\mathbf{\Psi}_n(\mathbf{R})\rangle = \frac{\sqrt{N}}{V_d} \int_{BZ} d^d\mathbf{k}\, e^{-i\mathbf{k}\cdot\mathbf{R}}\, |\Psi_n(\mathbf{k})\rangle \,, \tag{2.63}$$

where V_d is the BZ volume in d dimensions, $\mathbf{R}$ is the lattice vector corresponding to each primitive cell and N is the number of unit cells. Let us define a hybrid wavefunction $|\mathbf{\Psi}_n(R_i; k_y, k_z, ..., k_d)\rangle$, where only the k_x component is Fourier-transformed, and a position operator

$$\hat{x} = \sum_{i=-\infty}^{\infty} \sum_n R_i \,|\mathbf{\Psi}_n(R_i; k_y, k_z)\rangle \,\langle \mathbf{\Psi}_n(R_i; k_y, k_z)| \,, \tag{2.64}$$

which acts like a *canonical* position operator. For a general system King-Smith and Vanderbilt [34] have shown that the total charge polarization in x-direction is the sum of the centers of charge of all occupied (hybrid) Wannier states at $R_i = 0$. This can be written as

$$P_C(k_y) = \sum_{n \text{ occ.}} \langle \mathbf{\Psi}_n(0; k_y)|\hat{x}|\mathbf{\Psi}_n(0; k_y)\rangle = \sum_{n \text{ occ.}} \frac{1}{2\pi} \int_{-\pi}^{\pi} dk_x (\mathbf{A}_n)_x(\mathbf{k}) \tag{2.65}$$

with the x-component of the *vector potential* $\mathbf{A}_n(\mathbf{k}) = \langle u_n(\mathbf{k})|i\nabla_{\mathbf{k}}|u_n(\mathbf{k})\rangle$. This quantity is not yet gauge invariant. A gauge-invariant quantity can be defined by:

$$\Delta P_C = P_C(k_y^1) - P_C(k_y^2) = \sum_{n \text{ occ.}} \int_{k_y^2}^{k_y^1} dk_y \int_{-\pi}^{\pi} dk_x\, \Omega_n(\mathbf{k}), \tag{2.66}$$

where one assumes that $|u_n(\mathbf{k})\rangle$ is defined continuously between k_y^1 and k_y^2 so that we can use *Stokes theorem* to rewrite ΔP_C with the Berry curvature Ω_n (see Eq. (2.54)). This quantity describes the pumped charge if one tunes k_y from k_y^1 to k_y^2. This is equivalent to the pumping process for the LLs. In the case $k_y^1 - k_y^2 = 2\pi$ we complete a full charge pumping cycle and the right side of (2.66) turns into the definition of the Chern number. Coming back to the TR invariant system, we know that P_C has now two contributions: P_C^I and P_C^{II}. Both contributions cancel each other in a pumping process ($\Delta P_C = P_C^I + P_C^{II} = 0$). That is why we are not interested in the sum of both contributions but in the difference

$$P_T \equiv P_C^I - P_C^{II} = 2\Delta P_C^I. \tag{2.67}$$

This is exactly what we want for the definition of the TR polarization. To calculate P_T along one TR path in k_x-direction (thick lines in Fig. 2.10) we use the relation

$$A_x((n, II), k_x) = A_x((n, I), -k_x) - \partial_{k_x}\chi(n, k_x) \tag{2.68}$$

such that the TR polarization for the band n can be written as

$$P_T(n) = \frac{1}{2\pi}\int_0^\pi dk_x \left[\partial_{k_x}\chi(n, k_x) - \partial_{k_x}\chi(n, -k_x)\right] \tag{2.69}$$

or equivalently with the sewing matrix formalism [31]

$$\begin{aligned} P_T(n) =& \frac{i}{\pi}\left[\frac{1}{2}\int_0^\pi dk_x\partial_{k_x}\log\det(B_{nn}(k_x)) - \log\frac{\mathrm{Pf}(B_{nn}(\pi))}{\mathrm{Pf}(B_{nn}(0))} + 2\pi i l\right] \\ =& \frac{i}{\pi}\log\frac{\sqrt{\det B_{nn}(\pi)}\mathrm{Pf}(B_{nn}(0))}{\mathrm{Pf}(B_{nn}(\pi))\sqrt{\det B_{nn}(0)}} + 2l, \end{aligned} \tag{2.70}$$

where l is an integer defining the *branch* of the log function. By using $\det B_{nn} = (\mathrm{Pf}(B_{nn}))^2$ we see that the function is of the form $z/\sqrt{z^2}$, and can therefore, only assume values ± 1 (for $z \neq 0$). With that, one can rewrite the formula above as

$$\frac{\sqrt{\det B_{nn}(\pi)}\mathrm{Pf}(B_{nn}(0))}{\mathrm{Pf}(B_{nn}(\pi))\sqrt{\det B_{nn}(0)}} = (-1)^{P_T \bmod 2}. \tag{2.71}$$

The sign determines whether the $\mathrm{Pf}(B_{nn})$ for the two TRIM points are on the same or opposite branch of $\sqrt{\det B_{nn}}$. At this point we note that P_T mod 2 is not yet the desired $\mathbb{Z}_2$ invariant. It is not gauge invariant for the same reason as for the normal charge polarization. To generalize the idea of the total polarization, one can write the polarization including all occupied bands as

$$P_T \bmod 2 = \sum_n P_T(n) \bmod 2 = \frac{i}{\pi} \log \frac{\sqrt{\det B(\pi)}\mathrm{Pf}(B(0))}{\mathrm{Pf}(B(\pi))\sqrt{\det B(0)}}, \tag{2.72}$$

where we have introduced the $2N$ block matrix $B = \otimes_i B_{nn} = B_{1,1} \otimes B_{2,2} ... \otimes B_{N,N}$, with N being the number of occupied Kramers pairs. Due to the special form of P_T, using this block structure we directly see that any unitary transformation in the space $U(2N)$ leaves P_T invariant. This allows us to choose a more convenient definition of the sewing matrix,

$$(B)_{\alpha\beta} = \langle u_\alpha(-\mathbf{k})|\mathcal{T}|u_\beta(\mathbf{k})\rangle \,, \tag{2.73}$$

where α, β run now over all occupied bands. By using now the definition (2.66) with P_T, we get a gauge-invariant measure

$$[P_T(\gamma(\Gamma, X)) - P_T(\gamma(Y, M))] \bmod 2 \tag{2.74}$$

for the charge pumping of the Wannier centers over half the cycle orthogonal to k_x. After half a cycle, the system returns to a TR invariant $d = 1$-system where the Wannier states can recombine with other TR solutions or the same TR partners, which results in the possible appearance of unpaired Wannier states in an *open* system at each boundary. The even- or oddness of these switches defines the $\mathbb{Z}_2$ index, which can also be written as

$$I_{d=2}(\mathbb{Z}_2) = \prod_{i=1}^{4} \frac{\sqrt{\det(B(\Lambda_i))}}{\mathrm{Pf}(B(\Lambda_i))} \tag{2.75}$$

with the sewing matrix evaluated at the TRIM points. Before we generalize this invariant for the $d = 3$ case, let us give two other equivalent formulations of this invariant.

A) Pfaffian formulation

The first formulation allows us to use a line integral to calculate the invariant. In Ref. [30] it has been shown that Eq. (2.75) is equivalent to the topological index counting the number of zeros of the *Pfaffian* $P(\mathbf{k}) = \mathrm{Pf}(\langle u(\mathbf{k})|\mathcal{T}|u(\mathbf{k})\rangle)$ and their vorticities defined by

$$I_{d=2}(\mathbb{Z}_2) = \frac{1}{2\pi i} \oint_{\mathcal{C}} d\mathbf{k} \cdot \nabla_{\mathbf{k}} \log\left[P(\mathbf{p}) + i\delta\right] \bmod 2, \tag{2.76}$$

where $\mathcal{C}$ is the contour over the half BZ such that the states with quantum number $-\mathbf{k}$

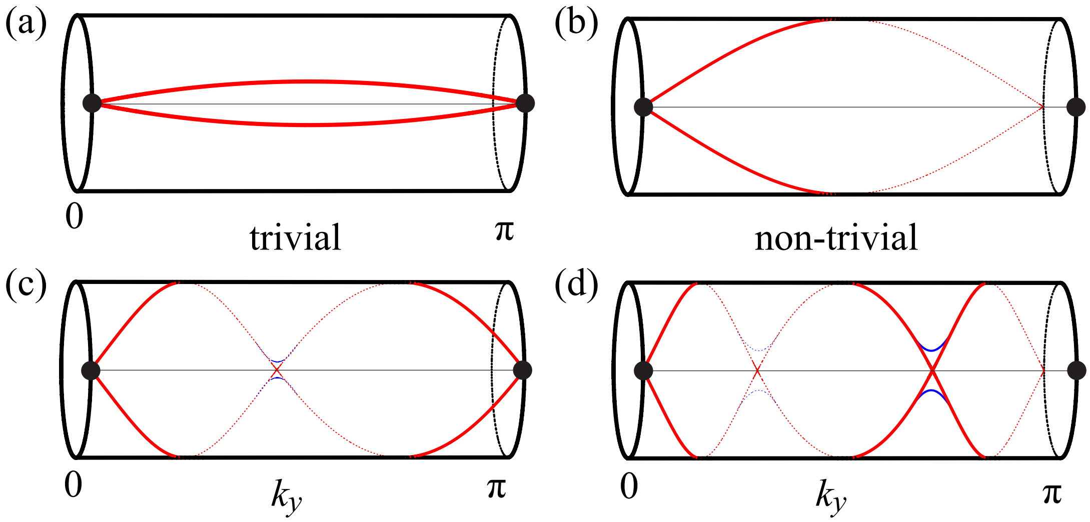

Figure 2.11: Schematic tracking of the Wannier centers with different windings for the trivial ((a) and (c)) and the non-trivial phase ((b) and (d)). The crossings can become anti-crossings after adding TR preserving perturbations.

and $+\mathbf{k}$ are separated.

B) Wannier-center formulation

The second formulation gives a more intuitive view on this new invariant Eq. (2.75). For that, we look at the evolution of the Wannier function centers by defining an alternative position operator [35]

$$\hat{x}(N) = \sum_{i=1}^{N} \sum_{n} e^{-i\frac{2\pi}{N}R_i} \left|\mathbf{\Psi}_n(R_i; k_y, k_z, ..., k_d)\right\rangle \left\langle \mathbf{\Psi}_n(R_i; k_y, k_z, ..., k_d)\right| \tag{2.77}$$

for a lattice with PBC, lattice constant $a = 1$ and N unit cells. This operator is unitary and its phase $U(1) \simeq \mathbb{S}^1$ represents the position of the Wannier centers. By tuning k_y (or any other component) from 0 to π we can track the expectation value of this quantity on a circle $\mathbb{S}^1$. The position of each Wannier center can therefore effectively be described by a point on a cylinder $[0, \pi] \times \mathbb{S}^1$. At $k_y = 0$ and $k_y = \pi$, the positions of Wannier states appear in pairs due to TR symmetry. By moving away from them, the pairs in general split and recombine. Each Wannier center pair thereby encloses the whole cylinder an integer number of times. This allows us to define a *winding number* as illustrated in Fig. 2.11. The winding number appears to be an integer. However, as one can see from Fig. 2.11 (c), (d), in which the original paths wind two or three times around the cylinder, the topological invariant cannot be an integer. Possible crossing points of the closed path are accidental. Only at the TRIM points we have Kramers theorem to protect degeneracies. TR symmetric perturbations can therefore turn the crossings into anti-crossings. Hence, the perturbed path has a winding number of 0 or 1, respectively. This is discussed extensively in Ref. [35] using the *non-abelian Berry connection*. Thus, the topological invariant for each band is $\mathbb{Z}_2$. This idea can be directly applied to multi-band systems where we have to consider all occupied bands, not only one. The $\mathbb{Z}_2$ invariant for a two-dimensional system is then equal to the summed winding numbers of all the pairs modulo 2.

All these definitions can be extended also to 3 dimensions [36, 37] which is nothing more than to reconsider a $d = 3$ system in terms of two $d = 2$ systems – two planes in the BZ at $k_z = 0$ and π connected along k_z. Either both systems have the same $I_{d=2}(\mathbb{Z}_2)$ (trivial or weak TI), then they can be considered as a system made of stacked two-dimensional systems, or the indices are different (strong TI) such that we have to introduce a new invariant. The *strong index* is defined as the product of the two $d = 2$ invariants

$$(-1)^{\nu_0} \equiv I_{d=3}(\mathbb{Z}_2) = I_{d=2}(k_z = 0) I_{d=2}(k_z = \pi) = \prod_{i=1}^{8} \delta_i, \text{ where } \delta_i = \frac{\sqrt{\det(B(\Lambda_i))}}{\mathrm{Pf}(B(\Lambda_i))} \tag{2.78}$$

evaluated at the 8 TRIM points of the BZ. Besides the strong index ν_0 one has also 3 weak indices (ν_1, ν_2, ν_3) which are the two-dimensional indices of the three TR-invariant corner-sharing planes excluding the Γ point. This leads to $2^4 = 16$ topologically distinct phases.

The most important difference is that a strong TI has a topologically protected surface state independent of the termination. The weak indices of a weak TI can be interpreted as *Miller indices* characterizing the layers of the stacking by $\mathbf{G} = \nu_1 \mathbf{b}_1 + \nu_2 \mathbf{b}_2 + \nu_3 \mathbf{b}_3$ modulo twice a reciprocal lattice vector, where $\mathbf{b}_i$ are the primitive lattice vectors. Along the stacking direction we find no topologically protected surface states.

2.7 The axion response and the Dirac cone

As we already have shown for the Chern number, the occurrence of topological non-triviality leads to a Chern-Simons term in the electromagnetic response describing the QHE physics. One can ask what is the physical response of a strong TR invariant TI. For our purposes the most relevant one is the $d = 3$ response, which is again connected to basic electromagnetic properties of solids, like the *dielectric constant* or the *magnetic* *permeability*. Doing an equivalent consideration like for TR broken systems, one gets a term in the expansion which is the so-called *magnetoelectric polarization* encoded in the effective theory [38, 26]

$$S_{3D} = \frac{1}{4\pi}\int d^3r dt\, \varepsilon^{\mu\nu\varrho\tau} P_3(\mathbf{r},t)\partial_\mu A_\nu \partial_\varrho A_\tau = \frac{1}{2\pi}\int d^3r dt\, P_3(\mathbf{r},t)\mathbf{E}(\mathbf{r},t)\cdot\mathbf{B}(\mathbf{r},t), \quad (2.79)$$

where P_3 describes the non-linear coupling between the electric $\mathbf{E}$ and the magnetic field $\mathbf{B}$. This action is known from the *axion electrodynamics*. However, assuming that we consider the theory in a *closed* space-time manifold with PBC we get [26, 39]

$$\frac{1}{2\pi}\int d^3r dt\, \mathbf{E}(\mathbf{r},t)\cdot\mathbf{B}(\mathbf{r},t) = 2\pi m \ (m \in \mathbf{Z}), \quad (2.80)$$

which leads to the equivalence relation [24]: $e^{iS_{3d}(P_3)} = e^{iS_{3d}(P_3+m)}$ $(m \in \mathbb{Z})$ saying that the homogenous axion P_3 is defined up to an integer. The parameter P_3 can describe trivial and non-trivial insulators with an arbitrary value in the regime $[0, 1)$. The important point is that the TR symmetry fixes the value of P_3. The term $\mathbf{E}\cdot\mathbf{B}$ is *odd* under TR symmetry. This means that we have to ensure $e^{-iS_{3d}(P_3)} = e^{iS_{3d}(-P_3)} = e^{iS_{3d}(P_3)}$. The $\mathbb{Z}_2$ invariant is hidden in the parameter P_3 which can take only the values 0 (trivial) or 1/2 (non-trivial) in a homogeneous material. This result also holds if one consider an open system, although the integer m has now a physical meaning. It describes the even number of Dirac cones, which are not topologically protected by the bulk system. They can be in principle gapped out by surface TR breaking terms added to the open system.

Using the *variational principle* we get direct access to its physical response

$$j^\mu = \frac{1}{2\pi}\varepsilon^{\mu\nu\varrho\tau}\partial_\nu P_3 \partial_\varrho A_\tau, \quad (2.81)$$

where the gradient of P_3 shows that one need a heterostructure. Assuming a TI in contact with a trivial insulator along the z-direction where all the other non-topologically protected contributions are 0 one can write

$$P_3 = \frac{1}{2}\theta(z) \text{ and } \partial_z P_3 = \frac{1}{2}\delta(z) \quad (2.82)$$

such that the spatial gradient of the magnetoelectric polarization induces a *half*-integer Hall effect

$$j_y = \frac{1}{2}\frac{1}{2\pi}E_x, \quad (2.83)$$

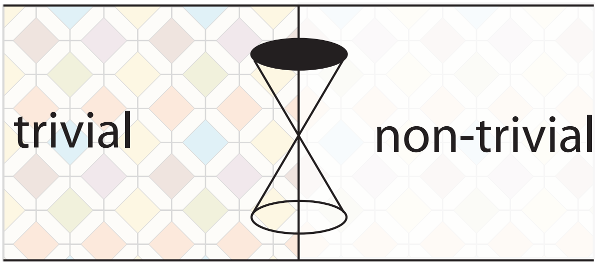

Figure 2.12: Idealized interface between a topologically non-trivial and trivial material. The simplest low-energy theory respecting TR symmetry and giving a half-integer QHE is the Dirac cone.

in the presence of an electric field E_x. This is consistent with a two-dimensional *Dirac cone* sitting on the surface which have the same response under an external electromagnetic perturbation. At the interface among the two topologically different states of matter the bulk band gap has to vanish without an electric field. This is the generic picture of the 3d TR invariant systems and the *bulk-edge correspondence* for such systems. The success of ARPES with its surface sensibility enables us to directly study those states providing a window into the bulk physics and into topology. However, the Dirac cone is only an idealized representative (see Fig. 2.12) and the real edge spectrum may look much more complicated.

The last question is how we can calculate P_3. Assuming a non-interacting system the magnetoelectric polarization P_3 can be expressed using the fermionic system by

$$P_3 = \frac{1}{16\pi^2}\int d^3k \varepsilon_{ijk} \mathrm{Tr}[(f_{ij}(\mathbf{k}) - \frac{2}{3} i a_i(\mathbf{k}) a_j(\mathbf{k})) a_k(\mathbf{k})] \tag{2.84}$$

or in an another gauge $a_i' = u^{-1} a_i u - i u^{-1} \partial_i u$ where

$$P_3' = P_3 + \frac{1}{2\pi^2}\int d^3k \varepsilon^{0ijk} \mathrm{tr}\left[(u^{-1}\partial_i u)(u^{-1}\partial_j u)(u^{-1}\partial_k u)\right], \tag{2.85}$$

with $f_{ij}(\mathbf{k}) = \partial_{k_i} a_j(\mathbf{k}) - \partial_{k_j} a_i(\mathbf{k}) + i[a_i(\mathbf{k}), a_j(\mathbf{k})]$ and the non-abelian Berry vector potential $(a_i(\mathbf{k}))_{\alpha\beta} = \langle u_\alpha(\mathbf{k})| i\partial_{k_i} | u_\beta(\mathbf{k})\rangle$ for the occupied bands. The corresponding Green function approach is discussed in Ref. [27].

3 Low-energy physics and the effect of boundaries

The topological invariants we encountered in the previous chapter are well-defined since the basis manifold $\mathcal{M}$ and the target manifold are *compact*. These are manifolds without a boundary such as a circle, the n-sphere or the n-torus. In condensed matter physics the crystal structure of a solid implies that the basis manifold is a torus $\mathbb{T}_d$ in d dimensions, which corresponds to the Brillouin zone (BZ). The target manifold instead is the Bloch Hamiltonian, which is compact as well. Apparently, low-energy continuum theories are different. They describe a dispersion over $\mathbb{R}^d$ instead of the BZ. At a first sight there is no connection to any compact manifold since by expanding at low-energy points of a lattice model we loose the compactness of the basis manifold, as illustrated in Fig. 3.1

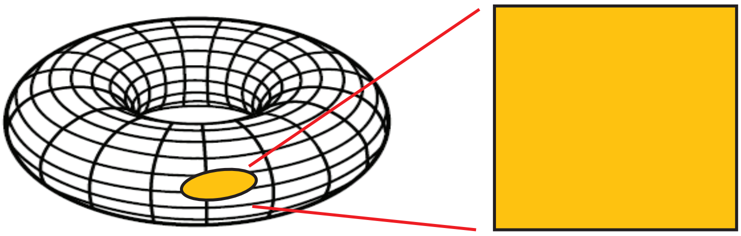

Figure 3.1: The BZ is a torus in d dimensions. The low-energy expansion is described by a continuum theory living on $\mathbb{R}^d$, which describes only a part of the torus.

3.1 Topological Marginality

Let us analyze a massive Dirac equation in three dimensions

$$\mathcal{H}_{Dirac} = A\boldsymbol{\alpha} \cdot \hat{\mathbf{p}} + M\beta, \tag{3.1}$$

where the matrices α_i and β are defined in appendix A. This system is insulating for $M \neq 0$ and belongs to the AZ symmetry class DIII. Using Tab. 2.1, the topological invariant is a $\mathbb{Z}$

number. The definition of this topological invariant can be found in Ref. [40]. Surprisingly, a direct calculation, which is evaluated in paragraph 4.6 explicitly, shows that this number is only half-integer ($N = 1/2$). A similar situation was found in the SSH model discussed in the previous chapter. The $\mathbb{Z}$ topological invariant in the lattice model was integer, but a linearized low-energy model gave a half-integer value. One could say that these states are neither topologically trivial nor non-trivial. The appearance of half-integer numbers is referred to as *topological marginality* [40], and comes about the non-compactness of the underlying effective theory.

From a continuum theory perspective, a non-interacting, insulating system can therefore exist in three phases: the topologically *trivial* insulating, the topologically *non-trivial* insulating or the topologically *marginal* insulating phase. As we have demonstrated for the SSH model, higher order terms in the continuum model can change the topology of effective theories from marginal to non-trivial without closing the gap. The argument for a generic model can be found in Ref. [41] which highlights how effective theories can show a crucial dependence on the high-energy part of the spectrum.

In chapters 4 and 5 we will show how marginality affects the significance of long-wavelength models. Before doing this, we will present in this chapter the basics of continuum $\mathbf{k}\cdot\mathbf{p}$ models and the techniques relevant to analyze the occurrence of edge and surface states.

3.2 The extended $\mathbf{k}\cdot\mathbf{p}$ method

First of all, we introduce the $\mathbf{k}\cdot\mathbf{p}$ theory. The Hamiltonian for non-interacting electrons in a crystal can be written in first quantization as

$$H_{el} = \sum_i \frac{\mathbf{p}_i^2}{2m} + V(\mathbf{r}_i) + \frac{1}{2m^2c^2}(\mathbf{s}_i \times \nabla V(\mathbf{r}_i)) \cdot \mathbf{p}_i, \tag{3.2}$$

where $\{\mathbf{x}_i, \mathbf{p}_i, \mathbf{s}_i\}$ describe the position, the momentum and the spin of the electron i with an effective mass m in an effective potential V describing the lattice of ions. The last part of the Hamiltonian accounts for the spin-orbit coupling (SOC). *Bloch theorem* guarantees that the electronic wavefunction can be characterized by a band index n (including the spin) and the crystal momentum $\mathbf{k}$, and can be written as

$$\Psi_{n,\mathbf{k}} = u_{n,\mathbf{k}}(\mathbf{r}) \frac{1}{\sqrt{\mathcal{V}}} e^{i\mathbf{k}\cdot\mathbf{r}} \text{ with } u_{n,\mathbf{k}}(\mathbf{r} + \mathbf{a}_l) = u_{n,\mathbf{k}}(\mathbf{r}), \tag{3.3}$$

where we introduced the volume $\mathcal{V}$ of the crystal to normalize the eigenstate. The secular equation for the *envelope functions* $u_{n,\mathbf{k}}$ reads then

$$\left[\frac{(\mathbf{p}+\mathbf{k})^2}{2m}+V+\frac{1}{2m^2c^2}(\mathbf{s}\times\nabla V)(\mathbf{p}+\mathbf{k})\right]u_{n,\mathbf{k}}=E_{n,\mathbf{k}}u_{n,\mathbf{k}}. \tag{3.4}$$

The $\mathbf{k}\cdot\mathbf{p}$ method is based on the fact that the essential physical properties depend on a small energy window near the Fermi level describing the low-energy excitations. Let us assume that $\mathbf{k}_0$ is the crystal momentum where the low-energy excitations reside. Then the secular equation can be written as

$$\left[H_{\mathbf{k}=\mathbf{k}_0}+\frac{(\mathbf{k}-\mathbf{k}_0)^2}{2m}+\frac{\mathbf{k}-\mathbf{k}_0}{m}\cdot(\boldsymbol{\pi}+\mathbf{k}_0)\right]u_{n,\mathbf{k}}=E_{n,\mathbf{k}}u_{n,\mathbf{k}} \tag{3.5}$$

with $\boldsymbol{\pi}=\mathbf{p}+(\mathbf{s}\times\nabla V)/(2mc^2)$. Assuming all eigenvalues $E_{n,\mathbf{k}_0}$ at $\mathbf{k}_0$ are non degenerate, we can treat this Hamiltonian using non-degenerate perturbation theory. The result of this method up to the second-order is given by

$$\begin{aligned}
E^{(0)}_{n,\mathbf{k}}&=E_{n,\mathbf{k}_0},\\
E^{(1)}_{n,\mathbf{k}}&=E^{(0)}_{n,\mathbf{k}}+\frac{\mathbf{k}-\mathbf{k}_0}{m}\cdot\left(\langle n,\mathbf{k}_0|\boldsymbol{\pi}|n,\mathbf{k}_0\rangle+\mathbf{k}_0\right)\text{ and}\\
E^{(2)}_{n,\mathbf{k}}&=E^{(1)}_{n,\mathbf{k}}+\frac{(\hat{m}^{-1})_{\alpha\beta}}{2}(\mathbf{k}-\mathbf{k}_0)_\alpha(\mathbf{k}-\mathbf{k}_0)_\beta
\end{aligned} \tag{3.6}$$

with the *effective mass* tensor

$$(\hat{m}^{-1})_{\alpha\beta}=m^{-1}\delta_{\alpha\beta}+\frac{2}{m^2}\sum_{l\neq n}\frac{\langle n,\mathbf{k}_0|\pi_\alpha|l,\mathbf{k}_0\rangle\,\langle l,\mathbf{k}_0|\pi_\beta|n,\mathbf{k}_0\rangle}{E_{n,\mathbf{k}_0}-E_{l,\mathbf{k}_0}}. \tag{3.7}$$

This technique can be extended to (quasi-)degenerate bands using *quasi-degenerate perturbation theory*, thanks to which the *Kohn-Luttinger* model [42] or the *Kane* model [43] can be derived. The method is nearly equivalent except that the perturbative part of the Hamiltonian has two weakly interacting subsets (A and B) where the elements of the relevant subset A are (quasi-)degenerate at $\mathbf{k}_0$. The perturbative Hamiltonian of subset A up to the second order in momentum is then given by

$$\left(h^{(2)}_{\mathbf{k}}\right)_{aa'}=\left(h^{(2)}_{\mathbf{k}_0}\right)_{aa'}+\frac{1}{2}\sum_{b\in B}\langle a|\,h^{(1)}_{\mathbf{k}_0}\,|b\rangle\,\langle b|\,h^{(1)}_{\mathbf{k}_0}\,|a'\rangle\left(\frac{1}{E_{a,\mathbf{k}_0}-E_{b,\mathbf{k}_0}}+\frac{1}{E_{a',\mathbf{k}_0}-E_{b,\mathbf{k}_0}}\right), \tag{3.8}$$

where the $h^{(i)}_{\mathbf{k}_0}$ describe the series around $\mathbf{k}_0$ up to the i-th order of the full Hamiltonian. This is a formal way to define an effective $\mathbf{k}\cdot\mathbf{p}$ Hamiltonian that gives exactly the low-lying energy states. We want to remark that this matrix structure of the Hamiltonian can be also derived using the so-called *theory of invariants* as shown in Ref. [44]. Independent of the technique we choose, the effective theory is of the form

$$H(\delta\mathbf{k}) = H(\mathbf{k}_0) + H'_\alpha(\mathbf{k}_0)\delta k_\alpha + H''_{\alpha\beta}(\mathbf{k}_0)\delta k_\alpha \delta k_\beta + ... \tag{3.9}$$

with $\mathbf{k}$-independent matrices/parameters capturing the physics of the low-energy excitations. The material-dependent parameters in this expansion can be derived by density functional theory (DFT), linear combination of atomic orbitals (LCAO), or after an expansion of a designed TB Hamiltonian.

Since the bulk-edge correspondence is the physical consequence of topologically non-trivial states of matter, we now show how to calculate surface and edge states in the $\mathbf{k}\cdot\mathbf{p}$ framework. Introducing an edge implies a breaking of the lattice translational symmetry. The momentum $\mathbf{k}$ is not a good quantum number anymore. However, a low-energy description of surfaces, or heterostructures can still be incorporated by applying two changes to the $\mathbf{k}\cdot\mathbf{p}$ Hamiltonian. The first one is the substitution

$$\delta\mathbf{k} \to \mathbf{p} = -i\nabla \text{ because } -i\nabla e^{i\delta\mathbf{k}\cdot\mathbf{r}} = \delta\mathbf{k}e^{i\delta\mathbf{k}\cdot\mathbf{r}}. \tag{3.10}$$

The second change covers the fact that all parameters appearing in the low-energy expansion can depend on the position $\mathbf{r}$. For the latter, we need to build up a quantum mechanically well-defined model. The canonical conjugate operators $\{\mathbf{r},\mathbf{p}\}$ do no commute with each other. Therefore, one has to choose a symmetrized Hamiltonian guaranteeing the *hermiticity* (*self-adjointness*) of the model. This can be done for each individual element of the Hamiltonian as

$$f(\mathbf{r})k_i \to \frac{1}{2}(p_i f(\mathbf{r}) + f(\mathbf{r})p_i) \text{ or } f(\mathbf{r})k_i k_j \to \frac{1}{2}(p_i f(\mathbf{r})p_j + p_j f(\mathbf{r})p_i). \tag{3.11}$$

This symmetrization procedure is not the only way to write down a quantum-mechanically well-posed system. There are indeed infinite many other ways. This arbitrariness of the symmetrization has led Burt to derive another ordering, which is known as the *Burt-Foreman ordering* [45]. As we find, independent of the symmetrization procedure we get in the end a *partial matrix differential equation* of order n after the expansion up to the n-th order. This method been successfully applied to the calculation of energy bands in GaAs/$\mathrm{Ga_{1-x}A1_xAs}$-type [46] and $\mathrm{Hg}_{1-y}\mathrm{Mn}_y\mathrm{Te}$-type [47] quantum wells.

3.3 Ellipticity and spurious solutions

A discussed problem in these matrix differential equations is the presence of so-called *spurious solutions*. Solving these equations leads to *unphysical* states, which are sensitive to the chosen discretization scheme and the mesh width. Their energies often lie inside a band gap and are localized close to the boundary. The reason for the presence of spurious solutions is often the absence of *ellipticity* [48] in the differential equation. Ellipticity is a property known from the theory of partial differential equations. Let us for example assume a heterostructure in d dimensions with a matrix differential equation of order n. We can characterize the high energy term of the $\mathbf{k}\cdot\mathbf{p}$ Hamiltonian for a system with a finite band gap by

$$H \cong ... + \begin{pmatrix} \sum\limits_{m_1+m_2+...m_d=n} H_{CB}^{\{m\}} p_x^{m_1} p_y^{m_2} ... p_d^{m_d} & 0 \\ 0 & \sum\limits_{m_1+m_2+...m_d=n} H_{VB}^{\{m\}} p_x^{m_1} p_y^{m_2} ... p_d^{m_d} \end{pmatrix}, \quad (3.12)$$

where n is the order of matrix differential equation and H_{CB}/H_{VB} are the position-dependent effective matrices of the conduction (CB) and the valence bands (VB). The requiring property for an elliptic differential equation is that the matrices where we substitute the n $\mathbf{p}$-operators by numbers of the vector $\mathbf{g} \in \mathbb{R}^n$

$$\tilde{H}_{CB/VB} = \frac{1}{|\mathbf{g}|^n} \sum_{m_1+m_2+...m_d=n} H_{CB/VB}^{\{m\}} g_x^{m_1} g_y^{m_2} ... g_d^{m_d} \quad (3.13)$$

are positive (negative) and negative (positive) respectively for all positions and directions in the n-dimensional space of $\mathbf{g}$. Positivity means that all eigenvalues of a matrix are positive.

Since spurious solutions are often associated with the violation of ellipticity [48], we want to ensure an elliptic $\mathbf{k}\cdot\mathbf{p}$ model in order to analyze the occurrence of surface and interface states due to topologically non-trivial properties. Moreover, we want to have at hand a model where the ambiguity in the symmetrization procedure discussed in the previous section is absent. For an heterostructure, this can be achieved by considering a sharp transition between two materials with properties A and B (cf. Fig. 3.2). In this case one has to find good *matching conditions* [49] of the wave function. For an interface with the vacuum instead we can consider the $\mathbf{k}\cdot\mathbf{p}$ problem in a half-infinite space. This allows us to describe the full problem by a single $\mathbf{k}\cdot\mathbf{p}$ Hamiltonian with properties A. The *effective*

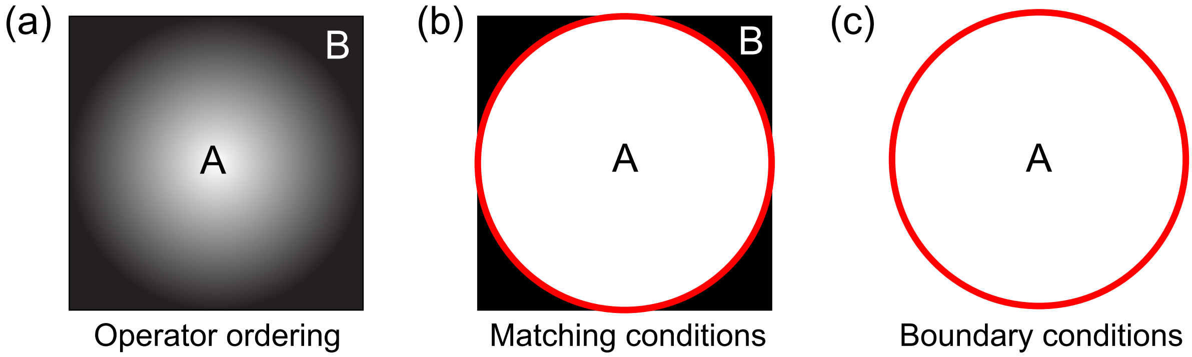

Figure 3.2: The approximation scheme to avoid the *operator ordering problem* (a) brings us to a new problem illustrated in panel (b) and (c) known as the *matching condition* and the *boundary condition* problem.

Schrödinger or *Dirac* problem in $d = 1$ can be written as a general Hamiltonian of the form

$$\hat{H} = \hat{A}\hat{p}^2 + 2\hat{B}\hat{p} + \hat{C} \text{ with } \hat{p} = -i\partial_x \tag{3.14}$$

built up by arbitrary Hermitian matrices $\hat{A}$, $\hat{B}$ and $\hat{C}$ – which are constant. The boundary is fixed to be at $x = 0$ while the half space in which we are interested is defined by $x > 0$. If we have a finite matrix $\hat{A}$ we are in the Schrödinger case and we have to check the property of ellipticity by analyzing the eigenvalues of $\hat{A}$. The eigenvalues of the conduction and valence bands have to be positive and negative respectively. In the Dirac case $(\hat{A} = 0, \hat{B} \neq 0)$ we have to do the same for matrix $\hat{B}$.

3.4 Self-adjoint extensions

Let us now assume we have an elliptic Hamiltonian for which we want to solve the eigenvalue problem in the half-infinite space. In the real space $(-\infty, \infty)$ we have unique operators $\hat{x}$ and $\hat{p}$ with the commutator relation $[\hat{x}, \hat{p}] = i$. However, in the half-infinite space $[0, \infty)$ we need new quantum-mechanical operators. The position operator is *bounded from below*: $\langle\hat{x}\rangle \geq 0$. Therefore the momentum operator cannot be defined as in the free case. The momentum is no longer a measurable quantity in that situation [50]. Other operators $\hat{A}(\hat{x}, \hat{p})$ which are combinations of the free operators $\hat{x}$ and $\hat{p}$ can be well-defined instead using the so-called *self-adjoint extensions*. To make this a little bit more systematic let us define the mathematics. All physically relevant operators must be *symmetric*, which means that

$$\langle \Psi | \hat{A}\Phi \rangle = \langle \hat{A}\Psi | \Phi \rangle \;\text{ for all }\; |\Psi\rangle, |\Phi\rangle \in \mathcal{D}(\hat{A}) \subset \mathbb{H}, \tag{3.15}$$

where $\mathbb{H}$ is the complex, separable Hilbert space and $\mathcal{D}(\hat{A})$ the dense domain of the unbounded, linear operator $\hat{A}$. This is in general not enough to ensure self-adjointness. If we want a self-adjoint operator we need that the operator is symmetric and that the domain of the adjoint operator $\mathcal{D}(\hat{A}^\dagger)$ is equal to $\mathcal{D}(\hat{A})$. The set $\mathcal{D}(\hat{A}^\dagger)$ is defined as the set of all $|\Psi\rangle \in \mathbb{H}$ for which a $\xi \in \mathbb{H}$ exists so that

$$\langle \Psi | \hat{A}\Phi \rangle = \langle \xi | \Phi \rangle \;\text{ for all }\; |\Phi\rangle \in \mathcal{D}(\hat{A}) \text{ with } |\hat{A}^\dagger \Psi\rangle := |\xi\rangle\,. \tag{3.16}$$

With this we can define for every symmetric operator the so called *deficiency spaces*

$$\mathcal{N}_\pm = \{(A^\dagger \mp i\mu)\,|\Psi\rangle = 0 \text{ with } |\Psi\rangle \in \mathbb{H}\}, \tag{3.17}$$

where $\mu > 0$ to preserve the units and the *deficiency indices* $n_\pm = \dim \mathcal{N}_\pm$. The criterion for self-adjointness is given by *von Neumann's* theorem: Let $\hat{A}$ be a symmetric operator with deficiency indices n_+ and n_- then

1. $\hat{A}$ is self-adjoint if and only if $n_+ = n_- = 0$.
2. $\hat{A}$ admits self-adjoint extensions if and only if $n_+ = n_- \neq 0$.
3. $\hat{A}$ has no self-adjoint extensions if and only if $n_+ \neq n_-$.

The extension is given by the domain

$$\mathcal{D}(\hat{A}_\mathcal{U}) = \{\Phi := \Psi + (\mathbb{1} + \mathcal{U})\xi \text{ where } \Psi \in \mathcal{D}(\hat{A}), \xi \in \mathcal{N}_+\}, \tag{3.18}$$

where $\mathcal{U}$ describes the unitary mapping between $\mathcal{N}_+ \to \mathcal{N}_-$ and the operator acts like $\hat{A}_\mathcal{U}\Phi = \hat{A}^\dagger(\Psi + (\mathbb{1} + \mathcal{U})\xi)$. A full theory has been built up to solve these problems and is given in many text-books about unbounded differential operators, e.g. Ref. [51]. The role of these self-adjoint extensions in the field of TIs is discussed in Ref. [52] and Ref. [53]. The interesting fact is that one can reinterpret the manifold $\mathcal{U}$ determining the self-adjoint extensions with boundary conditions (BCs) [54].

3.5 Boundary conditions

The relation between self-adjoint extensions and BCs becomes transparent by using a Lagrange formulation. This has been pointed out in Ref. [55]. Let us study a generalized Schrödinger Hamiltonian in a *Lagrangian* form

$$\mathcal{L}_\Omega =(\partial_x \Psi_i^*) A_{ij} (\partial_x \Psi_j) - iB_{ij} \Psi_i^* \overset{\leftrightarrow}{\partial_x} \Psi_j + (C_{ij} - E\delta_{ij})\Psi_i^* \Psi_j, \tag{3.19}$$

where E is the energy of the corresponding secular equation and the *Janus* operator $\overset{\leftrightarrow}{\partial_x} \equiv \overset{\rightarrow}{\partial_x} - \overset{\leftarrow}{\partial_x}$ with the arrows pointing in the direction where the derivative acts. The Lagrangian $\mathcal{L}_\Omega$ is the bulk Lagrangian. Terms which are missing are given by the surface Lagrangian

$$\Delta\mathcal{L}_\Omega =\partial_x \left(-i\tilde{A}_{ij} \Psi_i^* \overset{\leftrightarrow}{\partial_x} \Psi_j + \tilde{B}_{ij} \partial_x (\Psi_i^* \Psi_j) + \tilde{C}_{ij} \Psi_i^* \Psi_j\right) \tag{3.20}$$

written as a total derivative with arbitrary Hermitian matrices $\tilde{A}$, $\tilde{B}$ and $\tilde{C}$ completely unrelated to the Hamiltonian matrices. It is well-known that such terms can be ignored over $\mathbb{R}$ and leads to equivalence class ($\mathcal{L} \cong \mathcal{L} + \Delta\mathcal{L}$). In an infinite system the wave-function has to vanish at the boundary ($\Psi_j(|x| \to \infty) \to 0$) so that $\Delta\mathcal{L}_\Omega$ is not effective. For us instead it plays an important role. It does not vanish by the integration from 0 and ∞. After setting the problem with the action

$$\mathcal{S}[\Psi^*, \Psi] = \int_\Omega dV \; (\mathcal{L}_\Omega + \Delta\mathcal{L}_\Omega), \tag{3.21}$$

we can apply the variational approach $\delta\mathcal{S}[\Psi^*, \Psi] = 0$ to find the *matrix differential equation*. The variational approach gives us an elegant way to get the corresponding equations for Ψ and its Hermitian conjugate Ψ^*. By construction we know that both equations describe the same state, and we only need to consider a variation with respect to Ψ^* as can be seen from the total differential

$$\delta\mathcal{S}[\Psi^*, \Psi] = \int \frac{\delta\mathcal{S}[\Psi^*, \Psi]}{\delta\Psi_i^*} \delta\Psi_i^* + \int \frac{\delta\mathcal{S}[\Psi^*, \Psi]}{\delta\Psi_i} \delta\Psi_i, \tag{3.22}$$

where the second part is the Hermitian conjugate part of the first. One can write

$$\begin{aligned} &\delta\mathcal{S}[\Psi^*] - \int_\Omega dx \; \delta\Psi_i^* (H_{ij} - E\delta_{ij}) \Psi_j \\ =& + \left[(A_{ij} + \tilde{B}_{ij} - i\tilde{A}_{ij})(\partial_x \Psi_j) + (\tilde{C}_{ij} + iB_{ij})\Psi_j\right] \delta\Psi_i^* \Big|_{\partial\Omega} \\ &+ \left[(\tilde{B}_{ij} + i\tilde{A}_{ij})\Psi_j\right] \partial_x \delta\Psi_i^* \Big|_{\partial\Omega} . \end{aligned} \tag{3.23}$$

Now we can vary $\partial_x \delta\Psi^*$ and $\delta\Psi^*$ arbitrarily, and thus we reobtain the bulk Schrödinger equation with two new equations reading

$$0 = (A_{ij} + \tilde{B}_{ij} - i\tilde{A}_{ij})\,(\partial_x \Psi_j)\big|_{x=0} + (\tilde{C}_{ij} + iB_{ij})\Psi_j(0), \text{ and } 0 = (\tilde{B}_{ij} + i\tilde{A}_{ij})\Psi_j(0) \quad (3.24)$$

which describe the BCs. Next, one has to prove that all these operators with the new BCs build up a *Hermitian* model on the semi-axis. The condition that the operator is symmetric

$$\int_0^\infty dx \Phi_i^* (H_{ij}(\partial_x) - H_{ij}(\overleftarrow{\partial_x}))\Psi_j = - \left. \Phi_i^* A_{ij} \overleftrightarrow{\partial_x} \Psi_j - 2i\Phi_i^* B_{ij} \Psi_j \right|_{\partial\Omega} = 0 \quad (3.25)$$

is fulfilled for all BCs. The second condition is valid by construction. Nevertheless, we are left with two BC equations, which have to be concomitantly solved.

One solution is given by setting $\tilde{B} = -A$ and $\tilde{A} = 0$. We find the so-called fixed BC (FBC) if the matrix A is elliptic and so all its eigenvalues are non-zero. A more commonly used solution can be found if we set $\tilde{B} = 0$ and $\tilde{A} = 0$. The first equation is then sufficient enough and the BCs can be written as

$$(\hat{J} + i\hat{\eta})\,|\Psi\rangle\Big|_{x=0} = 0 \text{ with } \hat{J} := \frac{1}{2}\frac{\partial H}{\partial \hat{p}} = \hat{A}\hat{p} + \hat{B} \quad (3.26)$$

the probability current operator and an arbitrary Hermitian operator $\hat{\eta}$. The FBC is recovered in the $\hat{\eta} \to \infty$ limit. The $\hat{\eta} = 0$ case corresponds instead to natural boundary conditions (NBC). The Hermitian operator $\hat{\eta}$ can be reinterpreted by noticing that the Lagrangian

$$\int_0^\infty dx\, \Delta\mathcal{L}_\Omega = - \int_0^\infty dx\, \partial_x \langle\Psi|\eta|\Psi\rangle = - \int_0^\infty dx\, \langle\Psi|\eta\delta(x-\varepsilon)|\Psi\rangle\,, \quad (3.27)$$

where $\varepsilon \to 0$. Therefore the BCs can be written as a physical boundary potential $V(x) = \eta\delta(x-\varepsilon)$, as discussed in Ref. [56].

To analyze the role of these boundary potentials let us study the example of a free non-relativistic particle on a semi-axis. Starting with the standard action on an interval $[0,\infty)$

$$\mathcal{S}(E,\Psi,\Psi^*) = \int_0^\infty dx\, \mathcal{L}, \text{ where } \mathcal{L} = \mathcal{L}(E,\Psi(x),\Psi^*(x)) \quad (3.28)$$

with the Lagrangian

$$\mathcal{L} = \frac{1}{2m}\partial_x\Psi^*\partial_x\Psi - E\Psi^*\Psi - \eta\delta(x-\varepsilon)\Psi^*\Psi \tag{3.29}$$

for a particle of mass m and energy E, we use the variational principle to get the ordinary Schrödinger equation

$$H\Psi = -\frac{1}{2m}\partial_x^2\Psi = E\Psi \text{ and } \left(\frac{1}{2m}(-i\partial_x) - i\eta\right)\Psi\bigg|_{x=0} = 0. \tag{3.30}$$

After the rescaling $2m\eta \to \eta$, the generalized BCs are

$$\partial_x\Psi\cos\nu + \Psi\sin\nu = 0 \text{ with } \nu \in [-\pi/2, \pi/2) \text{ and } \eta = \tan\nu. \tag{3.31}$$

The FBC correspond to $\nu = \pm\pi/2$ whereas the NBC to $\nu = 0$, but all values of ν ensure a self-adjoint Hamilton operator on the half space. The eigenvalue equation for this operator is solved in Ref. [50] and given by

$$\text{spec H}_\nu = \begin{cases} \mathbb{R}_+ & \text{for} \quad \nu \in [-\pi/2, 0] \\ \mathbb{R}_+ \cup \{\varepsilon = -\frac{1}{2m}\tan^2\nu\} & \text{for} \quad \nu \in (0, \pi/2) \end{cases} \tag{3.32}$$

with the complete ortho-normalized system built up by the $u_E(x)$ functions

$$u_{E>0}(x) \propto \cos(\sqrt{2mE}x)\cos\nu - \frac{\sin(\sqrt{2mE}x)}{\sqrt{2mE}}\sin\nu \tag{3.33}$$

and the bound state solution

$$u_{\varepsilon<0}(x) = \frac{1}{\sqrt{2\tan\nu}}\exp(-\tan\nu x). \tag{3.34}$$

This additional state only vanishes in the regime $-\pi/2 \leq \nu \leq 0$. The spectrum is shown in Fig. 3.3 (a). The two critical points where the bound state disappears are $\nu = \pm\pi/2$ and $\nu = 0$. They correspond to the FBC ($\eta \to \infty$) and the NBC ($\eta = 0$) respectively. We identify the state of the point spectrum as an end state introduced by the presence of the edge. Another way to understand the occurrence of this state is to notice that the surface potentials act like a trapping potential and can hence create localized states. In any one-dimensional attractive potential ($\eta > 0$) there will be a bound state while in a barrier potential ($0 > \eta$) there are no end states allowed.

This analysis shows that boundary potentials can generate edge states indepedent of the

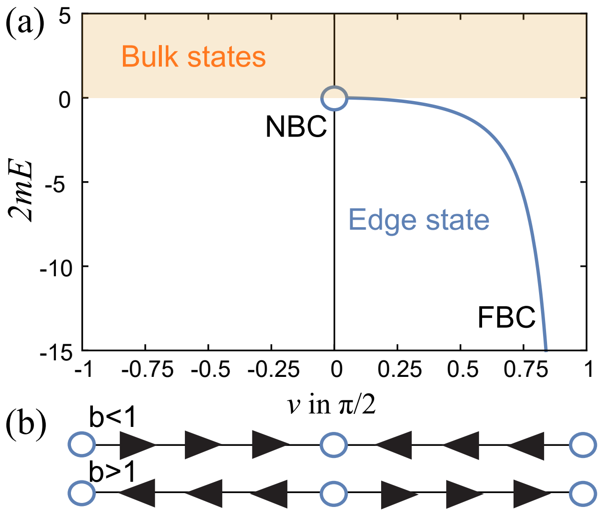

Figure 3.3: The spectrum of a quantum-mechanically free particle living on $[0, \infty)$ with all possible BCs for a self-adjoint Hamiltonian (a) suggests already a renormalization flow (b) towards FBC or NBC depending on the scaling parameter b.

topological properties of the bulk. Since we aim to analyze only the occurrence of edge states which are topological in origin, we will stipulate a *free surface assumption* ($\eta = 0$ or $\eta \to \infty$) and thus consider only NBC and FBC. This assumption and the requirement of ellipticity are thus of primary importance for the analysis of continuum models for TIs.

4 Compact continuum models of TIs

In this and in the following chapter we will study the class of TIs which have been first theoretically predicted: the Chern insulators "invented" by Haldane [57] who has won the Nobel prize in 2016.

Let us start with the simple case of a two-band insulator with broken time-reversal (TR) symmetry. The two bands derive from either a sublattice or an orbital degree of freedom. We can write the corresponding Hamiltonian H using the Pauli matrices σ_i (defined in appendix A) as [58]

$$H = d_0(k_x, k_y)\sigma_0 + \mathbf{d}(k_x, k_y) \cdot \boldsymbol{\sigma}. \tag{4.1}$$

The eigenstates $|\pm\rangle$ with eigenenergies $E = d_0(k_x, k_y) \pm \sqrt{\mathbf{d}(k_x, k_y) \cdot \mathbf{d}(k_x, k_y)}$ can be found using the projectors

$$P_\pm(\mathbf{k} = (k_x, k_y)) = \frac{1}{2}\left(1 \pm \hat{\mathbf{d}}(\mathbf{k}) \cdot \boldsymbol{\sigma}\right), \tag{4.2}$$

where $\hat{\mathbf{d}}$ is the normalized unit vector of $\mathbf{d}$. The related Chern number Eq. 2.54 – the topological invariant – turns out to be for each band

$$\nu_\pm = \mp\frac{1}{4\pi}\int_{\mathcal{M}} dk_x dk_y\ \hat{\mathbf{d}} \cdot (\partial_{k_x}\hat{\mathbf{d}} \times \partial_{k_y}\hat{\mathbf{d}}) \tag{4.3}$$

if $\mathbf{d}(k_x, k_y)$ is non-zero for all $\mathbf{k}$. The manifold $\mathcal{M}$ is the Brillouin zone (BZ) and the vector $\hat{\mathbf{d}}$ lives on a sphere. The vector $\hat{\mathbf{d}}$ therefore implies a mapping from the 2-torus $\mathbb{T}^2$ of the BZ to the 2-sphere $\mathbb{S}^2$, whereas ν counts the number of times the image of the mapping wraps the sphere. It is then obvious that this number is integer and cannot change under smooth deformations due to the fact that the integral over the BZ is simply the *Jacobian* of the mapping $\hat{\mathbf{d}}(k_x, k_y)$.

In low-energy continuum theories the manifold $\mathbb{T}^2$ is substituted by the real plane $\mathbb{R}^2$. Mappings between a two-dimensional real plane and a 2-sphere are topologically trivial. There is, however, one loophole: the basis manifold can be compactified over a *sphere*. The topological invariant counting how many times a sphere is wrapped can be then redefined.

4.1 Chern insulator in the honeycomb lattice

Haldane [57] showed how to create a non-zero Hall conductivity ($\nu_\pm \neq 0$) without using Landau levels in the honeycomb lattice. This was the first example of a two-dimensional TI displaying the so-called *quantum anomalous Hall* (QAH) effect. The model assumes spinless electrons with a next-nearest-neighbor (NNN) hopping of complex hopping amplitude. The unimodular phase factors in the NNN hopping are chosen such that the total magnetic flux is 0 in contrast to the QHE.

It was later understood that this model also describes one spin channel of a model for spin-one-half fermions with intrinsic spin-orbit coupling in graphene [29]. *Graphene* has indeed a honeycomb lattice structure (Fig. 4.1 (a)) with two carbon (C) atoms per unit-cell. A realistic description of graphene implies to treat all orbital and spin-degree of freedom using *ab-inito* calculations. Nevertheless, the low-energy properties can be approximated with a TB Hamiltonian which considers only orbitals orthogonal to the graphene layer (p_z orbitals). The effects of all the other bands are included in an effective hopping parameter between the p_z orbitals [59] (π bonds).

Back to spinless electrons on the honeycomb lattice, we start by writing the two primitive lattice vectors

$$\mathbf{a}_1 = \{3, +\sqrt{3}\}/2 \text{ and } \mathbf{a}_2 = \{3, -\sqrt{3}\}/2, \tag{4.4}$$

where we set the bond length equal to 1. The reciprocal lattice can be described by the reciprocal lattice vectors

$$\mathbf{b}_1 = 2\pi\{1, +\sqrt{3}\}/3 \text{ and } \mathbf{b}_2 = 2\pi\{1, -\sqrt{3}\}/3 \tag{4.5}$$

satisfying $\mathbf{a}_i \cdot \mathbf{b}_j = 2\pi\delta_{ij}$ and defining the BZ shown in Fig. 4.1 (b). A TB Hamiltonian with nearest-neighbor hopping results in a $\mathbf{d}$ vector given by

$$d_0 = d_3 = 0 \text{ and } d_1 - id_2 = -t(e^{i\mathbf{k}\cdot\boldsymbol{\delta}_1} + e^{i\mathbf{k}\cdot\boldsymbol{\delta}_2} + e^{i\mathbf{k}\cdot\boldsymbol{\delta}_3}), \tag{4.6}$$

where $\boldsymbol{\delta}_i$ are the three vectors describing the nearest neighbors. Alternatively a gauge transformation leads to a modified $\tilde{\mathbf{d}}$ vector

$$\tilde{d}_0 = \tilde{d}_3 = 0 \text{ and } \tilde{d}_1 - i\tilde{d}_2 = e^{-i\mathbf{k}\cdot\boldsymbol{\delta}_i}(d_1 - id_2) \tag{4.7}$$

satisfying $\tilde{d}_i(\mathbf{k}) = \tilde{d}_i(\mathbf{k} + \mathbf{b}_j)$. Therefore the Hamiltonian has the *Bloch* form after this transformation.

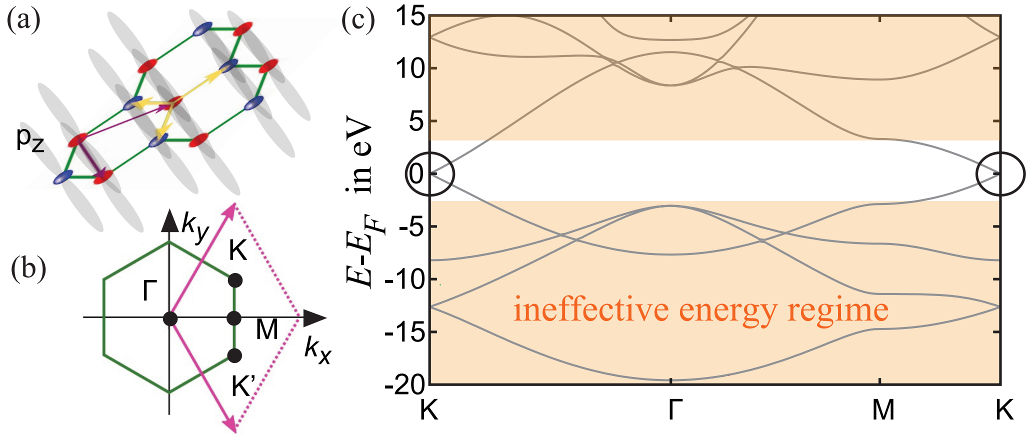

Figure 4.1: The honeycomb lattice (a) and its corresponding BZ (b). The panel (c) shows the result of a TB Hamiltonian considering only s and p orbitals given by Ref. [59]. The p_x and p_y orbitals are in-plane while p_z is out-of-plane. The orange part is irrelevant for the low-energy physics.

This model, which only takes into account the *nearest-neighbor* hopping, has *Dirac nodes* at the Fermi level protected by *inversion* and TR symmetry. The position of these nodal points is fixed by the lattice symmetry C_6 [60], and corresponds to two valleys

$$\mathbf{K} = \frac{2\pi}{3}\left\{1, +\frac{1}{\sqrt{3}}\right\} \text{ and } \mathbf{K}' = \frac{2\pi}{3}\left\{1, -\frac{1}{\sqrt{3}}\right\} \cong -\mathbf{K}. \tag{4.8}$$

Close to these points the bands have a conical dispersion, the so-called Dirac cones, characteristic of a linear band crossing point (LBCP). The presence of these crossings is illustrated in Fig. 4.1 (c) using a realistic TB model with additional orbitals.

The effective continuum theory close to the Dirac nodes is the *massless* Dirac equation. Haldane imagined now a flux pattern with complex NNN hopping to open up a gap. We reiterate that for spin-one-half fermions this effect is generated in each spin channel by the effective spin-orbit coupling coming from the overlap of the p_z orbitals with the d-orbitals [59] which can be treated using *quasi*-degenerate perturbation theory (*Löwdin partitioning*) [61].

The effective low-energy Hamiltonian of the two valleys is

$$H^{(1)}(\pm\mathbf{K} + \delta\mathbf{k}) = -t(\pm\sigma_x\delta k_x + \sigma_y\delta k_y) \pm B_z\sigma_z, \tag{4.9}$$

where B_z is a valley-dependent mass [62] breaking TR symmetry and originating precisely from the magnetic flux pattern introduced by Haldane. We can write the effective model

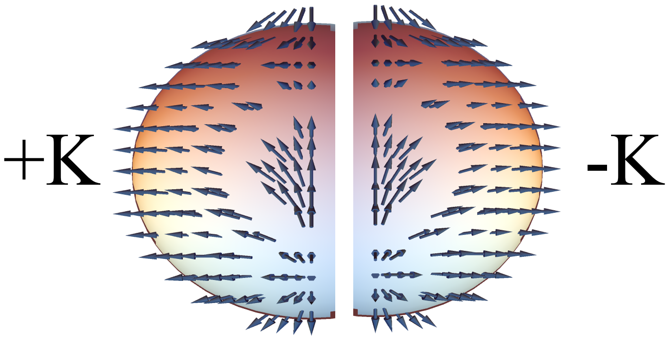

Figure 4.2: Schematic gluing of the two planes representing the valley Hamiltonians to build up a sphere.

with $H_{\mathbf{K}} \equiv H^{(1)}(+\mathbf{K}+\delta\mathbf{k})$ in the block form

$$\mathcal{H} = \begin{pmatrix} H_{+\mathbf{K}} & 0 \\ 0 & H_{-\mathbf{K}} \end{pmatrix}, \tag{4.10}$$

where the symmetry [60] of the full Hamiltonian connects $H_{-\mathbf{K}} = H_{\mathbf{K}}(\delta k_x, -\delta k_y; -B_z)$. We want to remark that this is not the only way to get an effective Hamiltonian for a Chern insulator in a hexagonal lattice. An alternative approach is discussed in Ref. [63]. The presence of two valleys together with the low-energy continuum approximation divides the compact basis manifold $\mathbb{T}_2$ (BZ) of the underlying lattice system in two disconnected spaces represented by two real planes $\mathbb{R}^2 \oplus \mathbb{R}^2$ which do not hybridize with each other. The Chern numbers describing the two valleys are given by $\nu_{\mathbf{K},\mathbf{K}'} = \mathrm{sign}(B_z)/2$ showing that each valley is *topologically marginal* [64]. However, the full Chern number, given by the sum of both valley Chern numbers, is $\nu = \mathrm{sign}(B_z)$. This is in agreement with the lattice results. The presence of two valleys removes the topological marginality. To understand this, one can compare the *Berry curvatures* of both valleys

$$\Omega_{+\mathbf{K}}(\mathbf{k}) = \Omega_{-\mathbf{K}}(\mathbf{k}) = \frac{1}{2}\frac{B_z t}{\sqrt{B_z^2 + t^2\mathbf{k}^2}}, \tag{4.11}$$

which, fulfilling the condition: $\lim_{\mathbf{k}\to\infty} \Omega_{+\mathbf{K}}(\mathbf{k}) = \lim_{\mathbf{k}\to\infty} \Omega_{-\mathbf{K}}(-\mathbf{k})$, allows to glue the two planes into a sphere (illustrated in Fig. 4.2).

Let us now analyze the occurrence of edge states. As long as the NNN hoppings are purely imaginary, the lattice Hamiltonian respects particle-hole symmetry, and thus the system belongs to the symmetry class D of the AZ classification. We are now ready to analyze the presence of edge states. Two possibilities can be taken into account: the analysis of the effective theory on a half-line $[0, \infty)$, or in a ribbon of width W. We want to start with the first one.

First we make a unitary transformation to simplify the analysis. This transformation has two parts given by a cyclic permutation of all elements of the vector $\mathbf{d} = (d_x, d_y, d_z)$ to $\tilde{\mathbf{d}} = (d_y, d_z, d_x)$, and

$$U = \begin{pmatrix} \tau_0 & 0 \\ 0 & \tau_y \end{pmatrix}. \tag{4.12}$$

This leads to a *valley-isotropic* representation where k_x appears only in the diagonal elements. The transformed Hamiltonian is then of the form $\mathcal{H}' = \sigma_0 \otimes \tilde{H}_{\mathbf{K}}$. With this, the unitary part of the particle-hole symmetry operator $P' = \sigma_x \otimes \sigma_0$. We look now for edge states of this model in the half plane determined by $x > 0$. The most general boundary conditions can be written in the form [65, 66]

$$\mathbf{\Psi}(0) = \zeta M \mathbf{\Psi}(0) \text{ with } M = M^\dagger \text{ and } M^2 = 1, \tag{4.13}$$

where the spinor wavefunction $\mathbf{\Psi}(x) = \{\Psi_1^+(x), \Psi_2^+(x), \Psi_1^-(x), \Psi_2^-(x)\}^T$ solves the eigenvalue problem of $\mathcal{H}'(\mathbf{k})$ for $x > 0$ ($\zeta = +1$) and $x < 0$ ($\zeta = -1$). Together with the required absence of the current normal to the boundary, which is equivalent to the anti-commutator

$$\left\{ \frac{\partial \mathcal{H}'}{\partial k_x}, M \right\} = 0, \tag{4.14}$$

we have to ensure particle-hole symmetry. The boundary conditions (BCs) have to fulfill $P'_{eff} \mathbf{\Psi}^*(0) = M P'_{eff} \mathbf{\Psi}^*(0)$, which leads to the commutation relation

$$[\mathcal{P}, M] = 0 \text{ with } \mathcal{P} = P' \mathcal{K}. \tag{4.15}$$

With these additional restrictions we find that the parametric form of the matrix M can be distinguished in two different classes, reading

$$M_a = \begin{pmatrix} 0 & 0 & 0 & e^{i\phi} \\ 0 & 0 & e^{i\phi} & 0 \\ 0 & e^{-i\phi} & 0 & 0 \\ e^{-i\phi} & 0 & 0 & 0 \end{pmatrix} \text{ and } M_b = \begin{pmatrix} 0 & e^{+i\phi} & 0 & 0 \\ e^{-i\phi} & 0 & 0 & 0 \\ 0 & 0 & 0 & e^{-i\phi} \\ 0 & 0 & e^{+i\phi} & 0 \end{pmatrix}. \tag{4.16}$$

The first type of BCs M_a admixes the two valleys and contains evanescent waves of the form

$$\boldsymbol{\Psi}_a \propto \begin{pmatrix} e^{i\phi} \\ -\text{sign}(B_z t)\zeta e^{i\phi} \\ -\text{sign}(B_z t) \\ \zeta \end{pmatrix} e^{\lambda|x|} \tag{4.17}$$

with a linear dispersion $E = \zeta\text{sign}(B_z)|t|k_y$ and $\lambda = -|B_z/t|$. In this case we see that the non-trivial value of the Chern number goes hand in hand with the presence of linear-dispersing edge states connecting the valence and the conduction band. The coupling of the valleys by the boundary lead to a good bulk-edge correspondence.
For the second type of BCs M_b, which do not couple the valleys, one finds that the edge spectrum of the half-plane configuration can contain the evanescent solutions

$$\boldsymbol{\Psi}_b^+ \propto \begin{pmatrix} \zeta \\ e^{-i\phi} \\ 0 \\ 0 \end{pmatrix} e^{\lambda_+|x|} \text{ and } \boldsymbol{\Psi}_b^- \propto \begin{pmatrix} 0 \\ 0 \\ \zeta \\ e^{+i\phi} \end{pmatrix} e^{\lambda_-|x|} \tag{4.18}$$

with the energies $E_\pm = \zeta(\mp B_z \sin\phi - t\cos\phi k_y)$, if the evanescent tails fulfill $\lambda_\pm = \mp\sin\phi k_y + \cos\phi B_z/t < 0$ for the half-plane $x > 0$ or $x < 0$ respectively. Considering now only the effective Hamiltonian of $+\mathbf{K}$ in the half-space $x > 0$, we further find a critical value k_y^{crit} where the edge solution appears ($\sin\phi > 0$) or disappears ($\sin\phi < 0$) out of the bulk states. The critical point is given by

$$k_y^{crit} = B_z/(t\tan\phi) \text{ and } E^{crit} = -B_z/\sin\phi \tag{4.19}$$

describing the point where the edge states are connected to the valence ($E^{crit} > 0$) or conduction band ($E^{crit} < 0$) respectively. This leads to a *spectral asymmetry* in each valley $\pm\mathbf{K}$ which is coupled to its valley Chern number $\nu_{\mathbf{K}} = \nu_{-\mathbf{K}}$. By counting the number of appearing edge states coming out of the bulk of the valence band $N_{VB}^{\pm}$ and adding the number of disappearing edge states connected to the conduction band $N_{CB}^{\pm}$ one gets twice the valley Chern number:

$$\nu_{\mathbf{K}} = (N_{VB}^{\pm} + N_{CB}^{\pm})/2, \tag{4.20}$$

which is precisely the full Chern number. If we would consider the half space $x < 0$ the sign of $N_{CB/VB}^{\pm}$ has to be flipped (see appendix B). This is a bulk-edge correspondence between

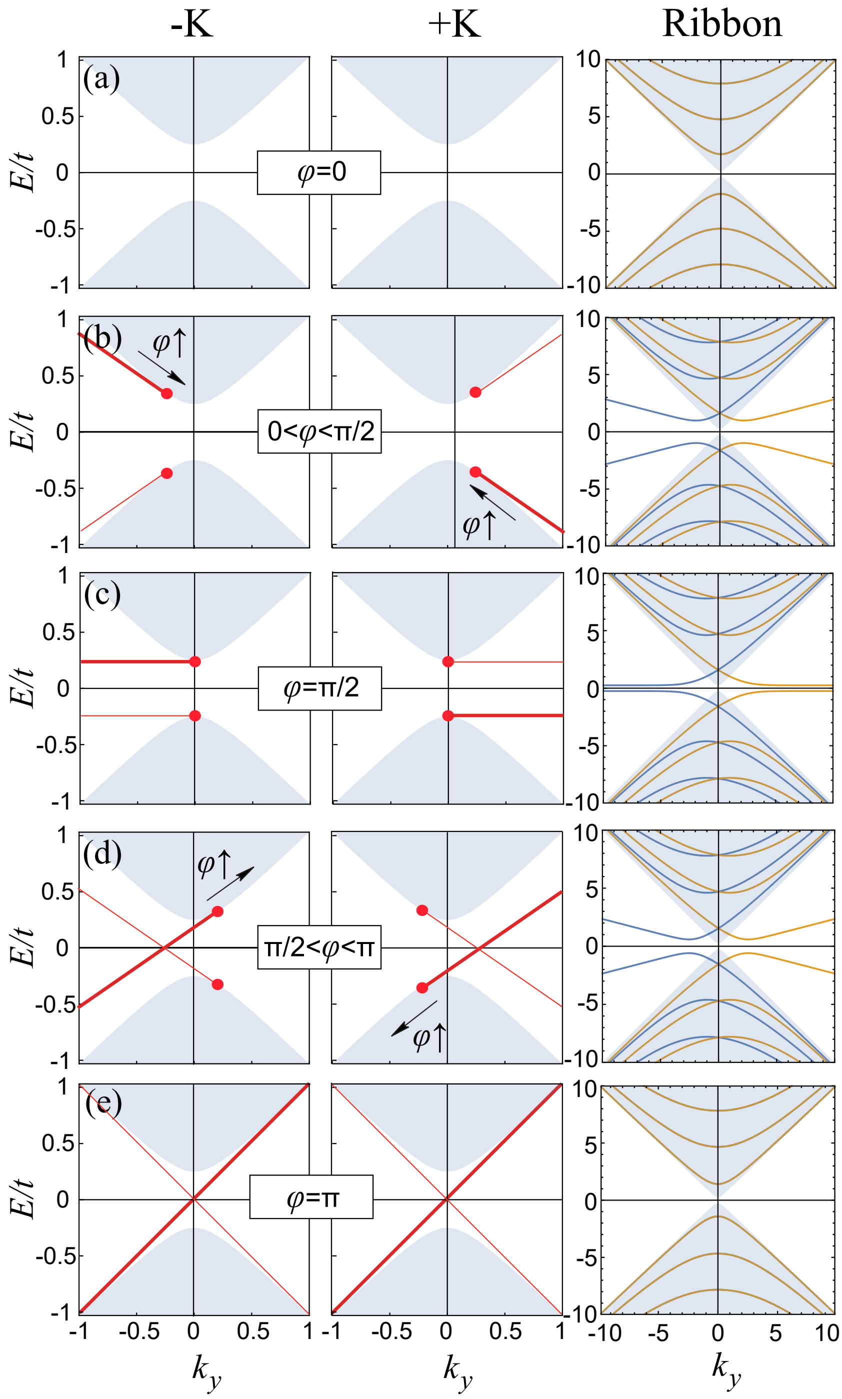

Figure 4.3: Edge spectrum of the honeycomb lattice in the phase $\nu_- = 1$ for $B_z/t = +1/4$ ($t > 0$) for each valley and in a ribbon of width $W = 1$. For other system widths the plot is invariant under the rescaling: $k_y(W) = Wk_y$, $E(W) = WE$, $\lambda(W) = W\lambda$ and $B_z(W) = WB_z$. The blue region marks the bulk regime and the dark red lines are the edge states. The thick lines correspond to the edge $x > 0$ and the thin lines to $x < 0$. The red dots describe the critical points (k^{crit}, E^{crit}) where the edge states appear or disappear.

the valley invariants and the valley edge spectrum. The edge spectrum is illustrated in Fig. 4.3 (b)-(d) together with the ribbon results, where the edge solutions of two edges can hybridize with each other. It must be emphasized that the bulk-edge correspondence for the appearance of in-gap modes only holds for $\pi/2 < \phi < \pi$ in a semi-infinite space.

There are two cases which show a completely different behavior. If $\sin\phi = 0$ and $\cos\phi B_z/t < 0$ we get a solution connecting the valence and the conduction band at $\pm\infty$ respectively. The other exceptional case is if $\sin\phi = 0$ and $\cos\phi B_z/t > 0$ where we find no edge states at all, although the valley Chern number is non-trivial. These types of spectra are illustrated in Fig. 4.3 (a) and (e). The first case could be related to a $\nu = 0$ Chern number while the second one to $\nu = 2$.

This partial breakdown of the bulk-edge correspondence has been dubbed as *marginal bulk-edge correspondence* and it has been related to the topological marginality of the single-valley Hamiltonians. However, and as a spoiler for the next chapter, it must be stressed that the generic BC for the single-valley Dirac Hamiltonians explicitly accounts for a finite edge potential, which violates the free surface assumption we stipulated in Chapter 3.

4.2 Bilayer graphene with Bernal stacking

The marginal bulk-edge correspondence is generic for graphene-like systems [67]. In this paragraph we want to construct a related two-valley model relevant for bilayer graphene (BLG) [68]. To describe spinless electrons in two honeycomb layers we need a 8×8 Hamiltonian to respect the sublattice degree of freedom A/B, the valley degree of freedom $\pm\mathbf{K}$ and the layer-index $1/2$. The two honeycomb lattices are arranged in the *Bernal stacking* configuration (see Fig. 4.4).

The distance between the two layers is not fixed and encrypted in the matrix elements of the inter-layer hopping. The symmetries of this system are equal to the one of graphene. Similar to a single honeycomb layer there are two non-equivalent degeneracy points $\pm\mathbf{K}$. Close to them we can consider now a low-energy expansion up to the first order. Following Ref. [69] each valley block can be written as

$$H_{\pm\mathbf{K}} = \begin{pmatrix} \Delta_\perp\sigma_x \pm \sigma_z B_z & K_{\pm\mathbf{K}} \\ K^\dagger_{\pm\mathbf{K}} & \mp\sigma_z B_z \end{pmatrix} \tag{4.21}$$

in the basis $\{\psi_{B,1}, \psi_{B,2}, \psi_{A,1}, \psi_{A,2}\}$, where $K_{\pm\mathbf{K}} = -t(\pm\sigma_x k_x + k_y\sigma_y)$ are the single-layer Hamiltonians, $\Delta_\perp$ is the effective interlayer dimerization parameter and B_z is a valley-

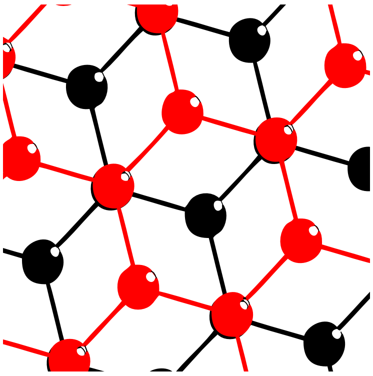

Figure 4.4: Top view of the graphite bilayer in the Bernal stacking configuration.

dependent mass. The parameter B_z drives the system from a semimetal to an insulator. This Hamiltonian is marginal like the Dirac equation.

If we assume again that the relevant physics is related to low-energy excitations, we can reduce the model for each valley to a two-band model. We write the *time-independent* Schrödinger equation as $(H_{\pm\mathbf{K}} - E)\Psi = 0$ with $\Psi = \{\xi, \phi\}$. This equation is equivalent to

$$\xi = -\frac{1}{\Delta_\perp^2 - E^2 + B_z^2}(E\mathbb{1} + \Delta_\perp \sigma_x \pm \sigma_z B_z) K_{\pm\mathbf{K}} \phi \tag{4.22}$$

giving a relation between the spinors ξ and ϕ. We can then write the eigenvalue equation for the spinor ϕ as

$$\begin{aligned}(\Delta_\perp^2 - E^2 + B_z^2)(E\mathbb{1} \pm \sigma_z B_z)\phi =& - K_{\pm\mathbf{K}}(E\mathbb{1} + \Delta_\perp \sigma_x \pm \sigma_z B_z) K_{\pm\mathbf{K}}\phi \\ =&(-t^2(E\mathbb{1} \mp \sigma_z B_z)k^2 + \Delta_\perp^2 \tilde{H}_{\pm\mathbf{K}})\phi,\end{aligned} \tag{4.23}$$

where we introduced the effective low-energy Hamiltonian

$$\tilde{H}_{\pm\mathbf{K}} = -\frac{t^2}{\Delta_\perp}\begin{pmatrix} 0 & (k_x \mp i k_y)^2 \\ (k_x \pm i k_y)^2 & 0 \end{pmatrix}. \tag{4.24}$$

In the regime, $E, B_z \ll \Delta_\perp$ the eigenvalue equation for the effective wavefunction ϕ can be finally written as

$$[\tilde{H}_{\pm\mathbf{K}} \mp \sigma_z B_z]\phi = E\phi. \tag{4.25}$$

The marginal property of the original four-component model is inherited by the reduced two-band model. We do not want to go into details, because the analysis of the edge states was already done in Ref. [69]. The authors studied the correspondence between the nontrivial topological properties associated with the individual valleys of gapped BLG and the presence of gapless modes at its edges. The important result is that, similar to the honeycomb lattice mode, one finds different behaviors depending on the lattice termination. The *non-universality* of the bulk-edge correspondence is attributed to the absence of a well-defined topological invariant in the single-valley Hamiltonians of BLG, in analogy to the honeycomb lattice.

4.3 One-point compacification

The already anticipated idea of obtaining a spherical basis manifold from a real plane, goes back to the method of *stereographic projection* (illustrated in Fig. 4.5) in two dimensions. It is a mapping of all points of a sphere onto points in the plane and the other way around. This mapping is well-defined on the full sphere, except for one point: the north pole (N). The south pole (S) is mapped on itself.

For all other points this mapping is *smooth* and *bijective*. Therefore we can write the stereographic projection

$$(\varrho, \alpha) = (\cot(\phi/2), \theta), \tag{4.26}$$

where we express the plane $(k_x, k_y) = \varrho(\cos\alpha, \sin\alpha)$ in polar coordinates and the unit sphere by the *zenith* angle ϕ and the *azimuth* θ. Nevertheless we will be more interested in defining the *inverse* operation

$$(\phi, \theta) = (2\arctan(1/\varrho), \alpha), \tag{4.27}$$

which allows to compactify the plane $\mathcal{M} = \mathbb{R}^2$. The north pole of the sphere $(\phi = 0, \theta)$ corresponds then to all points at $\varrho \to \infty$.

Interestingly, this line is *not* an element of the plane $\mathbb{R}^2$, but we can add it artificially. This is possible only if all points become indistinguishable at infinity. Fields living on those manifolds need the necessary property that at infinity they are independent on the angle α. For a quantum-mechanical eigenstate this implies that its projector $P(\mathbf{k})$ has to fulfill

$$\lim_{|\mathbf{k}|\to\infty} P(\mathbf{k}) = f(|\mathbf{k}|), \tag{4.28}$$

where f is a functional form of the projector, which is independent of the direction of the vector $\mathbf{k}$. This requirement can be generalized to higher dimensions d to ensure a compact basis manifold $\mathbb{S}^d \simeq \mathbb{R}^d \cup \{\infty\}$. This is the so-called *one-point compactification* [10, 70].

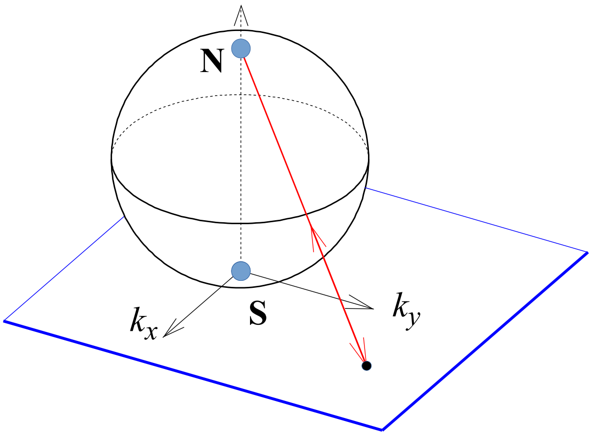

Figure 4.5: Illustration of the stereografic projection where each point of the sphere is mapped on a point of the plane. The north pole is mapped on the ∞-line of the plane.

Assuming a Hamiltonian which has for large $\mathbf{k}$ the form

$$H(\mathbf{k}) = ... + \sum_{|\{\alpha\}|=n} h_\alpha k^{\{\alpha\}} \text{ with } k^{\{\alpha\}} = k^{\alpha_1} k^{\alpha_2} ... k^{\alpha_n}, \tag{4.29}$$

where α is multi-index describing the products of n elements of the set $\{k_1, k_2 ... k_d\}$, we can reformulate the condition of one-point compactification for all eigenstates to the condition

$$\lim_{\mathbf{k}\to\infty} \frac{H(\mathbf{k})}{|\mathbf{k}|^n} = h(\theta_1, ..., \theta_{d-1}) \text{ with } P_n h(\theta_1, ..., \theta_{d-1}) P_n = E_n(\theta_1, ..., \theta_{d-1}), \tag{4.30}$$

where the projectors P_n with energy E_n do not dependent on the spherical coordinates $\{\theta_i\}$ and the order of the bands stays unchanged for an arbitrary set of angles. We have to remark that the order between all conduction (or valence) bands can change with $\{\theta_i\}$ instead.

If a general Hamiltonian does not fulfill this condition, it is in principle allowed to add a correction term $H_{corr}(\mathbf{k})$ *ad hoc* to $H(\mathbf{k})$, with $H_{corr}(\mathbf{k})$ respecting all the underlying symmetries and dominating at large $\mathbf{k}$. In the framework of effective theories such corrections have two effects: the eigenvalues and eigenvectors are modified at high energies, and the basis manifold changes. Topological invariants however are directly coupled to the concrete eigenvectors, and thus such corrections do not only change the manifold, but also the value of the invariant. It is therefore absolutely necessary to fix the order of the $\mathbf{k} \cdot \mathbf{p}$ expansion in line with the predictions of a lattice model.

4.4 The BHZ model

We next apply the idea of compact low-energy theories for TIs to a particle-hole symmetric Chern insulator by studying a simple two-band model known as the *Bernevig-Hughes-Zhang* (BHZ) model [71]. The model is defined by

$$\mathbf{d}_\mu(\Gamma + (k_x, k_y)) \simeq \{Ak_x, \mu A k_y, M - B(k_x^2 + k_y^2)\}, \tag{4.31}$$

where μ is an additional spin degree of freedom. We assume a sufficient small parameter M ($|M/B| < 4$) and finite parameters A, B. The corresponding lattice Hamiltonian is given by

$$\mathbf{d}_\mu(k_x, k_y) = \{A \sin k_x, \mu A \sin k_y, M - 2B(2 - \cos k_x - \cos k_y)\} \tag{4.32}$$

defined over the BZ $(-\pi, \pi] \times (-\pi, \pi]$. Expanding at the Γ-point restores the continuum model.

Let us study the continuum model at Γ in more details. The projector of the two bands is characterized by $\hat{\mathbf{d}}(\mathbf{k}) = -\mathrm{sign}(B)$ at $\mathbf{k} \to \infty$ showing that models of this form are indeed *one-point compactified.* The first things we can check are the Chern numbers. In the lattice and in the continuum model the invariants are equal and given by $\nu_\pm = \mp\mu(\mathrm{sign}(M) + \mathrm{sign}(B))$. The effective theory captures the topological invariant accurately. For $M, B > 0$ (or $M, B < 0$) the normalized $\mathbf{d}$ vector visits both the south and the north pole and wraps the unit sphere once. In the opposite regime $M > 0 > B$ (or $M < 0 < B$), the image of the mapping does not cover the full sphere. The Chern number is 0. The fact that the long-wavelength Hamiltonian is capable of correctly identifying the topology of the band structure of the lattice Hamiltonian, motivates to analyze the occurrence of topologically protected edge states on a half space ignoring finite size effects [72]. We want to remark that the Hamiltonian in each spin channel belongs to the AZ class D which allows a $\mathbb{Z}$ topological invariant. The particle-hole symmetry

$$\sigma_x H^T(-\mathbf{k}) = -H(-\mathbf{k})\sigma_x \tag{4.33}$$

is the only generic symmetry in this system. After the substitution $k_x \to -i\partial_x$ we can analyze the secular equation $\det(H(-i\lambda, k_y) - E) = 0$ for the energy E with the help of the exponential ansatz $\Psi \to \psi_0(\lambda)e^{\lambda x}$ on the half plane $x > 0$ to find the topologically protected edge states.

One can start to analyze the secular equation. This leads to a real polynomial of degree

2 in λ^2 which allows maximally two λ values with $\Re\lambda < 0$ for the half-space $x > 0$. We denote them as: λ_1 and λ_2. Any general polynomial of degree n has n complex roots by the *fundamental theorem of algebra.* It is therefore helpful to express the secular equation with the *Vieta's formulas* which relate the coefficients of the secular polynomial with its roots. They are given by

$$\lambda_1^2 + \lambda_2^2 = 2k_y^2 + \frac{A^2 - 2BM}{B^2} \text{ and } \lambda_1^2\lambda_2^2 = \frac{A^2k_y^2 + (M - Bk_y^2)^2 - E^2}{B^2}. \tag{4.34}$$

The corresponding wave functions to this secular equation can be expressed as

$$\psi_0^{(1)}(\lambda) = \begin{pmatrix} -iA(\lambda + \mu k_y) \\ E - M + B(k_y^2 - \lambda^2) \end{pmatrix} \text{ or } \psi_0^{(2)}(\lambda) = \begin{pmatrix} E + M + B(k_y^2 - \lambda^2) \\ -iA(\lambda - \mu k_y) \end{pmatrix}. \tag{4.35}$$

The vectors $\psi_0^{(1)}$ and $\psi_0^{(2)}$ are two different representations of the same secular equation. The general edge solution must therefore be of the form

$$\begin{aligned} \Psi(x) &= a_1^{(1)}\psi_0^{(1)}(\lambda_1)e^{\lambda_1 x} + a_2^{(1)}\psi_0^{(1)}(\lambda_2)e^{\lambda_2 x} \text{ or} \\ \Psi(x) &= a_1^{(2)}\psi_0^{(2)}(\lambda_1)e^{\lambda_1 x} + a_2^{(2)}\psi_0^{(2)}(\lambda_2)e^{\lambda_2 x} \end{aligned} \tag{4.36}$$

representing the *superposition* of the two eigenvectors where $a_j^{(i)}$ are still unknown coefficients. The next step is to implement the BCs. We stick to the free surface assumption we defined in Chapter 3, and thus consider both natural boundary conditions (NBC), and fixed boundary conditions (FBC). These two BCs then imply the existence of a localized normalizable in-gap state

$$\Psi \propto \begin{pmatrix} i \\ -\text{sign}(AB) \end{pmatrix} \left(e^{\lambda_1 x} \mp e^{\lambda_2 x}\right) \tag{4.37}$$

with an energy dispersion directly connected to the Chern number ν_-

$$E(k_y) = \mu \, \text{sign}(B)|A|k_y = \nu_-|A|k_y. \tag{4.38}$$

The exponents characterizing the decay length of the edge states are found to be

$$\lambda_{1/2} = \frac{\Sigma}{2} \pm \sqrt{\frac{\Sigma^2}{4} - \Pi} = -\frac{1}{2}\frac{|A|}{|B|} \pm \sqrt{k_y^2 + \frac{A^2 - 4BM}{4B^2}}. \tag{4.39}$$

The spectrum contains one chiral localized edge mode for all $k_y^2 < M/B$. At $k_y^2 = M/B$

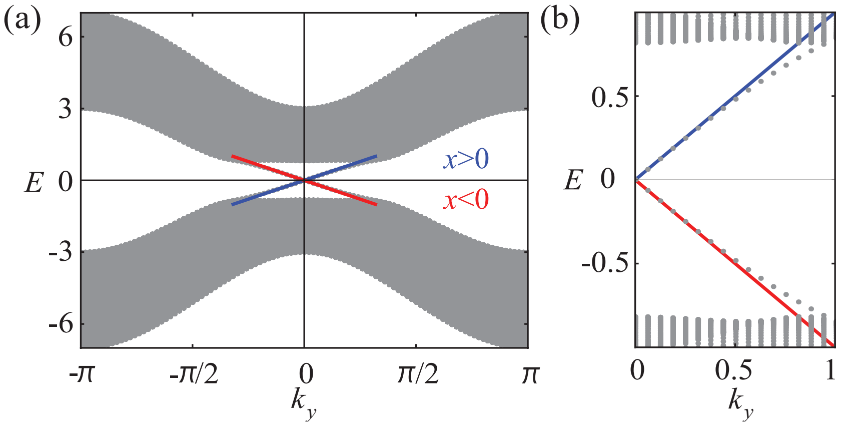

Figure 4.6: (a) Projective bands for the TB model with $M = A = B = 1$ in a ribbon of width $W = 200a$ with the square lattice constant $a = 1$. The thick lines represent the analytical results for the dispersion of the topologically protected edge states as obtained from the low-energy expansion at Γ in a semi-infinite strip with $x < 0$ (red) and $x > 0$ (blue). (b) Enlargement in the bulk gap region showing a perfect agreement between the analytical and the numerical results.

the edge states go into the bulk and disappear.

For comparison with the lattice results we study the TB model defined above. The dispersion of the topological edge states is shown in Fig. 4.6 with thick lines. The numerical results obtained by solving the square lattice TB Hamiltonian in a ribbon geometry show an excellent agreement with the long wavelength theory analysis. This proves that the absence of a short-distance cutoff in the long-wavelength Hamiltonian does not change neither the topological invariant nor the edge states.

This can be further corroborated by comparing the electronic properties of the topologically protected zero modes, which are encountered at the projection of the $\mathbf{k} \cdot \mathbf{p}$ expansion point in the one-dimensional BZ. The zero modes can be characterized by the *decay length* l_c which is defined as

$$l_c^{-1} = \max(\{\Re|\lambda_i|\}) \tag{4.40}$$

and the *Fermi velocity* v_F describing the linear dispersion at zero energy

$$E(k_y) = v_F k_y + \mathcal{O}(k_y^2). \tag{4.41}$$

They are plotted for one set of parameters in Fig. 4.7. The parameter M describes the bulk band gap which influences the behavior of the Fermi velocity and the decay length. Both the lattice model Hamiltonian and the continuum Hamiltonian predict the Fermi velocity

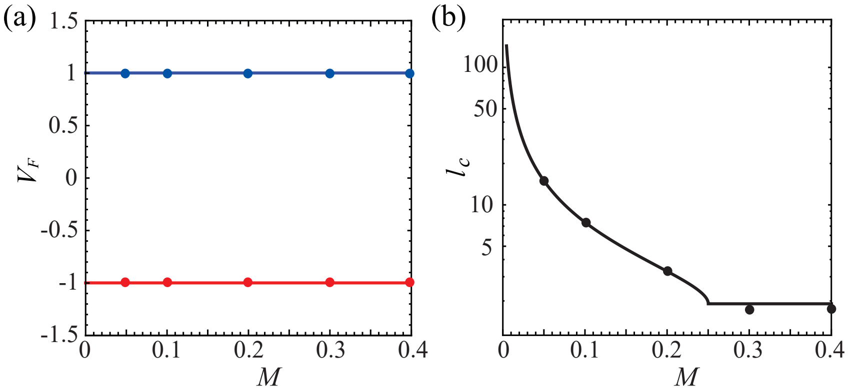

Figure 4.7: (a) Fermi velocity of the topologically protected zero modes as a function of the band gap M for the BHZ model with $A = B = 1$. (b) Same for the decay length of the zero modes in the bulk. In both panels, the continuous lines correspond to the functional dependence obtained from the $\mathbf{k}\cdot\mathbf{p}$ analysis, while the points are the results of the TB model for sufficient large ribbon width.

of the zero modes to be independent of the gap parameter while the decay length decreases by increasing M, thereby showing that the zero modes become effectively more localized as the band gap is increased. Qualitatively and quantitatively both models show the same electronic characteristics. The effective theory is therefore capable of correctly identifying all aspects of the topology of the band structure of the underlying lattice Hamiltonian.

4.5 Insulator with Chern number 2

To corroborate that a one-point compactified $\mathbf{k}\cdot\mathbf{p}$ model generally captures the topological properties of the underlying lattice model, we here consider a model which realizes a topological phase with Chern number $|\nu_\pm| = 2$. A single-valley effective model with a possible realization of this topological invariant is given by the generic form

$$\mathbf{d} = \{k_x^2 - k_y^2, 2k_xk_y, M - B(k_x^4 + k_y^4)\}, \tag{4.42}$$

and belongs to the AZ class C with the particle-hole symmetry operator $P = \sigma_y$. The fundamental difference with respect to the BHZ model is that a model in symmetry class C only allows even Chern numbers ($2\mathbb{Z}$). The corresponding lattice Hamiltonian can be constructed on a square lattice by applying the substitution

$$k_i \to \sin k_i + \frac{1}{6}\sin^3 k_i, k_i^2 \to 2(1-\cos k_i) + \frac{1}{3}(1-\cos k_i)^2 \text{ and } k_i^4 \to 4(1-\cos k_i)^2 \tag{4.43}$$

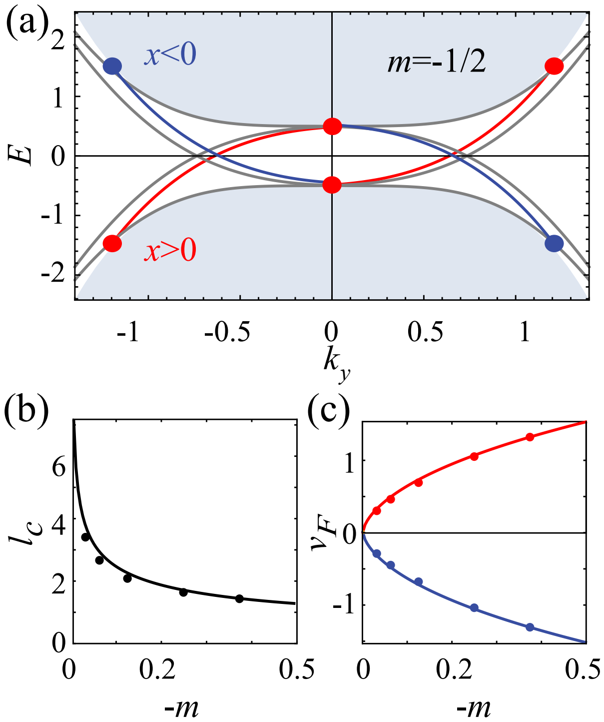

Figure 4.8: (a) The edge and bulk spectrum for a ribbon in x-direction with the parameters $M = B = 1/2$ is shown. The gray lines are the corresponding TB results of the band edges and the topological surface states for large enough system size. The blue region marks the bulk states of the effective model. The colored dots indicate the critical points where edge states appear or disappear. The decay length and Fermi velocity of the zero modes are plotted in (b) and (c) for $B = 1/2$ considering only the right branch of the edge states ($k_y > 0$). The dots are the TB results and the lines represent the continuum model solutions.

to the effective low-energy model.

We find that the topological invariant in the low-energy theory is well-defined and can be calculated to be $\nu_\pm = \mp(\text{sign}(M) + \text{sign}(B))$, which is for finite M and finite B equal to the lattice result. The mass parameter $M = 0$ separates a topologically trivial from a non-trivial phase. In the non-trivial phase, the vector $\hat{\mathbf{d}}$ wraps the sphere twice, which is consistent with the *even* Chern number listed in the periodic table of TIs.

Let us now analyze the occurrence of topologically protected edge states. The bulk-edge correspondence demands that for a Chern number equal to ν_- we should find ν_- topologically protected chiral edge solutions with the sign of ν_- defining their *chirality*, *i.e.*

$$\sum_i \text{sign}(v_F^{(i)}) = \nu_-. \tag{4.44}$$

Here $v_F^{(i)}$ are the Fermi velocities of the ν_- edge states. For $\nu_- = 2$ this means we must encounter two chiral edge states connecting the valence and the conduction band.

We solve the low-energy model in the half-plane $x > 0$ and the use of the substitution $k_x \to -i\partial_x$ together with the *self-adjoint* free-surface BCs

$$\mathbf{\Psi}(x = 0) = 0 \text{ and } \mathbf{\Psi}'(x = 0) = 0. \tag{4.45}$$

This leads to the edge spectrum plotted in Fig. 4.8 (a). We find a nice agreement with the spectrum obtained using the TB Hamiltonian in a ribbon geometry.

This holds true also by looking at the presence of the zero modes. It is interesting to notice that the zero modes do not occur at the low-energy expansion point. The edge spectrum contains two *branches* appearing at the bottom (top) of the conduction (valence) bulk bands precisely at the low-energy expansion point. Away from it, the two edge branches bend down and up respectively, and eventually touch the valence and conduction bands. Moreover, the electronic characteristics of zero modes as predicted by the continuum theory, and shown in Fig. 4.8 (b) and (c), are in perfect agreement with the TB results.

4.6 Time-reversal invariant systems

We finally comment on the possibility to define a topological invariant in a one-point compactified low-energy theory also in the case of time-reversal (TR) invariant systems. One simple model is the one-point compactified *Dirac* equation [73] where one exchanges the mass term M by the momentum dependent mass $M - B\hat{\mathbf{p}}^2$ discussed in Ref. [74]. This modified Dirac equation is invariant under TR symmetry, particle-hole symmetry and chiral symmetry (AZ class DIII), and can be therefore classified according to a $\mathbb{Z}_2$ invariant in $d = 2$ and to a $\mathbb{Z}$ index in $d = 3$.

The compact Hamiltonian can be written as

$$\mathcal{H}_{Dirac} = A\boldsymbol{\alpha} \cdot \hat{\mathbf{p}} + (M - B\hat{\mathbf{p}}^2)\beta, \tag{4.46}$$

where the matrices $\alpha_{x,y,z}$ and β have to fulfill $\alpha_i^2 = \beta^2 = \mathbb{1}_{4\times4}$ and $\{\alpha_i, \alpha_j\} = \{\alpha_i, \beta\} = 0$ if $i \neq j$. One common representation is

$$\alpha_i = \sigma_x \otimes \sigma_i \text{ and } \beta = \sigma_z \otimes \mathbb{1}_{2\times2}. \tag{4.47}$$

This equation has four bulk solutions which can be expressed in the form

$$\Psi_{\mu,\pm}(\mathbf{p}) = u_{\mu,\pm} e^{i(\mathbf{p}\cdot\mathbf{r}\mp E(\mathbf{p},)t)} \text{ and } u_{\mu,\pm} = \sqrt{\frac{E_p \pm (M - Bp^2)}{2E_p}} \begin{pmatrix} \chi_\mu \\ \frac{A\boldsymbol{\sigma}\cdot\mathbf{p}}{(M-Bp^2)\pm E_p}\chi_\mu \end{pmatrix} \tag{4.48}$$

with $\chi_1 = \{1, 0\}$, $\chi_2 = \{0, 1\}$ and the positive energy $E(p) = \sqrt{A^2p^2 + (M - Bp^2)^2}$. The index μ is used to distinguish the two solutions for each energy $\pm E(p)$. The bulk gap is then between the valence bands $(1, +), (2, +)$ and the conduction bands $(1, -), (2, -)$.
To analyze the topological invariant we have to define the TR operation. The symmetry operator is given by $\mathcal{T} = -i\alpha_x\alpha_z\mathcal{K}$ with $\mathcal{T}^2 = -1$ where $\mathcal{K}$ is the complex conjugation, so that we can analyze the overlap matrix

$$\Omega_{\mu\nu} = \langle u_{\mu,-}(\mathbf{p})|\mathcal{T}|u_{\nu,-}(\mathbf{p})\rangle = \begin{pmatrix} 0 & +i\frac{M-Bp^2}{-E(p)} \\ -i\frac{M-Bp^2}{-E(p)} & 0 \end{pmatrix}_{\mu\nu}. \tag{4.49}$$

In two-dimensions we can define an invariant by counting the *zeros* of the *Pfaffian* in the overlap matrix

$$P(\mathbf{p}) = \mathrm{Pf}\,[\Omega] = i\frac{M - Bp^2}{-E(p)} \tag{4.50}$$

as we already pointed out in Eq. 2.76. The only thing we have to change is to substitute the manifold encircled by the contour $\mathcal{C}$. This manifold is no longer the half torus but the half plane as illustrated in Fig. 4.9. In the context of the one-point compactification this means that we use a half sphere and the contour integral is over the *half circle* [75]. The arc closing at ∞ gives no contribution, so that the contour integral becomes a line integral from $p_x = -\infty$ to $+\infty$. This invariant can be evaluated and shows that the non-trivial phase is characterized by $\mathrm{sign}(M) = \mathrm{sign}(B)$ as we expected from the character switch of the eigenvectors from Γ to ∞. This is the $\mathbb{Z}_2$ invariant for the effective theory in $d = 2$.
For a modified Dirac equation in three-dimensions instead, the topological invariant can be written as [74]

$$N = \frac{\varepsilon_{ijk}}{48\pi^2}\mathrm{Tr}\left[C\int_{\mathcal{V}} d^3p G\partial_{p_i}G^{-1}G\partial_{p_j}G^{-1}G\partial_{p_k}G^{-1}\right] = \frac{1}{2}(\mathrm{sign}(M) + \mathrm{sign}(B)), \tag{4.51}$$

where $C = \sigma_y \otimes \sigma_0$ is the chiral-symmetry operator, $\mathcal{V} = \mathbb{R}^3 \cup \{\infty\}$ is the one-point

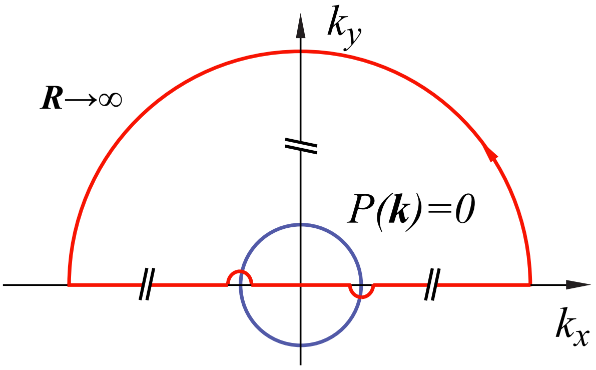

Figure 4.9: To count the number of pairs of the zeros of the Pfaffian $P(\mathbf{k})$ building a ring $M = Bp^2$ shown as a blue ring we integrate over the (red) contour $\mathcal{C}$.

compactified 3-dimensional space and $G(= G(0, \mathbf{p}))$ is the *Green function* given by

$$G(i\omega, \mathbf{p}) = -\frac{A\boldsymbol{\alpha}\cdot\mathbf{p} + (M - Bp^2)\beta + i\omega}{\omega^2 + H^2(p)}. \tag{4.52}$$

5 Non-local effective theory

In the previous chapters we have shown that $\mathbf{k}\cdot\mathbf{p}$ Hamiltonians have a well-defined topological invariant if the target and basic manifold is a full sphere. For two-valley systems, however, the single-valley Hamiltonians display a marginal bulk-edge correspondence, which has been suggested to come about the topological marginality of the single-valley effective theories. In this chapter, we will study a single-valley marginal Hamiltonians, which does not display a marginal bulk-edge correspondence as long as we respect the free-surface assumptions we stipulated in Chapter 3. This, in the end, allows us to relate the phenomenon of marginal bulk-edge correspondence to the effect of specific boundary potentials in the low-energy theory. To demonstrate this, we will start with a two-band model displaying a single degeneracy point, and corresponding to a *quadratic band crossing point* (QBCP). This is a point in the Brillouin zone (BZ) where two bands cross and have a quadratic dispersion close to it. It can be for instance realized in the *checkerboard lattice* (C_4 symmetry), and in the *Kagome lattice* (C_6 symmetry) [76].

5.1 Quadratic band crossing point

A QBCP protected by time-reversal (TR) symmetry and C_4 or C_6 rotational symmetry carries a *quantized Berry flux*

$$W = \frac{1}{i}\int_{\gamma} d\mathbf{k}\cdot \langle \Psi(\mathbf{k})|\nabla_{\mathbf{k}}|\Psi(\mathbf{k})\rangle\,, \tag{5.1}$$

where γ is a contour in the momentum space enclosing the band crossing point and $|\Psi(\mathbf{k}+\mathbf{G})\rangle = |\Psi(\mathbf{k})\rangle$ is the Bloch wave function of one band involved in the band crossing. The difference between a linear band crossing point (LBCP) and a QBCP is that the fluxes are $|W| = \pi$ and $|W| = 2\pi$ respectively [77]. It is important to stress that a generic QBCP can carry a 0 Berry flux, in which case the QBCP is an accidental crossing and not protected by any point-group symmetry.

Let us start constructing an effective model for such a system. Ignoring the identity part

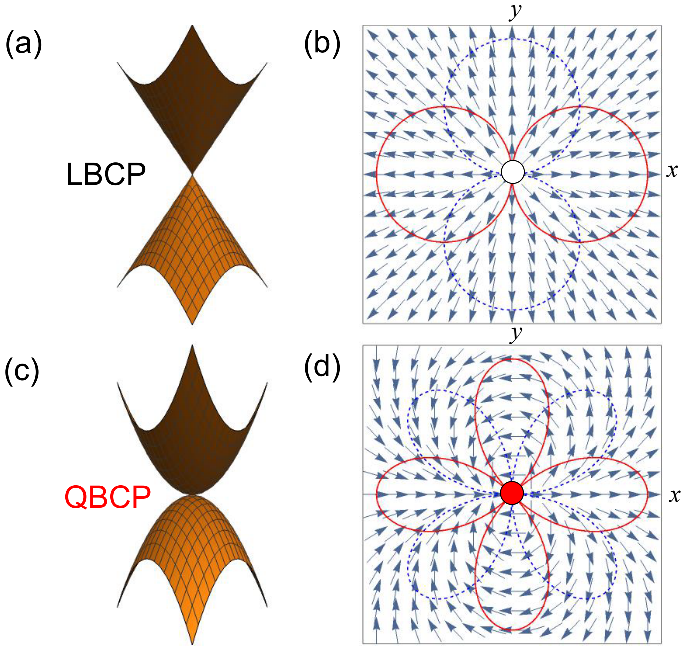

Figure 5.1: The band degeneracy points and their dispersion for a linear (LBCP) and a quadratic (QBCP) symmetry-protected band crossing point are plotted in (a) and (c) respectively. The non-trivial *meron configurations* $\mathbf{h}/|\mathbf{h}|$ which correspond to them are shown in (b) and (c). The red (solid) lines represent the absolute value of the x-component and the blue (dashed) the y-component.

the most general model with quadratic dispersion is given by

$$\mathcal{H}(k_x, k_y) = A_x(\boldsymbol{\sigma} \cdot \mathbf{n}_x)k_x^2 + A_y(\boldsymbol{\sigma} \cdot \mathbf{n}_y)k_y^2 + 2A_{xy}\sigma_x k_x k_y, \tag{5.2}$$

with the two unit vectors $\mathbf{n}_{x,y}$ and parameters A_x, A_y and A_{xy}. The direction of the A_{xy}-term is fixed along x without loss of generality. Applying TR symmetry represented by a complex conjugation $\mathcal{K}$

$$\mathcal{K}\mathcal{H}(k_x, k_y) = \mathcal{H}(-k_x, -k_y)\mathcal{K}, \tag{5.3}$$

one finds that the direction vectors have to fulfill $\mathbf{e}_y \cdot \mathbf{n}_{x,y} = 0$. To stabilize and protect the QBCP against perturbations one establishes, e.g., a *fourfold* symmetry axis C_4 in the Hamiltonian

$$R_y\mathcal{H}(k_x, k_y) = \mathcal{H}(R_y(k_x, k_y))R_y \text{ and } R_y\left(\theta = \frac{\pi}{2}\right) = \begin{pmatrix} \cos\theta & \sin\theta \\ -\sin\theta & \cos\theta \end{pmatrix}. \tag{5.4}$$

This leads to the additional condition $A_x = A_y$ and $\mathbf{n}_x = -\mathbf{n}_y$. A sixfold rotation C_6 is clearly more restrictive. Let us study a model where we set $\mathbf{n}_x = (0,0,1)$ without loss of generality. The Hamiltonian can be written as

$$\mathcal{H}(k_x,k_y) = h_1\sigma_x + h_2\sigma_z, \text{ where } \mathbf{h} = (h_1,h_2) = (2A_{xy}k_xk_y, A(k_x^2-k_y^2)) \tag{5.5}$$

describes a two-dimensional vector, where its length has the physical meaning of half of the band gap. This allows us to compare the QBCP with the LBCP. The dispersion close to the QBCP is plotted in Fig. 5.1(c) in comparison to a conventional Dirac cone (a). The $\mathbf{h}$ vector is a planar vector with a vortex structure illustrated in Fig. 5.1(d) again differing from a symmetry-protected LBC (b) with a generic $\mathbf{h} = (A_xk_x, A_yk_y)$. Another difference is that the QBCP has *d-wave* symmetry in contrast to a Dirac Point which has *p-wave* symmetry.

5.2 QBCP in the checkerboard lattice

The simplest two-band model displaying a QBCP is a TB model for spinless fermions on a *checkerboard lattice.* Its two-atomic basis $\{A,B\}$ is described by the basis vector $\mathbf{d} = (\mathbf{e}_x + \mathbf{e}_y)/2$ and the *primitive lattice vectors* are given by $\mathbf{a}_1 = \mathbf{e}_x$ and $\mathbf{a}_2 = \mathbf{e}_y$. Introducing an edge parallel to the x or y axis leads to a lattice termination with only one type of sublattice atoms, which we denote as (OO). Terminating the lattice along the diagonal direction, both types of sublattice atoms are alternating at the edge. We denote this termination as (OX). The two lattice descriptions are presented in Fig. 5.2.
The corresponding Hamiltonians can be written explicitly

$$\mathcal{H} = \sum_{\mathbf{R}_i,\mathbf{R}_j} \begin{pmatrix} c_{\mathbf{R}_i,A} \\ c_{\mathbf{R}_i,B} \end{pmatrix}^\dagger \begin{pmatrix} +\Delta_{\mathbf{R}_i,\mathbf{R}_j} + Q_1\delta_{\mathbf{R}_i,\mathbf{R}_j} & H^{AB}_{\mathbf{R}_i,\mathbf{R}_j} \\ \cdot & -\Delta_{\mathbf{R}_i,\mathbf{R}_j} - Q_1\delta_{\mathbf{R}_i,\mathbf{R}_j} \end{pmatrix} \begin{pmatrix} c_{\mathbf{R}_j,A} \\ c_{\mathbf{R}_j,B} \end{pmatrix} \tag{5.6}$$

with the blocks

$$\begin{aligned} \frac{\Delta_{\mathbf{R}_i,\mathbf{R}_j}}{-t_2} =& \delta_{\mathbf{R}_i,(x_j-1,y_j)} - \delta_{\mathbf{R}_i,(x_j,y_j+1)} + h.c. \text{ and} \\ \frac{H^{AB}_{\mathbf{R}_i,\mathbf{R}_j}}{-t} =& e^{+i\phi}(\delta_{\mathbf{R}_i,\mathbf{R}_j} + \delta_{\mathbf{R}_i,(x_j+1,y_j+1)}) + e^{-i\phi}(\delta_{\mathbf{R}_i,(x_j,y_j+1)} + \delta_{\mathbf{R}_i,(x_j+1,y_j)}), \end{aligned} \tag{5.7}$$

where $\mathbf{R}_i = (x_i,y_i)$ represents the lattice coordinates. In the Hamiltonian above, t is the nearest-neighbor hopping, t_2 a next-nearest neighbor hopping with opposite sign in the two sub-lattices A/B.

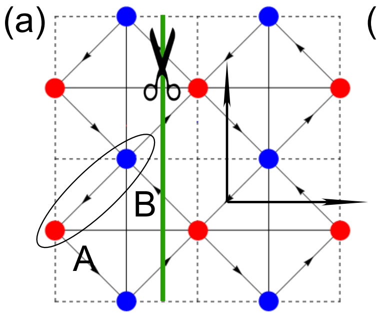

Figure 5.2: The figures show the two important descriptions for the Bravais lattice of the checkerboard. The different choices can be used for different terminations. (a) is the (OO) termination and (b) the (OX) termination. The green lines describe the edge. The red/blue dots are elements of the sub-lattice A/B with an alternating potential $V = \pm Q_1$. Thick lines with arrows correspond to hopping terms $-te^{i\phi}$, dashed lines to $+t_2$ and thick lines without arrows to $-t_2$.

Since the QBCP is protected by TR and point group symmetry, the model exhibits a gap only by explicitly breaking TR. This can be done by adding a magnetic flux of zero average, realizing the *Quantum anomalous Hall phase* (QAH) [76, 77]. The flux pattern is shown in Fig. 5.2 and is characterized by the parameter ϕ.

Besides TR symmetry breaking perturbation, rotational symmetry breaking perturbations realize a splitting of the QBCP into two LBCPs. This can be modeled by introducing a staggered chemical potential $\pm Q_1$ in the two sub-lattices A/B.

The discrete translation symmetry in the Bravais lattice allows us to consider the model with TR as well as rotational symmetry breaking perturbations in momentum space. The Fourier transformation is given by

$$c_{\mathbf{r}_i,A} = \frac{1}{\sqrt{N}} \sum_{\mathbf{k}} e^{i\mathbf{k}\mathbf{r}_i} c_{\mathbf{k},A} \text{ and } c_{\mathbf{r}_i,B} = \frac{1}{\sqrt{N}} \sum_{\mathbf{k}} e^{i\mathbf{k}(\mathbf{r}_i+\mathbf{d})} c_{\mathbf{k},B}, \tag{5.8}$$

where $\mathbf{k} = k_x \mathbf{e}_x + k_y \mathbf{e}_y, (k_x, k_y) \in (-\pi, \pi] \times (-\pi, \pi]$. In Fourier space, we can write the Hamiltonian as

$$\mathcal{H} = \sum_{\mathbf{k}\in BZ} c^{\dagger}_{\mathbf{k},\alpha} H_{\alpha\beta}(\mathbf{k}) c_{\mathbf{k},\beta}. \tag{5.9}$$

By definition the set of particle operators is not periodic ($c_{\mathbf{k}+\mathbf{G},A} = c_{\mathbf{k},A}$ and $c_{\mathbf{k}+\mathbf{G},B} = e^{-i\mathbf{G}\mathbf{d}} c_{\mathbf{k},B}$), and thus also the Hamiltonian is not periodic in $\mathbf{G}$. We dub this as the *natural gauge*. It is convenient to introduce another set of fermionic operators respecting instead the Bloch condition. We denote this choice as the *Bloch gauge*, ensuring that the related

Hamiltonian $\tilde{H}$ is periodic. The Bloch Hamiltonian is given by

$$\tilde{H}(\mathbf{k}) = U(\mathbf{k})H(\mathbf{k})U^{\dagger}(\mathbf{k}) \text{ with } U(\mathbf{k}) = \begin{pmatrix} e^{-i\mathbf{kd}/2} & 0 \\ 0 & e^{+i\mathbf{kd}/2} \end{pmatrix} \tag{5.10}$$

and the corresponding operators are defined by $\tilde{c}_{\mathbf{k},A} = c_{\mathbf{k},A}$ and $\tilde{c}_{\mathbf{k},B} = e^{i\mathbf{kd}}c_{\mathbf{k},B}$. Nevertheless, both gauge choices are topologically equivalent (cf. paragraph 2.5). The Hamiltonians can be characterized with the vector

$$\mathbf{d} = \begin{pmatrix} -4t\cos\left(\frac{k_x}{2}\right)\cos\left(\frac{k_y}{2}\right)\cos(\phi) \\ -4t\sin\left(\frac{k_x}{2}\right)\sin\left(\frac{k_y}{2}\right)\sin(\phi) \\ Q_1 - 2t_2(\cos k_x - \cos k_y) \end{pmatrix} \tag{5.11}$$

in the natural gauge, whereas in the Bloch gauge we have

$$\tilde{\mathbf{d}} = \begin{pmatrix} -t(\cos(k_x+\phi) + \cos(k_y+\phi) + \cos\phi + \cos(k_x+k_y-\phi)) \\ -t(\sin(k_x+\phi) + \sin(k_y+\phi) - \sin\phi + \sin(k_x+k_y-\phi)) \\ Q_1 - 2t_2(\cos k_x - \cos k_y) \end{pmatrix}. \tag{5.12}$$

This description is in line with Ref. [78]. An analysis of this model shows the checkerboard lattice indeed realizes a QBCP if the symmetry-breaking terms are set to $\phi, Q_1 = 0$. The term Q_1 splits the QBCP into two Dirac cones for small parameters $|\eta| < 1$ with $\eta = Q_1/4t_2$ and $\phi = 0$. The two Dirac points are located at

$$\mathbf{K}_{\pm}^{\eta>0} = \{\pm\arccos(2|\eta|-1), \pi\} \text{ and } \mathbf{K}_{\pm}^{\eta<0} = \{\pi, \pm\arccos(2|\eta|-1)\}. \tag{5.13}$$

Let us make an expansion around these two Dirac points. Using the Bloch gauge we find that the two Dirac cones carry the same Berry flux adding to 2π as expected. The expansion for $\eta > 0$ indeed reads

$$\tilde{\mathbf{d}}_{\mathbf{K}_\pm} \simeq \begin{pmatrix} \mp 2t\sqrt{\eta(1-\eta)}k_y \\ 2t\eta k_y \\ \pm 4t_2\sqrt{\eta(1-\eta)}k_x \end{pmatrix} = \begin{pmatrix} \cos\alpha & \mp\sin\alpha & 0 \\ \pm\sin\alpha & \cos\alpha & 0 \\ 0 & 0 & 1 \end{pmatrix} \begin{pmatrix} \pm 2t\sqrt{\eta}k_y \\ 0 \\ \pm 4t_2\sqrt{\eta(1-\eta)}k_x \end{pmatrix}. \tag{5.14}$$

Using the natural gauge instead the two π Berry fluxes of the Dirac cones cancel each other $W = W_{\mathbf{K}_+} + W_{\mathbf{K}_-} = 0$. This can be immediately proven by considering the expansion

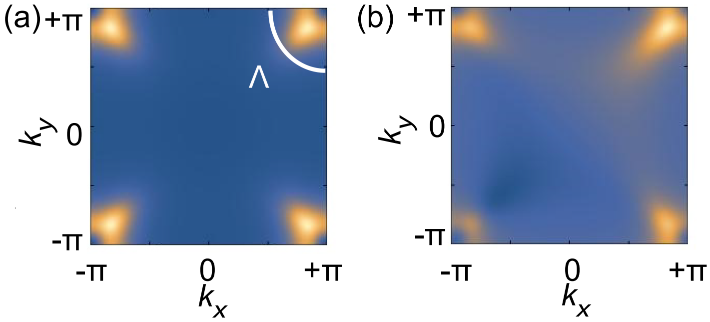

Figure 5.3: Density plot of the Berry curvature $\Omega/(2\pi)$ in the QAH phase of the checkerboard lattice considering the natural gauge (a) and the Bloch gauge (b) in arbitrary units. The TB parameters have been chosen as $Q_1 = 0$, $t_2/t = 0.9$ and $\phi = 0.1$. White regions correspond to high density and blue to zero density.

around the two Dirac points can be written as

$$\mathbf{d}_{\mathbf{K}_\pm} \simeq \begin{pmatrix} 2t\sqrt{\eta}k_y \\ 0 \\ \pm 4t_2\sqrt{\eta(1-\eta)}k_x \end{pmatrix} \text{ for } \eta > 0. \tag{5.15}$$

The signs in the first component of $\mathbf{d}_{\mathbf{K}_\pm}$ are equal, contrary to expansion found in the Bloch gauge. Nevertheless, the expansion around M for $Q_1 = 0$ up to the second order gives a $W = 2\pi$ Berry flux independent of the gauge description. The fact that in the natural gauge the Berry flux is not conserved under rotational-symmetry breaking perturbations already implies that for the analysis of the topological properties, the Bloch gauge should be always taken into account.

Let us now assume $\phi \neq 0$. The QAH phase is realized for $\phi \neq n\pi/2$ and $|\eta| < 1$. Using the formula (4.3) we can calculate the Chern number for the lattice model and get

$$\nu_- = -\text{sign}(t_2 \sin(2\phi)) \begin{cases} 1 & |\eta| < 1, \phi \neq n\pi/2 \\ 0 & |\eta| > 1, \phi \neq n\pi/2 \end{cases} \tag{5.16}$$

independent of the gauge. It is important to stress that in the two gauges the Berry curvature Ω is, for $|\phi| \ll 1$, always localized close to the M point of the BZ, *i.e.* where the QBCP occurs in the absence of TR symmetry breaking perturbations. They are shown for one set of parameters in Fig. 5.3. This fact suggests that a low-energy expansion around this point should correctly capture the topological properties of the system.

Before discussing this low-energy model let us discuss the symmetries of the TB Hamiltonian and first consider the natural gauge. In the absence of TR symmetry breaking

perturbations, *i.e.* $\phi = 0$, the Hamiltonian possesses TR symmetry $\mathcal{T} = \mathcal{K}$ where $\mathcal{K}$ is the complex conjugation. In addition, since the Hamiltonian anticommutes with σ_y for $\phi = 0$, we also find a chiral symmetry $\mathcal{C} = \sigma_y$ and consequently a particle-hole symmetry $\mathcal{P} = \sigma_y \mathcal{K}$, which squares to -1. In the QAH phase, the TR symmetry is broken but the system still possesses particle-hole symmetry. Henceforth, the system should belong to the symmetry class C of the AZ table and characterized by an even integer invariant.
This apparent paradox can be solved by considering that in the Bloch gauge the unitary part of the particle-hole symmetry operator acquires an explicit $\mathbf{k}$-dependence reading

$$\tilde{P}_{\mathbf{k}} = \begin{pmatrix} 0 & -ie^{-i\mathbf{k}\cdot\mathbf{d}} \\ +ie^{+i\mathbf{k}\cdot\mathbf{d}} & 0 \end{pmatrix}. \tag{5.17}$$

Therefore, in the Bloch gauge the system does not possess any symmetry and belongs to the symmetry class A, which correctly allows for a generic integer topological invariant and is in agreement with the calculated Chern number. The fact that the real symmetry class of the checkerboard lattice model is the A class will be important for the foregoing low-energy theory analysis.

5.3 Hemi-spherical Chern insulators

Let us now introduce the effective low-energy model for the checkerboard lattice close to the $M = \{\pi, \pi\}$ point of the BZ in the QAH phase, and further assume $|\phi| \ll 1$ and $Q_1 = 0$. Since in a low-energy theory analysis, we are allowed to take any representation of the $\mathbf{d}$ vector we choose the naural gauge, the expansion of which close to the M point results in

$$\mathbf{d}(M + (k_x, k_y)) \simeq \begin{pmatrix} -t\cos\phi k_x k_y \\ -4t(1 - (k_x^2 + k_y^2)/8)\sin\phi \\ -t_2(k_x^2 - k_y^2) \end{pmatrix}. \tag{5.18}$$

The corresponding Hamiltonian describes up to the second order the correct energy dispersion. To ensure that the Berry curvature is localized directly at M we have to treat ϕ as an infinitesimally small parameter. We find

$$\mathbf{d}(d\phi, k_x, k_y) = \begin{pmatrix} -tk_x k_y \\ -4td\phi \\ -t_2(k_x^2 - k_y^2) \end{pmatrix} + \mathcal{O}_3(k_x, k_y, d\phi). \tag{5.19}$$

With this, the Chern number of the continuum theory calculated with Eq. (4.3) is equal to the one of the lattice model. The reason why this is the case is not so simple as in the BHZ model. The continuum model is not one-point compactified since the *projector* of the lowest band is not constant at ∞. The checkerboard lattice continuum model is therefore a *marginal* theory as defined in the previous chapter, and the calculated Chern number does not represent a topological invariant. In addition, there isn't any valley degree of freedom.

We could then first start to *compactify* the model in such a way that the TR symmetry breaking mass is modified as $M \to M - Bk^n$ where $n \in 2\mathbb{Z}_+$. By substituting $d\phi \to d\phi(1-k^4)$ we find that the Chern number is given by $\nu_- = -2\text{sign}(t_2 d\phi)$. This number is even and twice as large as the lattice result. This follows from the fact that the continuum low-energy model inherits a particle-hole symmetry squaring to -1 and thus the model belongs to the symmetry class C of the AZ table. Every model with a compact basis manifold belonging to this class has to display an even topological invariant. However, the symmetry class of the checkerboard lattice model in the QAH phase is the class A. This symmetry consideration forbids us a one-point compactification.

Let us now give the relation between the Chern number and a topological invariant.

For the low-energy continuum theory of the checkerboard lattice model, the normalized $\hat{\mathbf{d}}$ vector is not constant at ∞, but it is still planar, *i.e.*

$$\mathbf{n} \cdot \mathbf{d}(|\mathbf{k}| \to \infty) = 0, \tag{5.20}$$

where $\mathbf{n}$ is the unit vector normal to the plane. In addition for $\mathbf{k} \to 0$ the normalized $\hat{\mathbf{d}}$ vector points normal to this plane. This allows us to reinterpret our manifold as a *hemisphere* where the points at infinity describe the *equator* of it. Using *Stockes' theorem* we can rewrite the Chern number as

$$\nu_- = \frac{1}{2\pi} \int_{\mathbb{R}^2} d^2k\, \Omega(\mathbf{k}) = \frac{1}{2\pi} \oint_{\partial(\mathbb{R}^2)} d\mathbf{k} \cdot \mathbf{A}(\mathbf{k}), \tag{5.21}$$

where $\partial(\mathbb{R}^2)$ is a closed loop in momentum space, $\Omega(\mathbf{k}) = \nabla \times \mathbf{A}(\mathbf{k})$, and $\mathbf{A}(\mathbf{k}) = \langle u(\mathbf{k})|(-i\nabla)|u(\mathbf{k})\rangle$ with $|u(\mathbf{k})$ the wave function of the lower band eigenstate. In addition we fix the gauge of the wave functions in such a way that the eigenstates at the equator are able to contract into the north of south pole of the hemisphere. This then

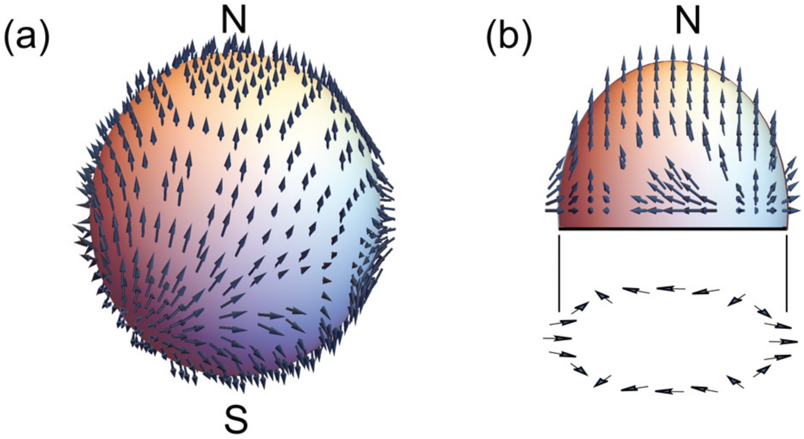

Figure 5.4: Patterns of the $\hat{d}$ vector configurations on a sphere like in the BHZ model (a) and a hemisphere like in the checkerboard lattice (b). The two topological classes are defined in terms of different topological invariants.

implies that the eigenstates for $|\mathbf{k}| \to \infty$ can be written as

$$|\hat{d}_z > 0\rangle = \frac{1}{2}\begin{pmatrix} 1 \\ -(\hat{d}_x + i\hat{d}_y) \end{pmatrix} \text{ and } |\hat{d}_z < 0\rangle = \frac{1}{2}\begin{pmatrix} -\hat{d}_x + i\hat{d}_y \\ 1 \end{pmatrix}. \tag{5.22}$$

With this, we can express the Chern number as

$$\nu_- = \frac{1}{2}\text{sign}(\hat{d}_z)W \text{ with } W = \frac{1}{2\pi}\oint_{\partial(\mathbb{R}^2)} d\mathbf{k}\cdot(\hat{d}_x\nabla\hat{d}_y - \hat{d}_y\nabla\hat{d}_x). \tag{5.23}$$

The Chern number is therefore directly related to another topological invariant, which is precisely the topological charge of the vortex structure realized at $|\mathbf{k}| \to \infty$. For the honeycomb lattice model discussed in the previous chapter, this relation does not hold since W only determines a "valley" Hall conductivity.

In conclusion, the topological origin of the Chern invariant changes from a mapping $[\mathbb{S}_2, \mathbb{S}_2]$, as found in the previous chapter, to a mapping $[\mathbb{S}_1, \mathbb{S}_1]$ as illustrated in Fig. 5.4. This suggests us to identify two different topological classes for single-valley $\mathbf{k}\cdot\mathbf{p}$ Hamiltonians of Chern insulators. In the first class we have a momentum manifold which can be one-point compactified to a Riemannian sphere, and allows for the usual definition of the Chern invariant. In the second one, instead, the momentum manifold is holomorphic to a non-compact hemisphere but still allows for a one-dimensional topological invariant contained in a mapping from a circle to a circle.

5.4 Edge states in the gapped QBCP

We next analyze whether the intrinsic non-compact nature of the low-energy theory for a QBCP leads to a marginal bulk-edge correspondence. We write the $\mathbf{k}\cdot\mathbf{p}$- Hamiltonian as

$$\mathbf{d}(d\phi)/(-t) = \begin{pmatrix} \sin(\theta)\cos(\theta)(k_\perp^2 - k_{||}^2) + \cos(2\theta)k_\perp k_{||} \\ 4d\phi \\ (t_2/t)(\cos(2\theta)(k_\perp^2 - k_{||}^2) - 2\sin(2\theta)k_\perp k_{||}) \end{pmatrix} \tag{5.24}$$

where we used new coordinates

$$\begin{pmatrix} k_x \\ k_y \end{pmatrix} = \begin{pmatrix} \cos\theta & -\sin\theta \\ +\sin\theta & \cos\theta \end{pmatrix} \begin{pmatrix} k_\perp \\ k_{||} \end{pmatrix} \tag{5.25}$$

to describe all directions in the plane. The direction $k_\perp$ is the *decay direction* and $k_{||}$ characterizes the dispersion (*propagation direction*). By using the substitution $k_\perp \to -i\partial_x$ the Hamiltonian turns into a *second-order* matrix differential equation. The edge states can be analyzed by considering the long-wavelength Hamiltonian over the half-plane $x > 0$ and scanning for localized wave functions exponentially decaying into the bulk. Hereby, we use again the exponential ansatz $e^{\lambda x}$ with $\Re(\lambda) < 0$.

In analogy with the previous chapter, one can write the secular equation for the existence of non-trivial solutions using the *Vieta's formulas*

$$\begin{aligned} \Sigma + \Sigma_2 &= \frac{4ik_{||}(4t_2^2 - t^2)\sin(4\theta)}{4t_2^2 + t^2 + (4t_2^2 - t^2)\cos(4\theta)}, \\ \Pi + \Pi_2 + \Sigma\Sigma_2 &= 6k_{||}^2 - \frac{8k_{||}^2(4t_2^2 + t^2)}{4t_2^2 + t^2 + (4t_2^2 - t^2)\cos(4\theta)}, \\ \Sigma\Pi_2 + \Sigma_2\Pi &= k_{||}^2(\Sigma + \Sigma_2) \text{ and} \\ \Pi\Pi_2 &= k_{||}^4 - \frac{8(E^2 - 16t^2d^2\phi)}{4t_2^2 + t^2 + (4t_2^2 - t^2)\cos(4\theta)}, \end{aligned} \tag{5.26}$$

where $\Sigma = \lambda_1 + \lambda_2$, $\Sigma_2 = \lambda_3 + \lambda_4$, $\Pi = \lambda_1\lambda_2$ and $\Pi_2 = \lambda_3\lambda_4$ with the four solutions of the secular equation $\{\lambda_1, \lambda_2, \lambda_3, \lambda_4\}$. The eigenvectors to the eigenvalue E are given by

$$\begin{aligned} \Psi_1(\lambda) &= \begin{pmatrix} -it(4d\phi + k_{||}^2\lambda\cos(2\theta)) - t(k_{||}^2 + \lambda^2)\sin\theta\cos\theta \\ -E + t_2(k_{||}^2 + \lambda^2)\cos(2\theta) - 2it_2k_{||}\lambda\sin(2\theta) \end{pmatrix} \text{ or} \\ \Psi_2(\lambda) &= \begin{pmatrix} iE + it_2(k_{||}^2 + \lambda^2)\cos(2\theta) + 2t_2k_{||}\lambda\sin(2\theta) \\ 4td\phi - tk_{||}^2\lambda\cos(2\theta) + it(k_{||}^2 + \lambda^2)\sin\theta\cos\theta \end{pmatrix}. \end{aligned} \tag{5.27}$$

They are two different representations for the same problem. The most general solution is then given by a superposition of all four solutions, although only two solutions will contribute. We write

$$\Psi_E = \sum_{i=1}^{2} a_i \Psi_1(\lambda_i) e^{\lambda_i x} = \sum_{i=1}^{2} b_i \Psi_2(\lambda_i) e^{\lambda_i x}, \tag{5.28}$$

where the 2 unknown coefficients $\{a_i\}$ or $\{b_i\}$ can be found by using appropriate BCs. We assume a *free surface* so we are tended to choose fixed and natural boundary conditions (FBC and NBC). Applying FBC means in this context $0 = \det(\{\Psi_1(\lambda_1), \Psi_1(\lambda_2)\})$ or $0 = \det(\{\Psi_2(\lambda_1), \Psi_2(\lambda_2)\})$. Both determinants are only linear functions of Π and Σ if we exclude the case $\lambda_1 = \lambda_2$. This allows us to solve Π and Σ in a *linear system* giving

$$\Sigma = \frac{2k_{||}(-E\cos(2\theta) + 2it_2 d\phi \sin(2\theta))}{2t_2 d\phi \cos(2\theta) - iE\sin(2\theta)} \text{ and } \Pi = k_{||}^2. \tag{5.29}$$

With Vieta's third formula one finds that $\Pi_2 = \Pi$. Therefore the fourth formula only allows edge states at the energy $E = \pm 4td\phi$ for $k_{||} \neq 0$. The edge state solutions are *flat* in contrast to the chiral edge states in the BHZ model. By putting the solution in the equation for Σ ensuring $\Re\Sigma < 0$ this leads to the dispersion

$$E_0 = \operatorname{sign}(t_2 k_{||}) 4|t| d\phi = -4|td\phi|\nu_- \operatorname{sign}(k_{||}) \text{ for } k_{||} \neq 0, \tag{5.30}$$

with the normalizable edge state

$$\Psi(x) \propto \begin{pmatrix} i \\ \operatorname{sign}(tt_2 k_{||}) \end{pmatrix} (e^{\lambda_1 x} - e^{\lambda_2 x}) \tag{5.31}$$

and its evanescent tails described by

$$\lambda_{1/2} = \frac{\Sigma}{2} \pm \sqrt{\frac{\Sigma^2}{4} - k_{||}^2} \text{ with } \frac{\Sigma}{k_{||}} = \frac{-4\operatorname{sign}(k_{||})|tt_2| + i(4t_2^2 - t^2)\sin(4\theta)}{t^2\sin^2(2\theta) + 4t_2^2\cos^2(2\theta)}. \tag{5.32}$$

If we instead would use NBC characterized by the equation $j(k_\perp \to -i\partial_x)\Psi|_{x=0} = 0$ with the current operator

$$j = \begin{pmatrix} 2t_2(k_\perp \cos(2\theta) - k_{||}\sin(2\theta)) & t(k_\perp \sin(2\theta) + k_{||}\sin(2\theta)) \\ . & -2t_2(k_\perp \cos(2\theta) - k_{||}\sin(2\theta)) \end{pmatrix}, \tag{5.33}$$

we get the same result except that $\Psi \propto (.)(e^{\lambda_1 x} + e^{\lambda_2 x})$. FBC and NBC realize both the

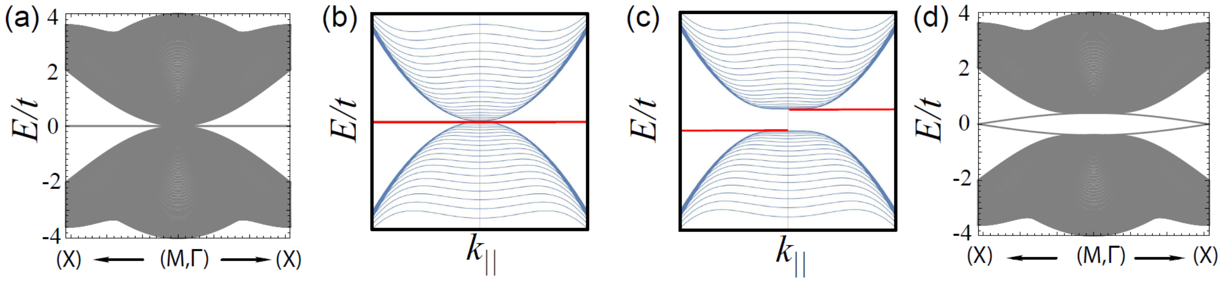

Figure 5.5: Schematic edge dispersion using the effective model without (b) and with (c) a finite value of $d\phi$. They correspond exactly to the ribbon results of the (OX) termination ((a) and (d) respectively) for sufficient large ribbon size N. The parameters for the figures are $\phi = 0.1$, $t_2/t = 0.9$ and $N = 100$. After opening a gap we find topological edge states (red) in the effective picture while a ribbon shows two contributions corresponding to the two edges of the ribbon.

same solution.

A comparison of the region with $k_{||} < 0$ with the region $k_{||} > 0$ show a spectral asymmetry with two branches of edge states, which are disconnected and disappear at $k_{||} = 0$. This is a new type of bulk-edge correspondence predicting that the two branches of edge states have to connect for a momentum different than the low-energy expansion point. This *non-local* behavior of the edge states is a hallmark for this class of Hamiltonians. Its spectrum is illustrated in Fig. 5.5 for zero and finite parameter $d\phi$, and perfectly mimics the ribbon results.

Due to the rotational invariance of the edge spectrum of the effective theory in the natural gauge we can compare directly our effective results with the TB results. As we see, we find edge states precisely at the top (bottom) of the conduction band close to the projection of the low-energy M in the one-dimensional BZ, which is in perfect agreement with the foregoing $\mathbf{k} \cdot \mathbf{p}$ analysis.

The Fermi velocity of the edge states is $v_F = 0$ for a free surface. The only non-trivial information about the edge states we can get is the *decay length* l_c represented by the inverse of the minimum of the exponential tails. The decay length can be written as

$$l_c = f(|t_2/t|, \theta)/|k_{||}| \tag{5.34}$$

diverging for $|k_{||}| \to 0$. The structure of function f is plotted in Fig. 5.6. The dips in the function are the points where the λ_1 and λ_2 exchange. They are at $\theta \in \{\pm\pi/4, \pm 3\pi/4\}$ for $|t_2/t| > 1/2$ and $\theta \in \{0, \pm\pi/2, \pi\}$ for $|t_2/t| < 1/2$ representing the d-wave structure underlying our system.

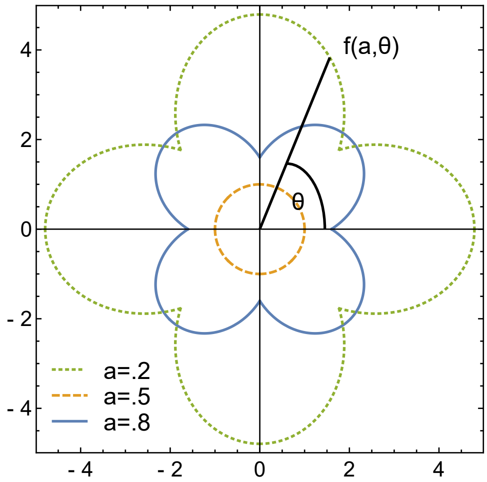

Figure 5.6: Representation of the function f as a polar plot describing the decay length of the edge states of the gapped QBCP in the checkerboard lattice.

5.5 The zero modes

The midgap energy modes of the checkerboard lattice occur however at another point of the one-dimensional BZ. This feature shows the most peculiar characteristic of the $\mathbf{k}\cdot\mathbf{p}$ model over the hemisphere: even though the topological invariant can be inferred from the low-energy bulk bandstructure, it exists a *non-local* bulk-edge correspondence predicting midgap edge states at different BZ points.

If we compare the functional dependence of the electronic characteristics of the zero modes on the band gap with respect to the BHZ model (cf. Fig. 4.7), we find that the Fermi velocity increases linearly and its decay length is independent of the gap. The TB results for the (OX) termination are shown in Fig. 5.7. A similiar behavior was found by Cano-Cortés *et al.* [67] by considering different terminations in honeycomb-like lattices.

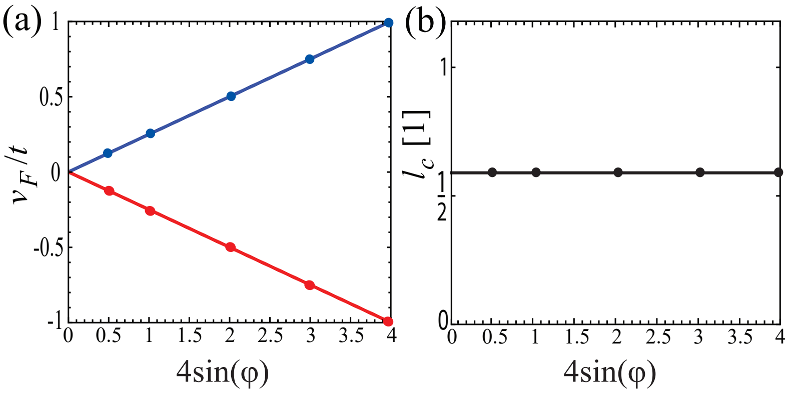

Figure 5.7: Fermi velocity and decay length of the zero modes in (OX) termination for the lattice Hamiltonian over the band gap for $t_2/t = 0.6$.

6 HgTe in 2D and 3D

In this chapter we will study a more sophisticated low-energy model describing the topological phases in time-reversal (TR) invariant materials. These TR invariant TIs are at the forefront of condensed matter physics for their huge potential applications in spintronics [79] and quantum computation.

One paradigmatic example is given by HgTe. In this material, topologically non-trivial phases were not only theoretically predicted [37, 80], but also experimentally verified [81, 82, 83]. To study HgTe within an effective continuum model we will use the well-known *Kane model* [84].

6.1 Bulk HgTe and its effective model

Pristine HgTe shows a semi-metallic behavior with the Fermi energy E_F that lies in the middle of the fourfold degenerate light-hole (LH) and heavy-hole (HH) states at the Brillouin zone (BZ) center [36, 85, 86]. The hole states have an orbital character which is p-like (the composition is shown in appendix C). Let us first consider what are the topological characteristics of the insulating state by lifting the degeneracy at the Γ-point. In this case we could consider an effective model only composed of LH and HH bands. They describe the dispersion and the low-energy excitations quite well, but do not explain the topological properties of HgTe. For this, one has to take into account the s-like Γ_6 bands, which are far below the Fermi energy. The contribution of all these bands can be studied by analyzing a TB Hamiltonian with a two-atomic basis of mercury Hg=[Xe]$f^{14}5d^{10}6s^2$ and tellurium Te=[Kr]$4d^{10}5s^25p^4$ forming the two interpenetrating fcc lattices of a zincblende lattice. The Bravais lattice vectors of this model are given by

$$\mathbf{a}_1 = \frac{1}{2}a \begin{pmatrix} 0 \\ 1 \\ 1 \end{pmatrix}, \; \mathbf{a}_2 = \frac{1}{2}a \begin{pmatrix} 1 \\ 0 \\ 1 \end{pmatrix}, \; \mathbf{a}_3 = \frac{1}{2}a \begin{pmatrix} 1 \\ 1 \\ 0 \end{pmatrix} \tag{6.1}$$

and the basis vector $\mathbf{d} = \frac{1}{4}a\{1,1,1\}$ is the shift between the two fcc lattices. The resulting

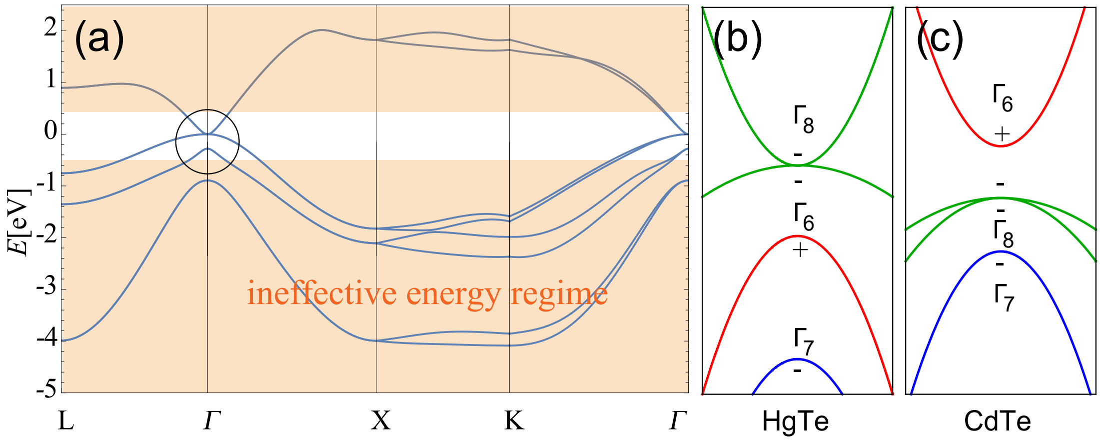

Figure 6.1: The TB results (a) for the bulk are shown in the relevant energy regime. The empirical model of HgTe is discussed in more details in Ref. [87]. At Γ we find the low-energy excitations of this system with the reversed band ordering (b) in comparison to the one of CdTe (c). The signs represent the parity of the relevant bands Γ_6 and Γ_8.

TB model can be obtained as

$$\begin{aligned}\hat{\mathcal{H}} = &\sum_{i\sigma,\mathbf{R}} \varepsilon_i^a \hat{a}^\dagger_{i\sigma,\mathbf{R}} \hat{a}_{i\sigma,\mathbf{R}} + \sum_{i\sigma,\mathbf{R}} \varepsilon_i^c \hat{c}^\dagger_{i\sigma,\mathbf{R}+\mathbf{d}} \hat{c}_{i\sigma,\mathbf{R}+\mathbf{d}} \\ &+ \sum_{\sigma ij,\mathbf{R}\mathbf{R}',\mathbf{d}} V_{ij}(\mathbf{R},\mathbf{R}'+\mathbf{d}) \hat{a}^\dagger_{i\sigma,\mathbf{R}} \hat{c}_{j\sigma,\mathbf{R}'+\mathbf{d}} + h.c. \qquad (6.2)\\ &+ \sum_{ij\sigma\sigma',\mathbf{R}} 2\lambda_a (\mathbf{L})_{ij}\cdot(\mathbf{S})_{\sigma\sigma'} \hat{a}^\dagger_{i\sigma,\mathbf{R}} \hat{a}_{j\sigma',\mathbf{R}} + \sum_{ij\sigma\sigma',\mathbf{R}} 2\lambda_c (\mathbf{L})_{ij}\cdot(\mathbf{S})_{\sigma\sigma'} \hat{c}^\dagger_{i\sigma,\mathbf{R}+\mathbf{d}} \hat{c}_{j\sigma',\mathbf{R}+\mathbf{d}},\end{aligned}$$

where we included the spin-orbit coupling (SOC) $\mathbf{L}\cdot\mathbf{S}$ for the (a)nion and the (c)ation with spin σ, orbital $i \in \{s, p, ...\}$ and lattice vector $\mathbf{R}$. The dispersion of this model is shown in Fig. 6.1 (a) using only s and p orbitals [87, 88] and realistic parameters. It shows that the low-energy excitations are close to the Γ point of the BZ.

Using the theory of invariants [84] the effective continuum model for these excitations can be constructed for the LH, HH (Γ_8) and the Γ_6 bands. This is the so-called 6-band *Kane model*. The functional form of this Hamiltonian is discussed in appendix C in detail. This model has been already successfully used to describe the Quantum Spin Hall effect in HgTe/CdTe quantum wells [71, 89].

Fig. 6.1 (b) and (c) show the main characteristics of the energy dispersion of HgTe as compared to CdTe. In the topologically CdTe, the Γ_6 bands form the conduction bands while the Γ_8 bands represent the valence bands. The inverted band ordering in HgTe, which is a consequence of the strong SOC of Hg, immediately implies a non-trivial topology since two bands of opposite parities [37] have level crossed with respect to the *normal band ordering* at the low-energy point. The latter criterion is strictly valid in the presence of inversion symmetry while the zincblende crystal structure of HgTe lacks inversion symmetry. However, it is normally considered that the bulk inversion aysmmetry (BIA) does not hinder the topological nature of the level crossing. In this chapter we will show that this assertion is verified in three-dimension but in two-dimensions inversion symmetry breaking perturbations can lead to topological changes.

6.2 HgTe/CdTe quantum wells

The topologically non-trivial properties of HgTe already appear in HgTe quantum wells (QWs), where HgTe layers are sandwiched between CdTe layers. To simulate this system, we start with the bulk-inversion symmetric 6-band Kane model in the axial approximation, where we neglect the split-off Γ_7 bands of the extended Kane model. The effective model and its parameters are discussed in the appendix. Small anisotropy effects will be treated perturbatively at the end. Following Ref. [71], one can choose the growth direction along z with CdTe for $|z| > d/2$ and HgTe for $|z| < d/2$ where d is the quantum well thickness. In the corresponding $\mathbf{k} \cdot \mathbf{p}$ theory, all parameters of the Kane model are spatial dependent. The *Luttinger parameters* γ_i are changed in $\gamma_i k_z^2 \to -\partial_z \gamma_i(z) \partial_z$ for $i = 0, 1, 2, 3$ with a functional form

$$\gamma_i(z) = \gamma_i^{(Cd)} \Theta(|z| - d/2) + \gamma_i^{(Hg)} \Theta(d/2 - |z|), \tag{6.3}$$

where $\gamma_i^{(x)}$ are the bare parameters of CdTe or HgTe respectively. Since we are interested in the electronic properties at the projected surface BZ Γ point, we set $k_x = k_y = 0$. The Hamiltonian is then

$$H_{Kane}(k_x = k_y = 0, k_z) = \begin{pmatrix} T & 0 & 0 & \sqrt{\frac{2}{3}} P k_z & 0 & 0 \\ . & T & 0 & 0 & \sqrt{\frac{2}{3}} P k_z & 0 \\ . & . & U + V & 0 & 0 & 0 \\ . & . & . & U - V & 0 & 0 \\ . & . & . & . & U - V & 0 \\ . & . & . & . & . & U + V \end{pmatrix}, \tag{6.4}$$

where $T = E_0 + B\gamma_0 k_z^2$, $U = E_v - B\gamma_1 k_z^2$ and $V = 2B\gamma_2 k_z^2$ in terms of the Kane model parameters. The Hamiltonian has two subblocks corresponding to the two TR channels. In addition, we find that the terms with coupling P describe the hybridization only between

Γ_6 and the LH-band. The HH bands are completely decoupled from the other bands. For the Γ_6 and LH states, the effective Hamiltonian reads

$$\begin{aligned} H^{1,4}_{1,4} &= \begin{pmatrix} T(z,\hat{p}_z) & \sqrt{\frac{2}{3}}P\hat{p}_z \\ . & U(z,\hat{p}_z) - V(z,\hat{p}_z) \end{pmatrix} \\ &= \begin{pmatrix} E_c(z) - B\gamma_0(z)\partial_z^2 & -i\sqrt{\frac{2}{3}}P\partial_z \\ . & E_v(z) + B(\gamma_1(z) + 2\gamma_2(z))\partial_z^2 \end{pmatrix}, \end{aligned} \tag{6.5}$$

and describes the higher-energy subbands (E1, E2, E3...) with their low-energy partners (L1, L2, L3...). The Hamiltonian for the HH is instead

$$H^3_3 = U(z,\hat{p}_z) + V(z,\hat{p}_z) = E_v(z) + B(\gamma_1(z) - 2\gamma_2(z))\partial_z^2 \tag{6.6}$$

and describes the so-called (H1, H2, H3...) subbands.
The Ei and Li subbands can be found by assuming the ansatz for the wavefunction

$$\begin{aligned} \Psi(z < -d/2) &= \begin{pmatrix} A^1 \\ A^4 \end{pmatrix} e^{-\alpha_{Cd}(E)|z|}, \\ \Psi(|z| < d/2) &= \begin{pmatrix} B^1(e^{\alpha_{Hg}(E)z} \pm e^{-\alpha_{Hg}(E)z}) \\ B^4(e^{\alpha_{Cd}(E)z} \mp e^{-\alpha_{Cd}(E)z}) \end{pmatrix} \text{ and} \\ \Psi(z > +d/2) &= \begin{pmatrix} \pm A^1 \\ \mp A^4 \end{pmatrix} e^{-\alpha_{Cd}(E)|z|}, \end{aligned} \tag{6.7}$$

where the energy-dependent parameters in front of the exponentials fulfill the following secular equation in each region

$$\frac{T_x - E}{\sqrt{\frac{2}{3}}iP\alpha_x(E)} = \frac{\sqrt{\frac{2}{3}}iP\alpha_x(E)}{U_x - V_x - E} \text{ for } x = \text{Hg,Cd}. \tag{6.8}$$

The continuity of the wavefunction and the probability current using $j(z) \propto \partial H^{1,4}_{1,4}/\partial(\partial_z)$ can be written as

$$\begin{aligned} \lim_{\delta\to 0} \Psi(z = \pm\frac{d}{2} - \delta) = \Psi(z = \pm\frac{d}{2} + \delta) \text{ and} \\ \lim_{\delta\to 0} j(z = \pm\frac{d}{2} - \delta)\Psi(z = \pm\frac{d}{2} - \delta) = j(z = \pm\frac{d}{2} + \delta)\Psi(z = \pm\frac{d}{2} + \delta), \end{aligned} \tag{6.9}$$

which leads to

$$\begin{aligned}\frac{T_{Cd}-E}{\alpha_{Cd}(E)} &= -\tanh\left[\alpha_{Hg}(E)\frac{d}{2}\right]\frac{T_{Hg}-E}{\alpha_{Hg}(E)} \text{ for Ei and}\\ \frac{U_{Cd}-V_{Cd}-E}{\alpha_{Cd}(E)} &= -\tanh\left[\alpha_{Hg}(E)\frac{d}{2}\right]\frac{U_{Hg}-V_{Hg}-E}{\alpha_{Hg}(E)} \text{ for Li.}\end{aligned} \tag{6.10}$$

Let us now consider the heavy-hole subbands Hi. In the HgTe QW the subband eigenstates will be simply standing waves. Therefore we use the ansatz

$$\begin{aligned}\Psi(z<-d/2) &= Ne^{-\tilde{\alpha}_{Cd}(E)|z|},\\ \Psi(|z|<d/2) &= Ne^{-\tilde{\alpha}_{Cd}(E)d/2}\frac{\cos/\sin(\tilde{\alpha}_{Hg}(E)z)}{\cos/\sin(\tilde{\alpha}_{Cd}(E)d/2)} \text{ and}\\ \Psi(z>+d/2) &= \pm Ne^{-\tilde{\alpha}_{Cd}(E)|z|}.\end{aligned} \tag{6.11}$$

The continuity of the wavefunction implies the two following secular equation

$$\tilde{\alpha}^2_{Cd}(E) = \frac{E-E_v^{Cd}}{B(\gamma_1^{Cd}-2\gamma_2^{Cd})} \text{ and } \tilde{\alpha}^2_{Hg}(E) = \frac{E_v^{Hg}-E}{B(\gamma_1^{Hg}-2\gamma_2^{Hg})}. \tag{6.12}$$

In addition, from the continuity of the probability current $j(z) \propto \partial H_3^3/\partial(\partial_z)$, written as

$$\lim_{\delta\to 0} j(|z|=\frac{d}{2}-\delta)\Psi(|z|=\frac{d}{2}-\delta) = j(|z|=\frac{d}{2}+\delta)\Psi(|z|=\frac{d}{2}+\delta), \tag{6.13}$$

we find the following equation

$$\frac{1}{(\gamma_1^{Cd}-2\gamma_2^{Cd})\tilde{\alpha}_{Cd}(E)} = \cot/\tan\left[\tilde{\alpha}_{Hg}(E)\frac{d}{2}\right]\frac{1}{(\gamma_1^{Hg}-2\gamma_2^{Hg})\tilde{\alpha}_{Hg}(E)}. \tag{6.14}$$

The equations above determine the subband states Ei, Hi and Li in one TR channel. The results are shown in Fig. 6.2. The most interesting part in this plot is marked with a black dot, and describes a level crossing of the E1 and H1 subbands. We also note that in the HgTe QW thickness $d \to \infty$ limit, the two E1 and L1 subbands become degenerate. We can already anticipate that these states are just the Dirac points of the Dirac cones predicted to occur on the surface of bulk HgTe.

Following Ref. [71], we can proceed further to analyze whether the level crossing of H1 and E1 at a critical thickness d_c marks a topological phase transition. By using perturbation theory and the 4 relevant low-energy subbands eigenstates $\{|\mathrm{E1},+\rangle, |\mathrm{H1},+\rangle, |\mathrm{E1},-\rangle, |\mathrm{H1},-\rangle\}$, where ± indicate the two TR channels, we can calculate the effective two-dimensional

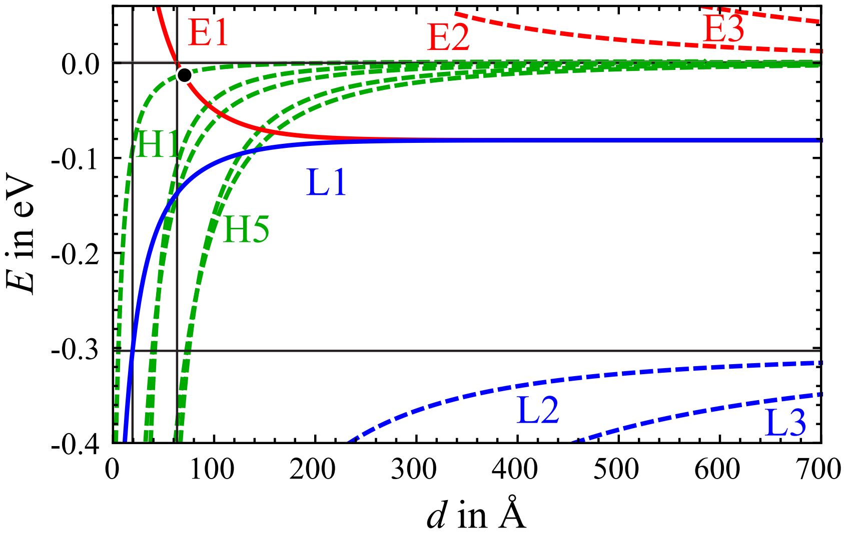

Figure 6.2: Energy of the subbands Ei, Hi and Li versus quantum well thickness d. The dashed bands are pure bulk states. The thick lines correspond to the Dirac point in $d = 3$ limit. The horizontal auxiliary lines are the band edges of pristine HgTe. The vertical ones describe the critical thickness where the two subbands of the Dirac cone become evanescent. The black dot corresponds to the critical point where E1 and H1 cross.

Hamiltonian

$$\left(H^{eff}(k_x,k_y)\right)_{ij} = \int_{-\infty}^{\infty} dz \,\langle i|H_{Kane}(k_x,k_y,-i\partial_z)|j\rangle\,. \tag{6.15}$$

It is of the form

$$H^{eff} = \varepsilon_{\mathbf{k}}\mathbb{1} + \begin{pmatrix} +\mathcal{M}(\mathbf{k}) & Ak_- & 0 & 0 \\ Ak_+ & -\mathcal{M}(\mathbf{k}) & 0 & 0 \\ 0 & 0 & +\mathcal{M}(\mathbf{k}) & -Ak_+ \\ 0 & 0 & -Ak_- & -\mathcal{M}(\mathbf{k}) \end{pmatrix} \tag{6.16}$$

with $\varepsilon_{\mathbf{k}} = C - D\mathbf{k}^2$, $\mathcal{M}(\mathbf{k}) = M - Bk^2$, $k_\pm = k_x \pm ik_y$ and $\mathbf{k} = (k_x,k_y)$. This functional form of the Hamiltonian can also be obtained using a two-dimensional theory of invariants [90]. The parameters A,B,C,D,M depend on the quantum-well thickness d. The parameters C and D are irrelevant from a topological point of view. The other parameters have the following behavior close to the critical thickness: $A < 0$, $B < 0$ and $M \propto -(d - d_c)$. Concrete values can be found for instance in Ref. [71]. This model has been already discussed in Chapter 4 of this thesis. Each block represents one spin channel of the continuum description of the BHZ model. The parameter M therefore distinguishes

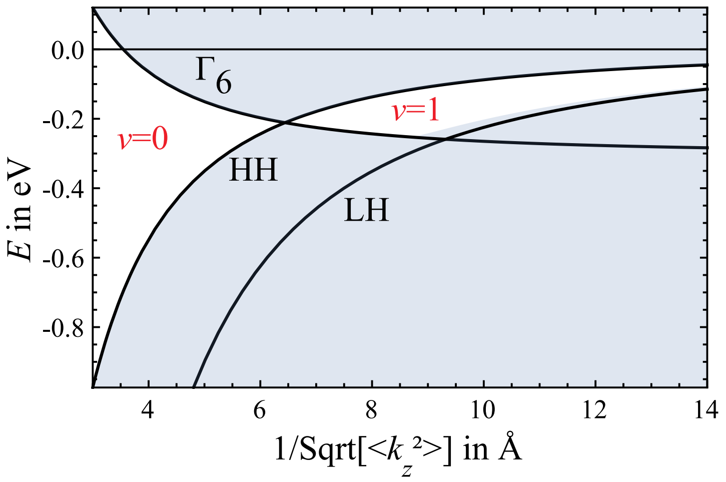

Figure 6.3: Phase transition in the quantum well approximation from the trivial ($\nu = 0$) to the Quantum Spin Hall phase ($\nu = 1$). The blue region is the projected bulk spectrum. The thick lines correspond to the energy of the bands at the point $k_x = k_y = 0$ where the bands cross.

two different topological phases.

Let us now introduce an alternative description of the topological properties of HgTe quantum wells using the so-called *quantum well approximation* [91]. We fix the expectation values of the Kane-Hamiltonian along the z-direction and substitute

$$\langle k_z \rangle = 0 \text{ and } \langle k_z^2 \rangle \approx (\pi/d)^2. \tag{6.17}$$

Using these relations we can bring the Kane model Hamiltonian after rearranging the basis set to $\{1, 3, 5, 2, 6, 4\}$ in the form [86]

$$H(k_\parallel = (k_x, k_y)) = \begin{pmatrix} h(k_\parallel) & 0 \\ . & h^*(-k_\parallel) \end{pmatrix}, \tag{6.18}$$

with the block $h(k_\parallel)$ written as

$$\begin{pmatrix} \langle T \rangle + B\gamma_0 k_\parallel^2 & -\frac{P}{\sqrt{2}} k_+ & \frac{1}{\sqrt{6}} P k_- \\ . & \langle U \rangle + \langle V \rangle - B(\gamma_1 + \bar{\gamma}) k_\parallel^2 & \sqrt{3}\bar{\gamma} B k_-^2 \\ . & . & \langle U \rangle - \langle V \rangle - B(\gamma_1 - \bar{\gamma}) k_\parallel^2 \end{pmatrix}, \tag{6.19}$$

where $\langle T \rangle = E_0 + B\gamma_0 \langle k_z^2 \rangle$, $\langle U \rangle = -B\gamma_1 \langle k_z^2 \rangle$ and $\langle V \rangle = 2B\gamma_2 \langle k_z^2 \rangle$. This block structure allows us to calculate the (Spin) Chern number for the Hamiltonian $h(k_\parallel)$. We here use the definition (2.54) and the $SU(3)$ formulation of the Chern number for a 3-band model discussed in appendix A, and get

$$\nu_{-}^{\Gamma_6} = -(\nu_{-}^{LH} + \nu_{-}^{HH}) = -\Theta(d - d_c). \tag{6.20}$$

In agreement with the foregoing analysis we find a phase transition from a trivial insulator to a quantum spin Hall insulator at a critical thickness where a level crossing between the HH and the Γ_6 subbands occurs. This is illustrated in Fig. 6.3.

6.3 Inversion-asymmetric BHZ model

Let us now consider the effect of a bulk inversion symmetry breaking term (BIA term) to the effective Hamiltonian of the HgTe QW. The spin symmetry is then totally broken, but a $\mathbb{Z}_2$ topological invariant can be still defined. Winkler et al. [92] identified a robust level coincidence in the subband structure of these quasi-2d systems implying the presence of two topologically distinct phases in the presence of small inversion-symmetry breaking perturbations. In the presence of a BIA terms, the continuous model near Γ up to the linear order can be written as [84]

$$H_{\Delta}^{eff}(\mathbf{k}) = \begin{pmatrix} M & A(k_x - ik_y) & 0 & \Delta \\ A(k_x + ik_y) & -M & -\Delta & 0 \\ 0 & -\Delta & M & -A(k_x + ik_y) \\ \Delta & 0 & -A(k_x - ik_y) & -M \end{pmatrix}. \tag{6.21}$$

Since the TR operator $\mathcal{T}$ is defined by $\mathcal{T} = i\sigma_y \otimes \sigma_0 \mathcal{K}$, $H_{\Delta}^{eff}(\mathbf{k})$ possesses TR symmetry while a finite parameter Δ breaks inversion symmetry represented by the operator $\mathcal{I} = \sigma_0 \otimes \sigma_z$ and $\mathbf{r} \to -\mathbf{r}$. The dispersion $E(k) = \pm\sqrt{M^2 + (|\Delta| \pm |A|k)^2}$ of the Hamiltonian above shows that a topological phase transition cannot occur any longer at the Γ point. We first look for interface states at a domain wall [93] assuming the mass parameter M flips sign at the interface between the right ($x > 0$) and the left side ($x < 0$). The solutions have to come in pairs for every k_y due to TR symmetry. This allows us to denote the two edge states at the domain wall

$$\Psi_{\uparrow}(x; k_y) \text{ and } \Psi_{\downarrow}(x; k_y) = \mathcal{T}\Psi_{\uparrow}(x; -k_y). \tag{6.22}$$

We first ignore the BIA term. $H_0^{eff}(\mathbf{k})$ can be divided in two independent subblocks for the up and down spins. According to this, the general solution for a mass profile

$M(x) = \mu \mathrm{sign}(x)$ with a positive μ is

$$E_\uparrow(k_y) = +|A|k_y \text{ with } \Psi_\uparrow(x;k_y) = \sqrt{\frac{\mu}{2|A|}} \begin{pmatrix} \mathrm{sign}(A) \\ +i \\ 0 \\ 0 \end{pmatrix} e^{-\mu|x/A|} \text{ and}$$

$$E_\downarrow(k_y) = -|A|k_y \text{ with } \Psi_\downarrow(x;k_y) = \sqrt{\frac{\mu}{2|A|}} \begin{pmatrix} 0 \\ 0 \\ \mathrm{sign}(A) \\ -i \end{pmatrix} e^{-\mu|x/A|}. \qquad (6.23)$$

In the next step we allow for a finite Δ. We use the entire Hamiltonian with the exponential ansatz $e^{\lambda x}$. The secular equation of the effective Hamiltonian $H^{eff}_\Delta(k_x \to -i\lambda; k_y)$ leads to four solutions $\lambda = \lambda_{1/2/3/4}(E)$

$$\begin{aligned} \lambda^2 &= \frac{1}{A^2}(M^2 - E^2) + k_y^2 - \frac{\Delta^2}{A^2} \pm i\frac{2|\Delta|}{A^2}\sqrt{M^2 - E^2} && \text{for } M^2 > E^2 \text{ or} \\ \lambda^2 &= \frac{1}{A^2}(M^2 - E^2) + k_y^2 - \frac{\Delta^2}{A^2} \pm \frac{2|\Delta|}{A^2}\sqrt{E^2 - M^2} && \text{for } E^2 \geq M^2. \end{aligned} \qquad (6.24)$$

The energy has to fulfill $M^2 > E^2$. The other choice leads to non-renormalizable solutions ($\lambda^2 < 0$) or to only one solution for λ ($\lambda^2 > 0$). We can write the four solutions of $\lambda(E)$

$$\begin{cases} \lambda_1 = +a + ib \\ \lambda_2 = -a - ib \\ \lambda_3 = +a - ib \\ \lambda_4 = -a + ib \end{cases} \text{with} \begin{cases} a = a_0 b_0 / b \\ b = -\frac{1}{\sqrt{2}}\sqrt{b_0^2 - a_0^2 - k_y^2 + \sqrt{4a_0^2 b_0^2 + (b_0^2 - a_0^2 - k_y^2)^2}} \\ a_0 = a(k_y = 0) = -\frac{1}{|A|}\sqrt{M^2 - E^2} \\ b_0 = b(k_y = 0) = -\left|\Delta/A\right| \end{cases} \qquad (6.25)$$

and the eigenvectors

$$\phi(\lambda_i) = \begin{pmatrix} \Delta(E^2 - M^2 - \Delta^2 - A^2(\lambda_i^2 - k_y^2)) \\ 2iA(E - M)\Delta(k_y - \lambda_i) \\ -iA(k_y - \Delta)(E^2 - M^2 + \Delta^2 + A^2(\lambda_i^2 - k_y^2)) \\ (E - M)(E^2 - M^2 - \Delta^2 + A^2(\lambda_i^2 - k_y^2)) \end{pmatrix}. \qquad (6.26)$$

At $k_y = 0$ we then have a Kramers doublet at zero energy whose wavefunctions are

$$\Psi_\uparrow(x;0) = \frac{1}{2}\sqrt{\frac{\mu}{|A|}}e^{-\mu|x/A|}e^{-i\Delta x/|A|}\begin{pmatrix} -i \\ \mathrm{sign}(A) \\ \mathrm{sign}(A)\mathrm{sign}(\Delta)i \\ \mathrm{sign}(\Delta) \end{pmatrix} \text{ and}$$

$$\Psi_\downarrow(x;0) = \frac{1}{2}\sqrt{\frac{\mu}{|A|}}e^{-\mu|x/A|}e^{+i\Delta x/|A|}\begin{pmatrix} \mathrm{sign}(A)\mathrm{sign}(\Delta)i \\ -\mathrm{sign}(\Delta) \\ i \\ \mathrm{sign}(A) \end{pmatrix}. \tag{6.27}$$

One can simply show that these two solutions in the $\Delta \to 0$ limit correspond, up to a unitary transformation, to the eigenstates found in the absence of inversion symmetry breaking perturbations. The effect of the BIA term is a change in the energy dispersion of the interface states. The Fermi velocities are modified to

$$v_F^\Delta = \frac{\mu^2}{\mu^2 + \Delta^2}v_F^0 \tag{6.28}$$

and terms $\propto k_y^2$ are also present. Obviously, the presence of interface states is not endangered by the BIA terms. As we have highlighted in the context of the marginal bulk-edge correspondence, the appearance of interface states does not uniquely determine the topological characteristic of the system. Therefore we study the BHZ continuous model including terms, which are quadratic in $\mathbf{k}$ as in Hamiltonian Eq. (6.16). We set $C = D = 0$ for simplicity. The quadratic terms modify the bulk dispersion to $E(k) = \pm\sqrt{(M - Bk^2)^2 + (|\Delta| \pm |A|k)^2}$. It is interesting that there exists a band crossing point driven by the inversion symmetry breaking term. The critical value at which this occurs is given by

$$|\Delta_{crit}| = \sqrt{\frac{M}{B}}|A| \text{ but only if } \frac{M}{B} > 0. \tag{6.29}$$

This shows that even if we start in the topologically non-trivial phase, inversion symmetry breaking terms can lead to a gap closing-reopening point, thereby suggesting a topological phase transition. For illustration purposes we have plotted the dispersion in Fig. 6.4 where we drive the system through the transition by tuning the strength Δ of the BIA term.

To analyze the consequence of the gap closing-reopening point we use a lattice regulariza-

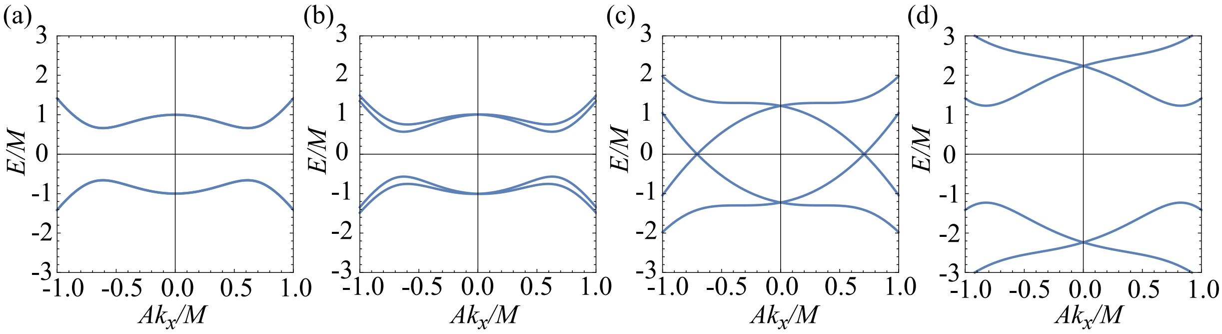

Figure 6.4: Bulk dispersion $E(k_x, k_y = 0)$ over the momentum Ak_x/M near the Γ point for $M > 0$, $B/(M\sqrt{A}) = 2$ and $\Delta/M = \{0, 0.1, \sqrt{1/2}, 2\}$ (from left to right).

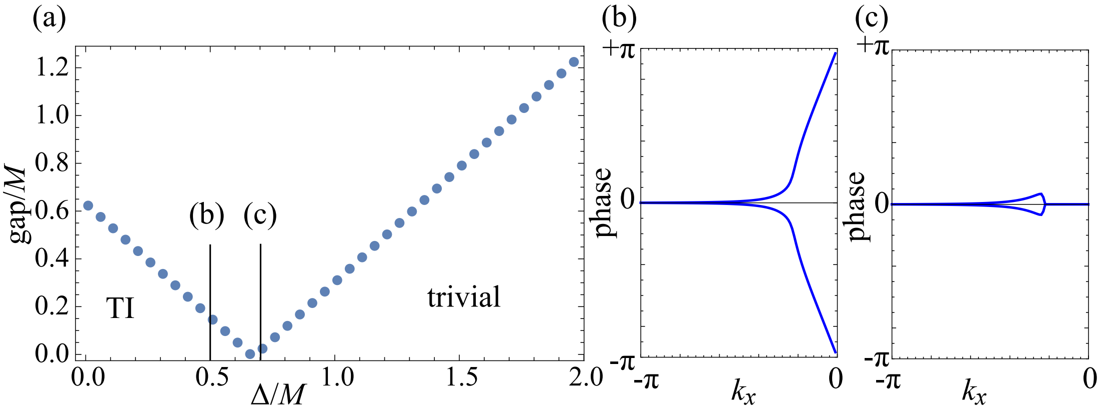

Figure 6.5: Using the square lattice to compactify the effective theory we find an equivalent band coincidence in the gap (a) like in the effective theory. The two insulating phases are characterized by an even (b) and odd number (c) of times the Wanniers center going around the cylinder using the technique of the nonabelian Berry connection explained in paragraph 2.6. The parameters are the same like in Fig. 6.4.

tion of the BHZ model obtained by substituting

$$k_i \rightarrow \sin k_i \text{ and } k_i^2 \rightarrow 2(1 - \cos k_i). \tag{6.30}$$

Within this TB model we can check whether the gap closing-reopening is accompanied by a topological phase transition. It turns out that this is the case. By using the formulation of the topological invariant in terms of the nonabelian Berry connection discussed in paragraph 2.6, we find a topological phase transition driven by the BIA term from a quantum spin Hall insulator a a trivial insulator (see Fig. 6.5). Therefore, sufficiently strong BIA terms can potentially destroy the topologically non-trivial phase in HgTe QWs.

6.4 Strained bulk HgTe

We now move to analyze the topological properties of bulk HgTe. As we have previously discussed, the topologically non-trivial properties of HgTe come about the inverted band ordering between the Γ_6 and the LH and HH bands. However, pristine HgTe is a semimetal rather than an insulator. In a semimetal with an inverted band ordering topological surface states can in principle coexist with bulk states. This, in turn, has suggested the notion of a *helical semimetallic* state. In a helical semimetallic state, the presence of surface states is not topologically protected by TR symmetry alone. Indeed, surface states generally overlap in energy with bulk states at different momenta. The protection of surface states then relies on additional continuous symmetries. For pristine HgTe, Ortix and collaborators [94] have shown that the presence of surface states strictly relies on the presence of bulk inversion symmetry. Even infinitesimally small bulk inversion-symmetry breaking perturbations render the topological surface states and hence the helical semimetallic state unstable.
The topological insulating regime in HgTe can be reached by lifting the fourfold degeneracy of the Γ_8 states at the zone center via a compressive uniaxial strain [81]. Epitaxial strain due to lattice mismatch in a heterostructure can be taken into account by applying a formalism introduced by Bir and Pikus (BP) [95]. The effect of strain is the transformation of the unstrained lattice vectors $\mathbf{R}_i$ to the strained lattice vectors $\mathbf{R}'_i$ through the relation

$$\mathbf{R}'_i = (\mathbb{1} + \hat{\varepsilon})\mathbf{R}_i, \tag{6.31}$$

where $\hat{\varepsilon}$ is the 3×3 strain tensor. The strain-induced terms can be simply incorporated into the $\mathbf{k}\cdot\mathbf{p}$ band structure calculation using the substitution $H \to H + H_{BP}$. The functional form of H_{BP} corresponds to the unstrained $\mathbf{k}\cdot\mathbf{p}$ Hamiltonian substituting terms quadratic in momentum as

$$k_i k_j \to \varepsilon_{ij}, \tag{6.32}$$

where $\varepsilon_{ij} = (\hat{\varepsilon})_{ij}$ are the strain tensor components. In addition, the $\mathbf{k}\cdot\mathbf{p}$ parameters are changed to new parameters, *e.g.*

$$B\gamma_0 \to C, B\gamma_2 \to -b \text{ and } B\gamma_3 \to -\frac{1}{\sqrt{3}}d, \tag{6.33}$$

known as *deformation potentials.* The main effect of strain is to introduce a shift in the conduction and valence band edges. In particular, uniaxial, or biaxial strain generally removes band degeneracies. In the remainder, we will consider strain obtained by epitaxial growth of a material onto a substrate with different lattice constant. For HgTe this can be achieved by epitaxial growth on CdTe. The in-plane contraction ($\varepsilon_{\|} < 0$) or dilation ($\varepsilon_{\|} > 0$) of the interface in the heterostructure is determined by the lattice mismatch [96]

$$\varepsilon_{\|} = \frac{a_{CdTe} - a_{HgTe}}{a_{HgTe}} \approx 0.003 > 0, \tag{6.34}$$

where a_x are the two lattice constants of the materials. Growth of HgTe in the (001) direction yields the strain tensor

$$\hat{\varepsilon} = \varepsilon_{\|} \begin{pmatrix} 1 & 0 & 0 \\ 0 & 1 & 0 \\ 0 & 0 & -2\frac{C_{12}}{C_{11}} \end{pmatrix} \tag{6.35}$$

with the positive elastic stiffness constants C_{11} and C_{12} given in Ref. [97]. In the extended 6×6 Kane model we can write the BP Hamiltonian as

$$H_{BP} = \begin{pmatrix} T_\varepsilon & 0 & 0 & 0 & 0 & 0 \\ . & T_\varepsilon & 0 & 0 & 0 & 0 \\ . & . & U_\varepsilon + V_\varepsilon & S_\varepsilon & R_\varepsilon & 0 \\ . & . & . & U_\varepsilon - V_\varepsilon & 0 & R_\varepsilon \\ . & . & . & . & U_\varepsilon - V_\varepsilon & -S_\varepsilon \\ . & . & . & . & . & U_\varepsilon + V_\varepsilon \end{pmatrix} \tag{6.36}$$

with strain-induced terms (see Ref. [47])

$$\begin{aligned} &T_\varepsilon = C \ \mathrm{tr}\hat{\varepsilon},\ U_\varepsilon = a \ \mathrm{tr}\hat{\varepsilon},\ V_\varepsilon = \frac{b}{2}(\mathrm{tr}\hat{\varepsilon} - 3\varepsilon_{zz}), \\ &S_\varepsilon = -d(\varepsilon_{xz} - i\varepsilon_{yz}) \text{ and } R_\varepsilon = -\frac{\sqrt{3}}{2}b(\varepsilon_{xx} - \varepsilon_{yy}) + id\varepsilon_{xy}. \end{aligned} \tag{6.37}$$

In order to study the low-energy properties in presence of epitaxial strain, we will ignore the volumetric part of the strain, which changes the energy difference between the Γ_6 and the hole band edges characterized by the deformation potential difference

$$C - a = (-3.69 \pm 0.1) \text{ eV (from Ref. [98])}. \tag{6.38}$$

The remaining part corresponds to an effective uniaxial strain along the (001) direction with an effective BP Hamiltonian with functional form

$$H_{BP} = \mathrm{diag}(\{0, 0, -\Delta\varepsilon, \Delta\varepsilon, \Delta\varepsilon, -\Delta\varepsilon\}). \tag{6.39}$$

In the equation above we introduced the parameter

$$\Delta\varepsilon = -V_\varepsilon = -b\varepsilon_\parallel \left(1 + 2\frac{C_{12}}{C_{11}}\right), \tag{6.40}$$

which is proportional to the deformation potential

$$b = (-1.5 \pm 0.2)\ \mathrm{eV}\ \text{(from Ref. [99])}. \tag{6.41}$$

For HgTe grown on CdTe $\Delta\varepsilon > 0$ corresponding to compressive strain. Clearly tensile strain $\Delta\varepsilon < 0$ can be realized if HgTe is epitaxially grown on a substrate with smaller lattice constant. For tensile strain, the LH band edge is smaller than the HH band edge. In this case, the analysis of the inversion-symmetric Kane model Hamiltonian yields the presence of two four-time degenerate band crossing points at finite $\pm k_z$ and $k_x = k_y = 0$. The presence of these degeneracy points, in turns, defines a *Dirac semimetal phase* [100]: the bands disperse linearly in all direction away from the band crossing points. Taking into account the broken bulk inversion symmetry each Dirac point splits into two *Weyl nodes*: materials with a zincblende crystal structure cannot host indeed a Dirac semimetal [101]. Weyl nodes come in pairs and carry opposite topological charge like two magnetic monopoles [102]. In addition, if the Weyl nodes reside exactly at the Fermi level of a system, the Weyl semimetal metals is referred to as *ideal*. Ruan et. al [103] have shown that under a broad range of in-plane compressive strain (tensile uniaxial strain) HgTe realizes precisely this phase.

For compressive strain instead HgTe realize a strong three-dimensional TI phase [37]. We emphasize that we can identify different surfaces of strained HgTe (see Fig. 6.6). We dub the surface orthogonal to the uniaxial strain direction as *main surface*. Surfaces, which are orthogonal to the main surface will be dubbed as *side surfaces*. The difference between main and side surfaces is manifested in the qualitatively different behavior of the projected bulk spectrum as shown in Fig. 6.6 (b), (c).

6.5 Löwdin partioning of the extended Kane model

Before analyzing the 6-band Kane model in full glory, we show that the presence of Γ_6 band is essential not only to capture the topology of strained HgTe but also for the appearance

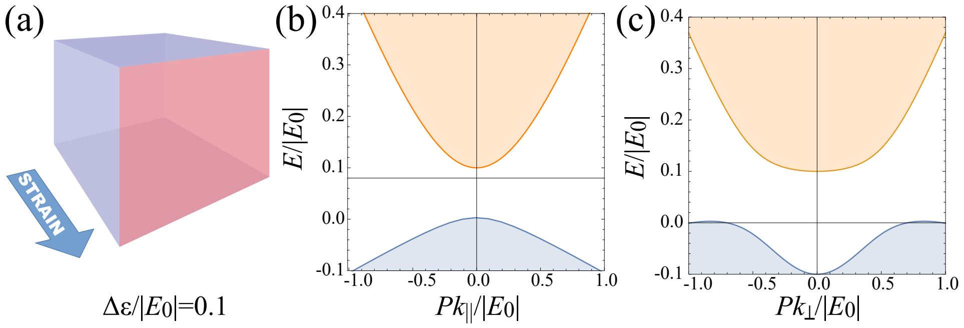

Figure 6.6: Projected bulk spectrum of uniaxial strained HgTe in the axial approximation without bulk inversion asymmetry of the side surfaces (blueish in (a)) and the main face (redish in (a)) are shown in (b) and (c) respectively.

of surface states. We start with an effective 4×4 Hamiltonian for the HH and LH bands describing strained HgTe. To do so, we have to integrate out all the other bands of the 8×8 Kane model, and derive an effective 4×4 $\mathbf{k} \cdot \mathbf{p}$ Hamiltonian. This procedure is known as *Löwdin partioning* [61] or *quasi-degenerate perturbation theory* – an idea already incorporated in the $\mathbf{k} \cdot \mathbf{p}$ expansion.

Assuming we treat k_x, k_y, k_z and $\Delta\varepsilon$ as small perturbations, the HH and LH (set A) are degenerate at the BZ center. The other states (set B) show a large energy separation with respect to these bands. If we start a perturbative expansion for the LH and HH bands, the new effective Hamiltonian $\hat{H}'_{\Gamma_8}$ for the bands $a, b \in A$ is obtained from

$$\langle a|\hat{H}'_{\Gamma_8}(\mathbf{k})|b\rangle = \langle a|\hat{H}(\mathbf{k})|b\rangle + \sum_{i,j} k_i k_j \sum_{c\in B} \langle a|\hat{H}_i|c\rangle \langle c|\hat{H}_j|b\rangle \left(\frac{1}{E_a - E_c} + \frac{1}{E_b - E_c}\right) \tag{6.42}$$

up to the second order in momentum. In the equation above, $E_a = \langle a|\hat{H}(0)|a\rangle$ are the energies at Γ of the 8×8 Kane Hamiltonian $\hat{H}(\mathbf{k})$ and $\hat{H}_i$ are the linear terms of the Hamiltonian along k_i. This perturbative expansion yields an Hamiltonian known as *Luttinger model*, which is characterized by Luttinger parameters renormalized by the Γ_6 and the split-off spin-orbit bands. The renormalization of the Luttinger parameters reads

$$\begin{aligned}
\gamma_1' &= \gamma_1 - \frac{P^2}{3B(E(\Gamma_8) - E(\Gamma_6))} - \frac{C_k^2}{4B(E(\Gamma_8) - E(\Gamma_7))},\\
\gamma_2' &= \gamma_2 - \frac{P^2}{6B(E(\Gamma_8) - E(\Gamma_6))} + \frac{C_k^2}{8B(E(\Gamma_8) - E(\Gamma_7))} \quad \text{and}\\
\gamma_3' &= \gamma_3 - \frac{P^2}{6B(E(\Gamma_8) - E(\Gamma_6))} - \frac{C_k^2}{8B(E(\Gamma_8) - E(\Gamma_7))},
\end{aligned} \tag{6.43}$$

where $E(\Gamma_i)$ are the energies of the bands Γ_i at Γ, γ_i the parameters of the $8{\times}8$ Hamiltonian and P, C_k are the linear order terms in the Kane model. C_k is the first order correction due to BIA. The functional form of the Luttinger model for a material with an inversion asymmetric crystal structure, such as the zincblende crystal structure, is given by

$$\begin{aligned}\hat{H}'_{\Gamma_8}(\mathbf{k}) = &- B\left(\gamma'_1 + \frac{2}{3}\gamma'_2 J^2\right) k^2 - 2B\gamma'_2 J_i^2 k_i^2 - 2B\gamma'_3 \left(\{J_x, J_y\}k_x k_y + c.p.\right) \\ &+ \frac{1}{\sqrt{3}} C_k \left[\{J_x, J_y^2 - J_z^2\}k_x + c.p.\right] - \Delta\varepsilon(J_z^2 - \frac{1}{3}J^2),\end{aligned} \tag{6.44}$$

where c.p. denotes the cyclic permutation of the terms. Let us now investigate on whether this model predicts the presence of topological surface states at the surface BZ center of the main surface. We thus set $k_\parallel^2 = k_x^2 + k_y^2 = 0$ thereby obtaining the Hamiltonian

$$\hat{H}'_{\Gamma_8}(k_z, 0, 0) \simeq \begin{pmatrix} U + V - \Delta\varepsilon & 0 & C_k k_z & 0 \\ 0 & U - V + \Delta\varepsilon & 0 & -C_k k_z \\ C_k k_z & 0 & U - V + \Delta\varepsilon & 0 \\ 0 & -C_k k_z & 0 & U + V - \Delta\varepsilon \end{pmatrix}_A, \tag{6.45}$$

with $U = -B\gamma'_1 k_z^2$ and $V = 2B\gamma'_2 k_z^2$. Using the unitary transformation

$$U_{AB} = \begin{pmatrix} 1 & 0 & 0 & 0 \\ 0 & 0 & 0 & 1 \\ 0 & 1 & 0 & 0 \\ 0 & 0 & 1 & 0 \end{pmatrix}_B, \tag{6.46}$$

from the original A basis to a new B basis, the Hamiltonian can be brought in a block structure and is equivalent to a BHZ model. Using the ansatz for the wavefunction

$$\Phi_\uparrow \to \begin{pmatrix} \Psi^+ \\ 0 \end{pmatrix}_B \exp\lambda z \text{ and } \Phi_\downarrow \to \begin{pmatrix} 0 \\ \Psi^- \end{pmatrix}_B \exp\lambda z \tag{6.47}$$

in the B basis, we can solve the effective Schrödinger equation for the two independent blocks using fixed boundary conditions. This can be achieved using the same technique encountered earlier in this thesis. We find the energy of the surface Kramer's double – the Dirac point (DP) – and the inverse of the decay length of the surface states determined by

$$E_{DP} = -\frac{\gamma'_1}{2\gamma'_2}\Delta\varepsilon,\ (\lambda_1 + \lambda_2)^2 = \frac{C_k^2}{B^2(4\gamma'^2_2 - \gamma'^2_1)} > 0 \text{ and } \lambda_1\lambda_2 = \frac{\Delta\varepsilon}{2B\gamma'_2} > 0. \tag{6.48}$$

With these equations one can investigate the conditions for the existence of the DP of the surface states. They are given by: $|\gamma_1'| < 2|\gamma_2'|$ and $\Delta\varepsilon\gamma_2' > 0$. If these conditions are satisfied, then the two λ's can be written as

$$\lambda_{1/2} = -\frac{1}{2}\sqrt{\frac{C_k^2}{B^2(4\gamma_2'^2 - \gamma_1'^2)}} \pm \sqrt{\frac{C_k^2}{4B^2(4\gamma_2'^2 - \gamma_1'^2)} - \frac{\Delta\varepsilon}{2B\gamma_2'}} \tag{6.49}$$

and the wavefunction of the surface states for each block is

$$\Psi^{\pm}(z) \propto \begin{pmatrix} \pm\mathrm{sign}(C_k\gamma_2') i\sqrt{1+\frac{\gamma_1'}{2\gamma_2'}} \\ \sqrt{1-\frac{\gamma_1'}{2\gamma_2'}} \end{pmatrix} \left[e^{\lambda_1 z} - e^{\lambda_2 z}\right]. \tag{6.50}$$

The topological nature of these surface states can be shown at $k_\parallel \neq 0$ by demonstrating the spin-momentum locking of the surface states. We start by writing the total angular momentum operators

$$\hat{J}_x \simeq \sigma_x \otimes \begin{pmatrix} 0 & \frac{\sqrt{3}}{2} \\ \frac{\sqrt{3}}{2} & 1 \end{pmatrix}_B, \hat{J}_y \simeq \sigma_y \otimes \begin{pmatrix} 0 & \frac{\sqrt{3}}{2} \\ \frac{\sqrt{3}}{2} & -1 \end{pmatrix}_B \text{ and } \hat{J}_z \simeq \sigma_z \otimes \begin{pmatrix} \frac{3}{2} & 0 \\ 0 & -\frac{1}{2} \end{pmatrix}_B \tag{6.51}$$

in the B basis. This allows us to investigate the angular momentum decomposition of the surface states. The expectation values of the total angular momentum of the DP are given by

$$\int_0^\infty dz\ \Phi_a^\dagger \frac{\hat{J}_x \pm \hat{J}_y}{\sqrt{2}} \Phi_b = C_\pm \frac{(\sigma_x \mp \sigma_y)_{ab}}{2\sqrt{2}} \text{ and } \int_0^\infty dz\ \Phi_a^\dagger \hat{J}_z \Phi_b = C_z \frac{(\sigma_z)_{ab}}{2}, \tag{6.52}$$

with coefficients

$$C_\pm = \frac{\gamma_1'}{2\gamma_2'} - 1 \pm \sqrt{3}\mathrm{sign}(C_k\gamma_2')\sqrt{1 - \frac{\gamma_1'^2}{4\gamma_2'^2}} \text{ and } C_z = \frac{\gamma_1' + \gamma_2'}{\gamma_2'}. \tag{6.53}$$

Away from the DP, the surface state dispersion can be calculated using perturbation theory. We have

$$\Delta\hat{H}'_{\Gamma_8}(\mathbf{k}) = \frac{1}{\sqrt{3}} C_k \left[\{J_x, J_y^2 - J_z^2\}k_x + \{J_y, J_z^2 - J_x^2\}k_y\right]. \tag{6.54}$$

As a result, we then get a spin-momentum locked dispersion reading

$$\Delta H_{eff} = v_F^1 k_1 \sigma_1 + v_F^2 k_2 \sigma_2 \text{ with } v_F^{1/2} = -\frac{C_k}{2}\left(\sqrt{3} \mp \text{sign}(C_k \gamma_2')\sqrt{1 - \frac{\gamma_1'^2}{4\gamma_2'^2}}\right), \tag{6.55}$$

where $k_{1,2} = (k_x \pm k_y)/\sqrt{2}$ and $\sigma_{1,2} = (\sigma_x \pm \sigma_y)/\sqrt{2}$. This corresponds to an anisotropic Dirac cone along the diagonal directions of the surface BZ where $v_F^{1/2}$ represent the non-equivalent Fermi velocities.

Nevertheless, by using realistic parameters of strained HgTe ($\varepsilon > 0$) it turns out that the renormalized Luttinger parameters fulfill $|\gamma_1'| < 2|\gamma_2'|$ and $\gamma_2' < 0$. This point is in contradiction with the condition that the product of strain and the Luttinger parameter γ_2' has to be positive. The DP only exists in the regime $\Delta\varepsilon < 0$ for HgTe, which is in the Weyl semimetal phase [103].

The question that arises is whether the effective theory predicts the presence of topological surface states in the strong TI phase even if there is not any surface Kramer's doublet. We have therefore solved the Schrödinger equation for $k_x \neq 0$ and $k_y = 0$ without employing perturbation theory. The solution for the inverse decay lengths for $C_k = \gamma_1' = 0$ and $\gamma_2' = \gamma_3' < 0$ reads

$$\lambda_1^2 \lambda_2^2 = k_x^4 + \frac{\Delta\varepsilon k_x^2}{2\gamma_2'} + \frac{\Delta\varepsilon^2}{4\gamma_2'^2} \text{ and } \lambda_1 \lambda_2 = \frac{\Delta\varepsilon}{2B\gamma_2'} + \frac{k_x^2}{2}. \tag{6.56}$$

These two equations cannot be concomitantly satisfied for all k_x which therefore implies the global absence of topological surface states. The reason for this behavior is quite clear: the Luttinger model does not describe the topological properties originating from the inverted band ordering of the Γ_6 and Γ_8 bands.

To obtain topological surface states in the strong TI phase within a 4 × 4 Hamiltonian, one has to introduce a model accounting for the Γ_6 and the LH bands. Löwdin partitioning is not an option since in the unstrained $\Delta\varepsilon \to 0$ limit the HH and LH bands are degenerate, and renormalization would lead to divergences. Nevertheless, we can assume that the strain is so large that the HH bands are pushed below the Γ_6 bands. Ignoring renormalization effects of the Luttinger parameters the resulting model can be explicitly written as

$$\hat{H}(\mathbf{k}) \simeq \begin{pmatrix} T & 0 & \sqrt{\frac{2}{3}}Pk_z + \chi_+ & \frac{P}{\sqrt{6}}k_- + \xi_+ \\ 0 & T & -\frac{P}{\sqrt{6}}k_+ + \xi_- & \sqrt{\frac{2}{3}}Pk_z + \chi_- \\ \sqrt{\frac{2}{3}}Pk_z - \chi_- & -\frac{P}{\sqrt{6}}k_- + \xi_+ & U - V & \frac{\sqrt{3}}{2}C_k k_+ \\ \frac{P}{\sqrt{6}}k_+ + \xi_- & \sqrt{\frac{2}{3}}Pk_z - \chi_+ & \frac{\sqrt{3}}{2}C_k k_- & U - V \end{pmatrix}, \tag{6.57}$$

where $T = E_0 + B\gamma_0 k^2$, $U - V = -B\gamma_1 k^2 + B\gamma_2(k_x^2 + k_y^2 - 2k_z^2)$, $\xi_\pm = B_8^+/\sqrt{6}k_\pm k_z$ and $\chi_\pm = (iB_8^+ k_x k_y \pm B_8^-(k_x^2 - k_y^2))/\sqrt{6}$ in the basis $\{\Gamma_6, |3/2, \pm 1/2\rangle\}$. We first check whether this Hamiltonian is one-point compactified. The projector of the highest band pair (+) at Γ is given by

$$P_+^{\uparrow/\downarrow}(\Gamma) = |3/2, \pm 1/2\rangle \langle 3/2, \pm 1/2| \,, \tag{6.58}$$

where ↑ / ↓ describe the two TR partners. At ∞ we find instead a non well-defined behavior. This can be seen if one considers the projector in the z direction

$$P_+^{\uparrow/\downarrow}((0,0,\infty)) = |1/2, \pm 1/2\rangle \langle 1/2, \pm 1/2| \tag{6.59}$$

and compare it with the projector in the x-direction which is a mixture of LH and Γ_6 bands. As it stands the model is *marginal*.

This would in principle forbid us to study the Kane model in the low-energy sector. Happily, by neglecting the inversion symmetry-breaking parameters $B_8^\pm$, we get a TR invariant and *spherical* model for HgTe. The Hamiltonian is a BHZ-like model but in $3d$, and thus shows topological surface states connecting the valence and the conduction bands with a Dirac cone dispersion. The two DP solutions at the energy $E_{DP} = (\gamma_1 + 2\gamma_2)/(\gamma_0 + \gamma_1 + 2\gamma_2)E_0$ for an edge $z > 0$ are

$$\Psi_1 \propto \begin{pmatrix} i\sqrt{-B_2} \\ 0 \\ \sqrt{B_1} \\ 0 \end{pmatrix} (e^{\lambda_1 x} - e^{\lambda_2 x}) \text{ and } \Psi_2 \propto \begin{pmatrix} 0 \\ i\sqrt{-B_2} \\ 0 \\ \sqrt{B_1} \end{pmatrix} (e^{\lambda_1 x} - e^{\lambda_2 x}), \tag{6.60}$$

where we introduced new parameters $E_1 = E_0$, $E_2 = 0$, $B_1 = B\gamma_0$, $B_2 = -B(\gamma_1 + 2\gamma_2)$ and $P' = \sqrt{2/3}P$, which describe the exponents

$$\lambda_{1/2} = -\frac{P'}{2\sqrt{-B_1 B_2}} \pm \frac{1}{2}\sqrt{\frac{(B_1 - B_2)(P')^2 - 4B_1 B_2(E_1 - E_2)}{-B_1 B_2 (B_1 - B_2)}}. \tag{6.61}$$

The Dirac cone Hamiltonian is then

$$H_{eff} = E_{DP}\mathbb{1}_{2\times 2} - \frac{\sqrt{-B_1 B_2}}{B_1 - B_2} P' (\sigma_1 k_2 - \sigma_2 k_1) + \frac{\sqrt{3}}{2}\frac{B_1}{B_1 - B_2} C_k (\sigma_1 k_2 + \sigma_2 k_1) \,, \tag{6.62}$$

where $\sigma_{1/2} = (\sigma_x \mp \sigma_y)/\sqrt{2}$ and $k_{1/2} = (k_x \mp k_y)/\sqrt{2}$. The main effect of the BIA terms is to create an asymmetry in the Dirac cone. This asymmetry is maximal if C_k reaches the value

$$|C_k^{crit}| = \frac{2}{\sqrt{3}}\sqrt{\frac{-B_2}{B_1}}P' \approx 2.3P, \tag{6.63}$$

where the *helicity* defined by the product of both Fermi velocities along the diagonals flips sign. We do not want to discuss this scenario in more detail because in reality this value will never be reached due to the natural smallness of $C_k \ll P$.

Let us come back to a more realistic picture where the parameter C_k and the strain is small. In this case, we have to take the HH into account. A large portion of the gap between $E(\Gamma_6) = E_0$ and $E(LH) = 0$ is filled with HH bulk states. This in turn shows that we have to study the full 6×6 model of Γ_6 and Γ_8 for the correct Hamiltonian of strained HgTe.

We first ask ourselves whether our continuum model is topologically well-defined. Starting with the inversion symmetric case we find that the projector of the highest bands fulfills the condition

$$P_+^{\uparrow/\downarrow}(\Gamma) = |3/2, \pm 1/2\rangle\langle 3/2, \pm 1/2| \text{ and } P_+^{\uparrow/\downarrow}(\infty) = |1/2, \pm 1/2\rangle\langle 1/2, \pm 1/2|\,. \tag{6.64}$$

Comparing both TRIM points Γ and ∞ we find that the highest band show a parity flip which indicates that we have a strong TI phase. In the realistic inversion-symmetry broken case the situation changes and the model turns out to be marginal. As before, the theory however can be one-point compactified if we ignore the quadratic BIA terms parametrized by $B_8^{\pm}$.

6.6 Mirror Chern numbers of HgTe

Uniaxially strained HgTe is not only a strong TI, but also a *Mirror Chern insulator* [104]. To analyze in detail the 6×6 Hamiltonian, we will make use of these weak topological invariants – the mirror Chern numbers (MCNs) – which are topologically protected by crystallographic mirror symmetries.

To understand the real nature behind these mirror symmetries we have to study the *space groups* [105] of HgTe. The elements of a space group can be represented with the Seitz symbols $\{R|t\}$ describing the combination of a point group element R with the translation vector t.

Assuming we neglect the BIA of the zincblende crystal structure of HgTe, the symmetry group of the crystal in the absence of strain is the group # 227 ($Fd-3m$), whereas in the real zincblende structure, the group is # 216 ($F-43m$). The space group # 216 of HgTe contains 6 mirror planes, which are the diagonal planes represented by

$$\{m_{[110]}|0\}, \{m_{[\bar{1}10]}|0\} \text{ and } c.p.. \tag{6.65}$$

In addition there are 3 glide-operations for each of these 6 mirror planes. For a diamond crystal (# 227) the space group contains all mirror and glide planes of # 216 plus 16 additional glide plane operations

$$\{m_a|t\}, \text{ where } a = \{[100] + c.p.\} \text{ and } t = \{(1/4, 1/4, 1/4), (1/4, 3/4, 3/4) + c.p.\}. \tag{6.66}$$

The mirror symmetries found in the space group analysis correspond directly to symmetries in the $\mathbf{k}\cdot\mathbf{p}$ Hamiltonian. This also holds for the glide operations. In Ref. [105] (Tab. C.6) it is shown that the space groups (# 227 and # 216) lead respectively to the point groups O_h (diamond) and T_d (zincblende) at the low-energy expansion point Γ. The $\mathbf{k}\cdot\mathbf{p}$ expansion at the Γ point for a diamond crystal is invariant under the 48 operations of the point group O_h, which correspond to the 24 operators of the point group T_d plus additional 24 operators which act like a mirror symmetry [106]. Glide operations are indeed *isomorphic* to mirror symmetries in the $\mathbf{k}\cdot\mathbf{p}$ theory.

Straining HgTe along [001] changes the space group from the non-symmorphic #216 to a symmorphic group #111 ($P-42m$) [107]. All operations can be written as [108]

$$\{1|0\}, \{-4^{+}_{[001]}|0\}, \{-4^{-}_{[001]}|0\}, \{2_{[001]}|0\}, \{2_{[010]}|0\}, \{2_{[100]}|0\}, \{m_{[110]}|0\}, \{m_{[1\bar{1}0]}|0\}, \tag{6.67}$$

where the nomenclature for the R-part is the following: m is a reflection, 1 is the identity, -1 the inversion, the numbers 2, 3, 4, 6 are used for rotations, -3, -4, -6 are the rotoinversions, and the superscript $\pm$ indicates the sense of the rotation.

This shows us that taking into account the broken inversion symmetry of HgTe only two mirrors planes ([110] and [1$\bar{1}$0]) are preserved in presence of uniaxial strain. However, by neglecting the BIA the $\mathbf{k}\cdot\mathbf{p}$ Hamiltonian has three additional *isomorphic* mirror symmetries $M_{x,y,z}$ with respect to the [100], [010] and [001] planes. For the further discussion we want to drop the word isomorphic and say simply that strained HgTe described by the $\mathbf{k}\cdot\mathbf{p}$ Hamiltonian has 5 mirror planes assuming the point group O_h and 2 mirror symmetries considering the T_d point group at the Γ point.

We want to remark that the whole analysis can be also done for the strain directions [100] and [010] . They are equivalent by applying a ±120° rotation around [111] direction

With this understanding, we can start to study the inversion-symmetric 6×6 Hamiltonian in the axial approximation $\bar{\gamma} = \gamma_2 = \gamma_3$. All definitions of the mirror operators are reported in appendix D. As mentioned above, the presence of an uniaxial strain reduces the number of mirror planes but preserves the mirror symmetry with respect to the [100], [010], and [001] planes. Since the Kane model Hamiltonian commutes with the corresponding mirror symmetry operations at the three planes $k_{x,y,z} = 0$, all eigenstates can be classified according to their $\pm i$ mirror parity. Let us consider for example the M_z mirror symmetry whose operator reads

$$M_z = i\mathrm{diag}(+1, -1, +1, -1, +1, -1, -1, +1). \tag{6.68}$$

The Kane Hamiltonian can be written for $k_z = 0$ in the block form

$$H(k_x, k_y, 0) = \begin{pmatrix} \mathcal{H}_{+i} & 0 \\ \cdot & \mathcal{H}_{-i} \end{pmatrix}. \tag{6.69}$$

We can then study the topological properties at $k_z = 0$ in each mirror channel considering a uniaxial strain along the [001] direction, or along the [100] or [010] directions. This leads to two different Hamiltonians

$$\mathcal{H}_{+i}^{[001]} = \begin{pmatrix} T & -\frac{P}{\sqrt{2}}k_+ & \frac{P}{\sqrt{6}}k_- \\ \cdot & U + V - \Delta\varepsilon & \sqrt{3}B\bar{\gamma}k_-^2 \\ \cdot & \cdot & U - V + \Delta\varepsilon \end{pmatrix} \tag{6.70}$$

for strain along [001] and

$$\mathcal{H}_{+i}^{[100]/[010]} = \begin{pmatrix} T & -\frac{P}{\sqrt{2}}k_+ & \frac{P}{\sqrt{6}}k_- \\ \cdot & U + V + \frac{\Delta\varepsilon}{2} & \sqrt{3}B\bar{\gamma}k_-^2 \mp \frac{\sqrt{3}}{2}\Delta\varepsilon \\ \cdot & \cdot & U - V - \frac{\Delta\varepsilon}{2} \end{pmatrix} \tag{6.71}$$

for strain along [100]/[010]. As usual, we introduced $T = E_0 + B\gamma_0(k_x^2 + k_y^2)$ and $U \pm V = -B(\gamma_1 \pm \bar{\gamma})(k_x^2 + k_y^2)$. All information are encoded in those two simple models which are much easier to study than the full 6×6 Hamiltonian. The big advantage of considering the mirror planes is that we can define a new topological invariant. For each block we can introduce a Chern number $\nu_{\pm i}$. Due to TR symmetry the sum of the Chern numbers of both mirror blocks $\nu_{\pm i}$ has to vanish. Nevertheless, we can define a *Mirror Chern number* (MCN) [104] similar to the *Spin Chern number* for quantum spin-Hall insulators as the difference of both blocks

$$\nu_M \equiv \frac{\nu_{+i} - \nu_{-i}}{2} = \nu_{+i}, \tag{6.72}$$

which represents a new *weak* topological invariant. Following Ref. [109] and Ref. [110], our 3×3 Hamiltonians and the projectors for each band can be represented with the help of a $SU(3)$ matrices as shown in the appendix A. These expressions allow us to study the MCNs in terms of quantities from the 3×3 mirror block of the Kane model Hamiltonian. We find that at the $k_z = 0$ mirror plane, the MCN $\nu_{+i} = -1$ for strain along [001] direction, while for strain along [100] and [010] the invariant $\nu_{+i} = +1$.

Let us compare these MCNs with those appearing in the closely related material *meta-cinnabar*. Since β-HgS has an inverted level order at the Γ point [111], its $\mathcal{Z}_2$ invariant is nontrivial. The band inversion comes from the split-off spin-orbit s-orbiral bands (Γ_7) and the s-band (Γ_6) which is far below the Fermi level. The p-orbtials valence bands (Γ_8) do not participate in the level crossing and act as "parasitic" bands in this material. By neglecting the Γ_8 bands, we can easily calculate the MCN by using the effective Hamiltonian for the Γ_6 and Γ_7 bands. Going into the mirror planes by setting e.g. $k_z = 0$ we get a block structure of the Hamiltonian with

$$\mathcal{H}_{+i} = \begin{pmatrix} E_0 + B\gamma_0 k_\parallel^2 & -\frac{1}{\sqrt{3}} P k_- \\ . & -\Delta_0 - B\gamma_1 k_\parallel^2 \end{pmatrix}, \tag{6.73}$$

where $k_\parallel^2 = k_x^2 + k_y^2$, $P > 0$ and $\gamma_{0,1} > 0$. We find a MCN $\nu_{+i} = -1$ for $\Delta_0 + E_0 < 0$. Our results are in agreement with Ref. [112] which states that strained HgTe and β-HgS can have opposite MCNs.

The MCNs at the [100], [010] and [001] planes allow us to define *pseudospin* textures [104, 113] of the topological surface states in mercury chalcogenides. At the [001] surface, for instance, the projection of the unbroken mirror planes [100], [010] define two mirror invariant lines where the surface states can be classified according to their mirror eigenvalues. Using that the mirror operators can be brought in the form $M_i = -i\mu_i$ with Pauli matrices μ_i, the effective two-dimensional Hamiltonian of the surface states can be then written as

$$H_{eff} = E_{DP}\mathbb{1}_{2\times 2} + v_F^x \mu_y k_x - v_F^y \mu_x k_y, \tag{6.74}$$

where the degeneracy at the surface BZ center is guaranteed by TR symmetry. The MCNs determine the sign of the Fermi velocities, *i.e.* $\text{sign}(v^{x/y}) = \nu_{M_{y/x}}$. The convention is discussed in appendix B. The topological surface states can be then characterized by pseudospin textures which are directly related to the MCNs and realize a vortex structure in momentum space. Hence they can be characterized topologically by the winding number

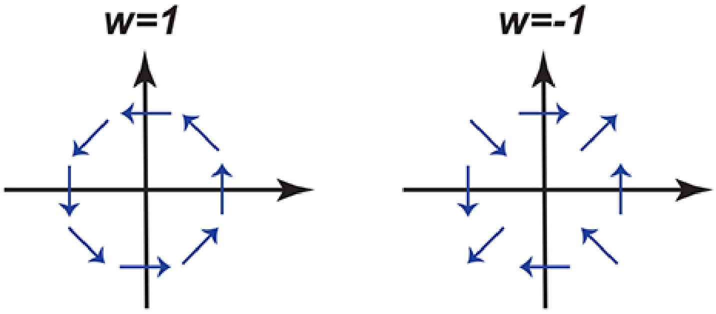

Figure 6.7: The topologically distinct pseudospin textures.

(the topological charge of the vortex) of the planar unit pseudospin. Writing the surface state Hamiltonian in the form $H_{eff} = h_x(k_x, k_y)\sigma_x + h_y(k_x, k_y)\sigma_y$, the winding number is defined as

$$w = \frac{1}{2\pi} \oint_{\mathcal{C}} d\mathbf{k} \cdot \nabla \Im(n_x + i n_y) \text{ with } (n_x, n_y) = (h_x, h_y)/\sqrt{h_x^2 + h_y^2}, \tag{6.75}$$

where $\mathcal{C}$ is a closed loop in momentum space encircling the essential degeneracy point. The two winding numbers $w = \pm 1$, corresponding to the pseudospin textures shown in Fig. 6.7, are equally compatible and the specific value is directly determined by the value of the MCNs. We remark that at opposite surfaces the sign of both two Fermi velocities are flipped. This changes the *helicity* of the pseudospin texture but still preserves the pseudospin texture winding number $w = \text{sign}(v_F^x \times v_F^y)$.

The pseudospin textures of the topological surface states have a close relation to the physical spin textures. At the surface mirror invariant lines the spin, and the total angular momentum of topological surface states have to be either *parallel* or *anti-parallel* to the pseudospin. For SmB_6, the physical spin was found to be always parallel to the pseudospin, and thus the knowledge of the MCNs provides a robust classification of the topological surface state spin [113]. However, for HgTe the angular momentum, as well as the spin operators of the $\Gamma_{6,8}$ bands have both positive and negative eigenvalues, and thus the relation between the pseudospin and the physical spin depends on the orbital composition of the surface states.

Before analyzing the results for the (pseudo)spin textures realized in strained HgTe, we emphasize that the broken inversion symmetry of the zincblende crystal structure can lead to a more complicated form of the effective two-dimensional Hamiltonian for the surface states. This occurs at the side surfaces of strained HgTe where the system possesses only TR symmetry and a twofold rotation symmetry: $\{2_{[100]}|0\}$, $\{2_{[010]}|0\}$ and $\{2_{[001]}|0\}$. We have performed a two-dimensional $\mathbf{k} \cdot \mathbf{p}$ analysis from which the functional form of the topological surface states can be derived to be

$$H_{eff}^{(001)} = E_{DP}\mathbb{1}_{2\times 2} + \tilde{v}_F^x \sigma_y (k_x + \alpha k_y) - \tilde{v}_F^y \sigma_x (\beta k_x + k_y). \tag{6.76}$$

Here we have considered the total angular momentum $J_z = \pm 1/2$ as a natural basis for the surface Kramer doublet sitting at the surface BZ center [114], and used that the form of the Hamiltonian must be invariant under the twofold rotational symmetry operator as $C_2^{[001]} = -i\sigma_z$ and the TR symmetry operator as $\mathcal{T} = i\sigma_y \mathcal{K}$. From the equation above, we see that the parameters α and β allow for a distortion of the spin textures with respect to those encountered in presence of mirror symmetries, but still yield a completely planar structure that can be topologically characterized by the physical spin winding number w.

6.7 Inversion symmetric results

We first start to present the results for the (pseudo)spin textures by neglecting the broken inversion symmetry of the zincblende crystal structure. The computation of the MCNs leads to the pseudospin textures shown in Fig. 6.8(a). Without loss of generality, we chose the uniaxial strain along the $\hat{x}$ direction. At the main [100] surface, the pseudospin texture exhibits an helical structure with a left-handed helicity for the surface state conduction band, and a right-handed one for the valence band, in perfect agreement with *density functional theory studies* [112, 100]. At the side surfaces ([010] and [001]) the different values of the two mirror Chern numbers for the mirror invariant planes yields a pseudospin texture with an opposite winding number $w = -1$.

To derive the physical spin textures we proceed as follows: we first establish the electronic characteristic of the surface Kramer's doublet at the main and side surfaces by solving the $\mathbf{k} \cdot \mathbf{p}$ model at the surface BZ center in the half-infinite space $x, y, z > 0$ respectively and then make use of first order perturbation at different momenta. The general method is outlined in Ref. [94]. The $\mathbf{k} \cdot \mathbf{p}$ parameters are based on the $T = 0$ band structure of pristine HgTe [47] and are listed in appendix C.

The results for the electronic characteristic of the DP at the side and the main surfaces are presented in Fig. 6.9. Panel (a) shows the behavior of the surface DP energy E_{DP} as a function of the uniaxial strain magnitude $\Delta\varepsilon$ along x. At the main surface, the Kramer's doublet is buried within the HH valence band, while on the two other side surfaces it resides in the indirect bulk gap of the system. This termination dependence is also reflected in the behavior of the decay length of the surface states shown in Fig. 6.9 (b). The side surfaces are characterized by a diverging decay length in the $\Delta\varepsilon \to 0$ limit, which implies that

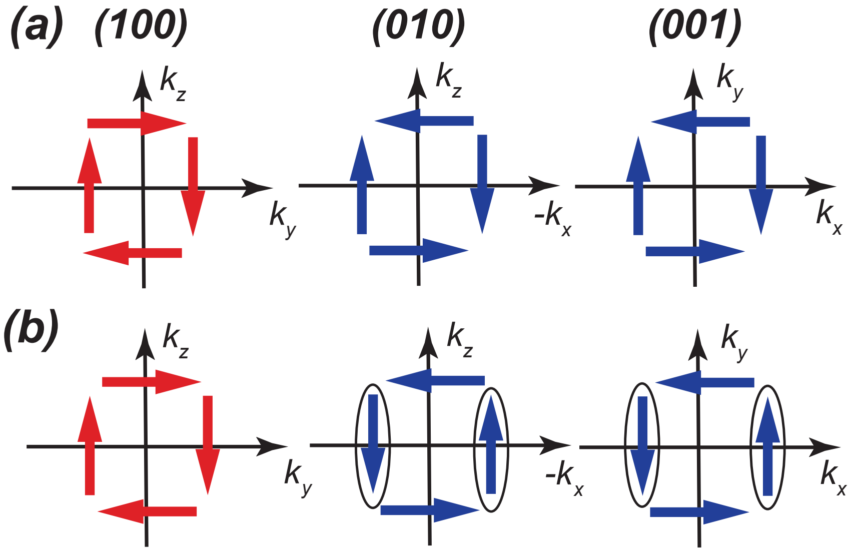

Figure 6.8: (a) Pseudospin textures for the Dirac cone of HgTe in presence of an uniaxial strain along the (100) direction at the (100), (010) and (001) crystal planes (from left to right). (b) Physical spin textures for strain smaller than the critical one $\Delta\varepsilon < \varepsilon_c$. For larger strain the physical spin textures corresponds to the pseudospin ones. Red indicates the main surface while blue represents the side surface patterns. The black circle marks the spin configuration which flips sign.

these surface states penetrate more deeply into the bulk as compared to the main surface. This different behavior can be attributed to the different nature of the wavefunction at the surface BZ center. At the main surface, the surface state Dirac wavefunction is all made of LH and Γ_6 states. An uniaxial strain along the $\hat{x}$ direction preserves the axial rotation symmetry in the plane and the total angular momentum J_x is a good quantum number [71, 94]. This implies the absence of any mixing between the HH states ($|3/2, J_x = \pm 3/2\rangle$) and the LH ($|3/2, J_x = \pm 1/2\rangle$). This is verified in the effective Hamiltonian (6.71), which can be written as

$$\mathcal{H}^{[100]}_{+i}(k_y = 0) \simeq \begin{pmatrix} E_0 + B\gamma_0 k_x^2 & \sqrt{\frac{2}{3}} P k_x & 0 \\ . & -B(\gamma_1 + 2\bar{\gamma})k_x^2 + \Delta\varepsilon & 0 \\ . & . & -B(\gamma_1 - 2\bar{\gamma})k_x^2 - \Delta\varepsilon \end{pmatrix} \tag{6.77}$$

in the basis $|1/2, J_x = +1/2\rangle$ (Γ_6), $|3/2, J_x = +1/2\rangle$ (LH) and $|3/2, J_x = +3/2\rangle$ (HH). At these surfaces the HH bands play the role of a *parasitic* band [94] and the surface Kramer's doublet results from the reduced model describing an artificial LH-Γ_6 TI. The DP energy

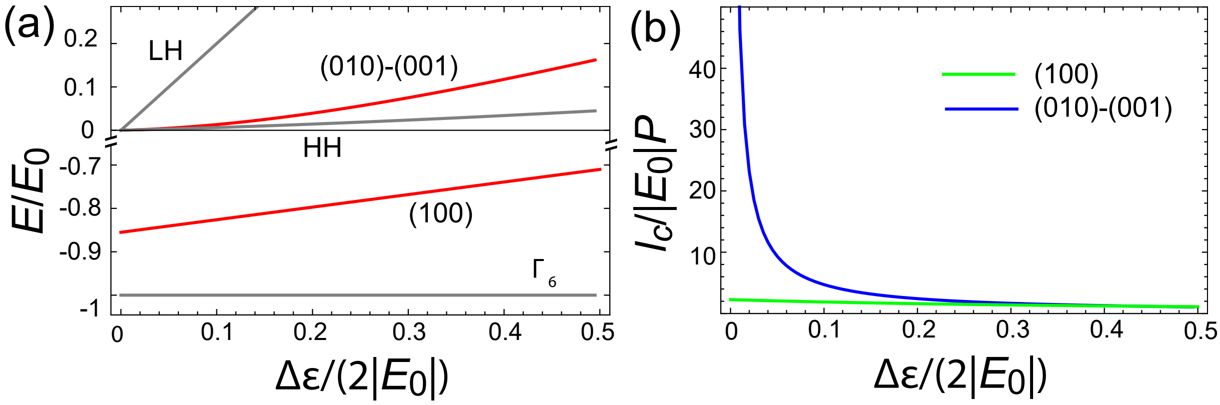

Figure 6.9: Behavior of the surface DP (a) and its decay length (b) in strained HgTe along [100] as a function of the strain magnitude $\Delta\varepsilon > 0$ at the (100),(010), and (001) surfaces (red lines). The gray lines correspond to the conduction, valence and the Γ_6 band edge. At the (100) surface, the surface DP is buried within the HH valence band but resides in the bandgap of the LH-Γ_6 TI bulk.

in Fig. 6.9 at this surface is thus given by

$$E_{DP} = \frac{E_0(\gamma_1 + 2\gamma_2) + \gamma_0\Delta\varepsilon}{\gamma_0 + \gamma_1 + 2\gamma_2}. \tag{6.78}$$

This does not hold true at the side surfaces where the uniaxial strain breaks the in-plane rotation symmetry, thereby leading to an effective hybridization between the LH and the HH states. The surface Dirac wavefunction becoming a superposition of $\Gamma_{6,8}$ bands is then pushed out of the HH bulk bandwidth [115] and remerges in the full bandgap of the system, in agreement with the features encountered in the *Fano model* [116].

Before studying the spin textures, let us analyze the Fermi velocities of the surface Dirac cones. In Fig. 6.10 (a) we show the behavior of the magnitude of the Fermi velocities $|v_F^i|$ as a function of the strain magnitude $\Delta\varepsilon$. We find that for the Dirac cone at the main surface, the two Fermi velocities $v_F^{y/z}$ have equal magnitudes. Therefore, the topological surface states display a global $U(1)$ rotational symmetry similarly to the case of, for instance, Bi_2Se_3 [114]. The expression for the Fermi velocity is given by

$$v_F^{y/z} = \frac{1}{2}\sqrt{\frac{2}{3}}P\sqrt{1 - \frac{(\gamma_0 - (\gamma_1 + 2\bar{\gamma}))^2}{(\gamma_0 + (\gamma_1 + 2\bar{\gamma}))^2}}. \tag{6.79}$$

The two-dimensional $\mathbf{k}\cdot\mathbf{p}$ analysis of Ref. [94] explicitly shows that this is an immediate consequence of the fourfold rotational symmetry along the $\hat{x}$ axis. At the side surfaces the strain lowers the surface point group symmetry from $\mathcal{C}_{4v}$ to $\mathcal{C}_{2v}$. This explains the

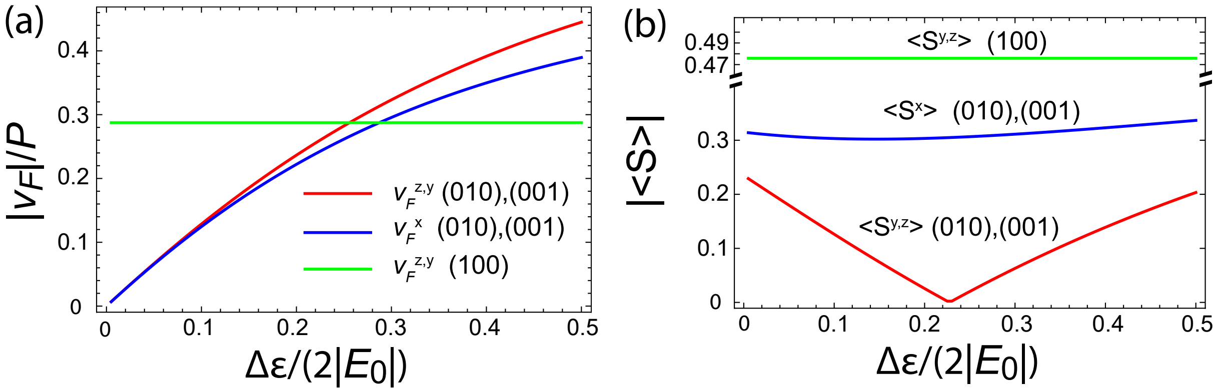

Figure 6.10: Behavior of the magnitudes of the Fermi velocities $|v_F|$ (a) and its spin composition (b) in the topological surface states of strained HgTe as a function of the strain magnitude $\Delta\varepsilon$ along x. The Dirac cone at the side surfaces ((010) and (001)) exhibit an anisotropic behavior in the Fermi velocity and spin composition since the uniaxial strain lower the point group symmetry.

anisotropy seen in Fig. 6.10 (a).

We find that a similar anisotropy appears also by evaluating the spin operator eigenvalues along the mirror invariant lines at the side surfaces plotted in Fig. 6.10 (b). It then follows that the physical spin is always parallel to the pseudospin except at the $k_z = 0$ and $k_y = 0$ mirror invariant lines for the side surfaces (010) and (001) respectively. At these mirror invariant lines, the physical spin is *antiparallel* to the pseudospin below a critical strain magnitude ε_c, and *parallel* for large enough strain. This implies that contrary to the pseudospin textures at the (010) and (001) surface terminations characterized by a $w = -1$ winding number independent of the strain magnitude, the physical spin textures exhibit a right-handed $w = 1$ helical structure for small strain. This is shown in Fig. 6.10 (b). The spin textures are only equal to the pseudospin textures for a large enough strain value.

To gain more insight into this *spin texture topological phase transition*, we computed the orbital resolved projected spin eigenvalue

$$\langle \mathbf{S} \rangle = \langle \mathbf{S}^{\Gamma_6} \rangle + \langle \mathbf{S}^{LH} \rangle + \langle \mathbf{S}^{HH} \rangle \tag{6.80}$$

of the topological surface states along the mirror invariant lines $k_{y,z} = 0$ for the (001) and (010) surface terminations respectively. The ensuing behavior as a function of the strain magnitude is shown in Fig. 6.11 For small strain, the helical edge states has a predominant LH orbital character, which implies that the physical spin is *anti-parallel* to the pseudospin. By continuously increasing the strain magnitude, the surface states starts to acquire a sizeable Γ_6 and HH character which ultimately reverse the spin direction to

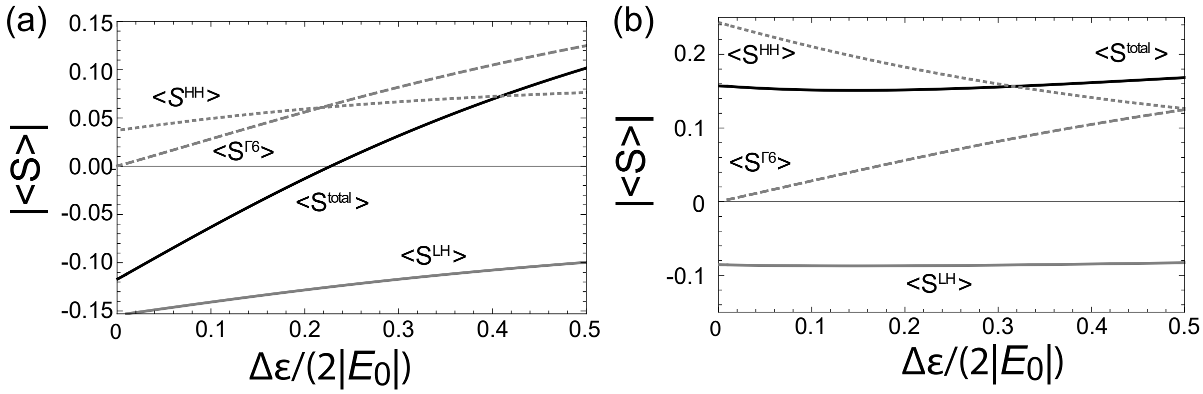

Figure 6.11: Orbital resolved (grey lines) and total spin (black line) of the Dirac cone for the (010) [(001)] plane at the mirror invariant line $k_z = 0$ [$k_y = 0$] (a) and $k_x = 0$ (b). For small strain, the physical spin plotted in (a) is antiparallel to the pseudospin, while for large strain they are parallel. Along the other direction (b) we find no spin-flip.

be *parallel* to the pseudospin.

To understand how the spin texture reverses its winding number, we show the schematic spin structure of the Dirac cone close to the critical strain in Fig. 6.12 for the conduction band ($E > E_{DP}$). At the critical strain value ε_c, the spin expectation value vanishes at two TR related momenta on the $k_y = 0$ line for the (001) plane and the $k_z = 0$ line for the (010) plane. For all other momenta, the spin expectation values are one-dimensional. This makes the reversal of the spin textures winding possible (cf. Fig. 6.8 (b)).

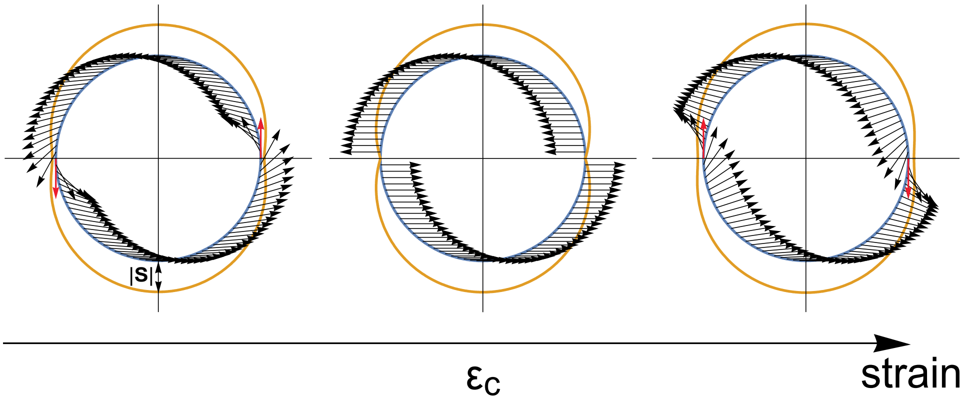

Figure 6.12: Schematic unit planar spin textures of the Dirac cone close to the critical strain ε_c for all in-plane momenta where we ignore the ellipticity of the Dirac cone dispersion of the conduction band. The radial difference between the blue and the orange line is a measure for the absolute value of the spin. The red-marked spins are the spins which flip sign.

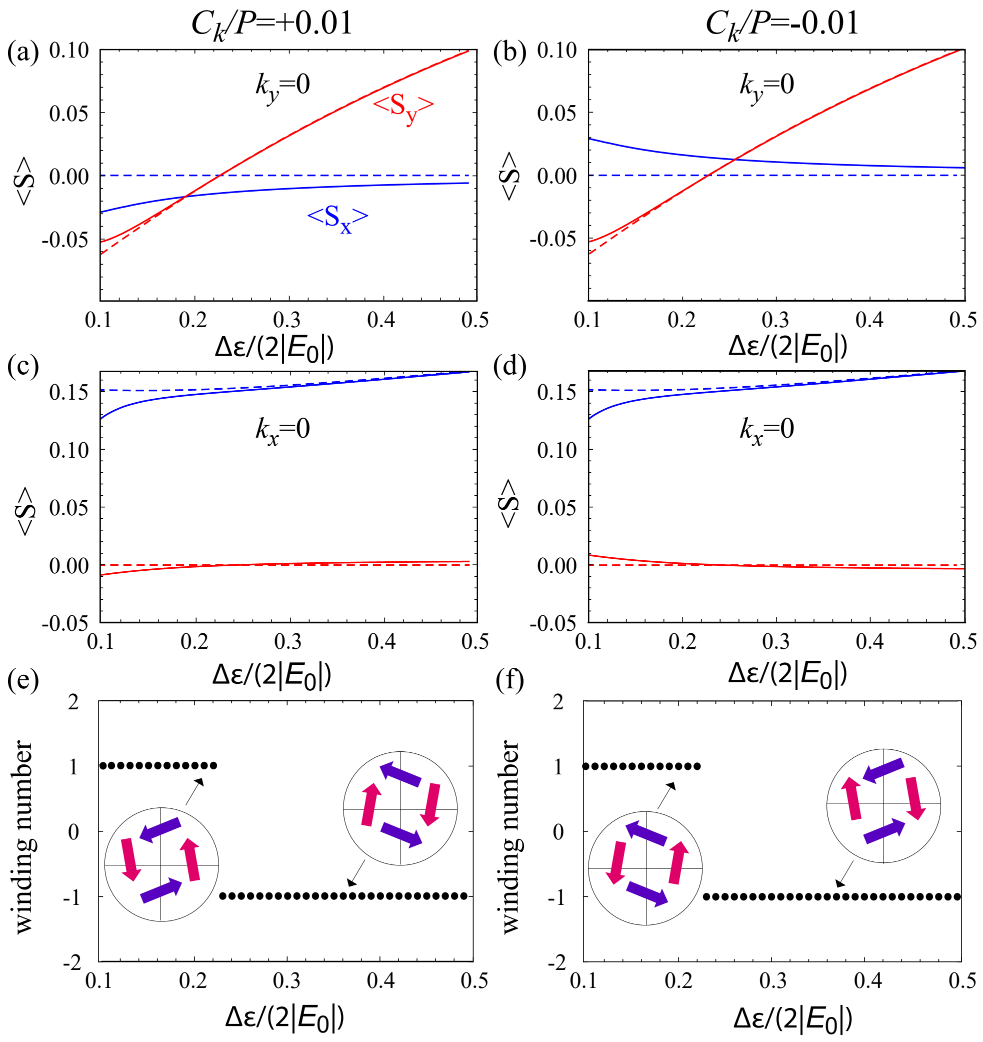

Figure 6.13: Spin values of the side surface Dirac cone for two BIA parameters $C_k/P = \pm 0.01$ (thick lines) for $k_y = 0$, $k_x < 0$ (a,b), and $k_x = 0$, $k_y < 0$ (c,d). The dashed lines correspond to the inversion-symmetric solution. At (e) and (f) we explicitly calculated the winding number and show in the inset the corresponding real spin pattern.

6.8 Robust spin-flip transition at the side surfaces

The characteristics of the surface states at the side surfaces are not endangered by small perturbations destroying the mirror symmetries. We explicitly show this by taking into account the bulk inversion asymmetry (BIA) of the real zincblende crystal structure. This reduces the point group symmetry to the tetrahedral group T_d and the mirror Chern numbers at the side surfaces are not well-defined. This also means that the spin textures of the surface states cannot be directly inferred from the mirror Chern number discussed above. We have additional linear terms in $k_{x/y}$ going with the elementary parameter C_k

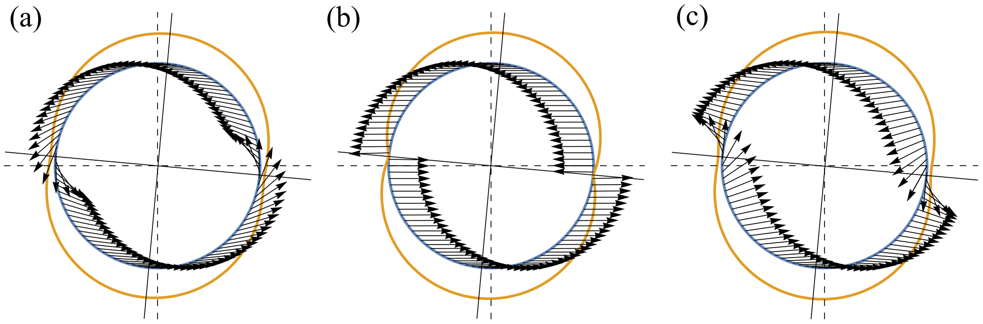

Figure 6.14: Unit planar spin textures equivalent to Fig. 6.12 with $C_k/P = 0.01$ for $\Delta\varepsilon < \varepsilon_c(C_k)$ (a), $\Delta\varepsilon = \varepsilon_c(C_k)$ (b) and $\Delta\varepsilon > \varepsilon_c(C_k)$ (c).

of the Kane model mixing both mirror channels.

The spin textures can be still topologically characterized by their winding number since yet they realize a planar vortex structure in momentum space as we explained above. Although the symmetry argument allows a distortion of the spin textures the corresponding topological phase transition is not endangered.

We can solve the Kane model Hamiltonian with the linear BIA terms in the half-infinite space $z > 0$ for strain along x. The eigenstates along $k_{x/y} > 0$ for $k_{y/x} = 0$ corresponding to the eigenvalues with positive slope are a mixture of both mirror blocks.

Our results are represented in Fig. 6.13. It shows the spin components of the topological surface states at the $k_{x/y} = 0$ lines as a function of the strain magnitude at two representative values of the BIA parameter C_k. The spin expectation value ceases to be orthogonal to these lines acquiring a finite component parallel to them. However, as found earlier, only one predominant spin component drives the phase transition and switches the sign of the winding number at a critical strain $\varepsilon_c(C_k)$. The spin expectation value vanishes at two TR related momenta which are now slightly shifted from $k_y = 0$ and $k_z = 0$ respectively. Fig. 6.14 shows the evolution of the spin textures close to the critical strain value, which is very similar to the one encountered in the absence of inversion symmetry breaking perturbations (cf. Fig. 6.12).

The winding number of the spin textures is unaltered if we add a small perturbation given by the linear BIA term. This allows us still to distinguish two different phases of the strong TI phase at the side surfaces for different strain values. One phase is characterized by the topological invariant $w = +1$ and the other one by $w = -1$. We have therefore verified that the occurrence of the spin winding number flip is a generic feature independent of the BIA parameter value. The corresponding phase diagram is shown in Fig. 6.15.

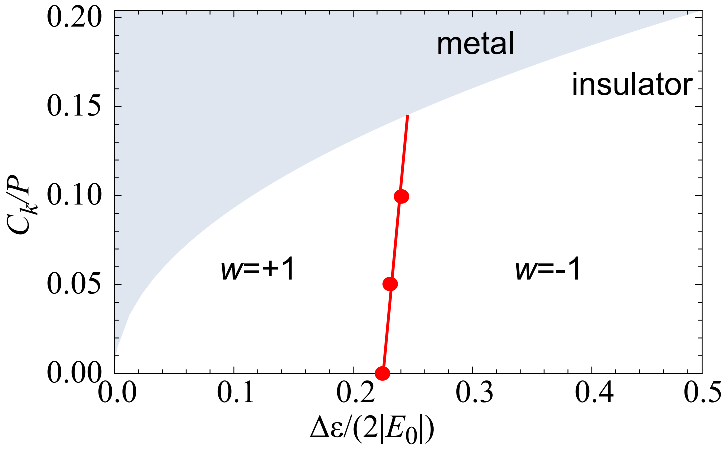

Figure 6.15: Phase diagram of the side surface physics for finite BIA parameter C_k. The non-trivial insulating phase can be distinguished into two different topological phases coming from the Dirac cone spin texture.

6.9 Crucial boundary dependence on the main surface

We now show that the electronic characteristics of the topological surface states at the main surfaces are more susceptible to inversion-symmetry breaking perturbations. This is due to the fact that, as we have shown previously, the DP is embedded in the bulk of the HH band but still completely decoupled if inversion symmetry is preserved. Allowing for the BIA terms in the $\mathbf{k}\cdot\mathbf{p}$ theory, the DP is no longer decoupled from the HH band, and opens an effective hybridization channel between the surface states and the bulk states.
For enough small hybridization, we could expect that the original DP leads to a residual surface/ghost resonance [115] in the bulk states, similarly to the *Fano model* [116]. Alternatively, there could be a catapult-like effect: the hybridization of the buried topological surface states with the parasitic bulk bands leads to the tendency of the surface states to be pushed away from overlapping in energy and momentum with the bulk states.
To discriminate between these two mechanisms, we divide the Kane Hamiltonian in two TR channels at $k_x = k_y = 0$ assuming a uniaxial strain along the z direction. We can then bring the Hamiltonian in the block form

$$H(k_x = 0, k_y = 0, k_z \to -i\partial_z) \simeq \begin{pmatrix} \mathcal{H}_+(-i\partial_z) & 0 \\ \cdot & \mathcal{H}_-(-i\partial_z), \end{pmatrix} \tag{6.81}$$

with

$$\mathcal{H}_+(k_z) = \begin{pmatrix} E_0 + B\gamma_0 k_z^2 & \sqrt{\frac{2}{3}} P k_z & 0 \\ . & \Delta\varepsilon - B(\gamma_1 + 2\bar{\gamma}_2) k_z^2 & -C_k k_z \\ . & . & -\Delta\varepsilon - B(\gamma_1 - 2\bar{\gamma}_2) k_z^2 \end{pmatrix}. \tag{6.82}$$

Studying the $\mathbf{k}\cdot\mathbf{p}$ Hamiltonian of Eq. (6.82) for the half-line $z > 0$ with the techniques used many times before in the thesis, we find the absence of a localized surface states for small strain as long as we take into account fixed boundary conditions (FBC). A surface Kramer's doublet only appears at an enough large value of strain above which the contribution of the bulk HH bands is nearly negligible. The critical strain at which surface states appear is given in terms of Luttinger parameters by

$$\Delta\varepsilon_{crit}(C_k) \approx \frac{(\gamma_1 - 2\bar{\gamma})(\gamma_1 + 2\bar{\gamma})|E_0| - \gamma_0 C_k^2}{(\gamma_1 - 2\bar{\gamma})\,(2\gamma_0 + \gamma_1 + 2\bar{\gamma})}. \tag{6.83}$$

The critical strain value at which the surface Kramer's doublet appears is marked with a black dot in Fig. 6.16 (b). We can interpret this point as a phase transition point separating the parameter space region where the topological surface states possess a DP from a region where the DP of the surface states is absent. In Fig. 6.16 (c) we also show the inverse decay length l_c^{-1} characterizing the exponential behavior of the DP as an indicator for the critical behavior of the system. Going from high strain to the low strain limit the decay length is diverging using FBC. This analysis shows that there can exist TI materials where the topological surface states do not have a surface DP. We emphasize that this feature is not in contradiction with the non-trivial $\mathbb{Z}_2$ topological invariant of the system: the non-trivial topology of a three-dimensional topological insulator implies the presence of surface states connecting valence to conduction bands, and does not predict the existence of a surface Kramers doublet.

We proceed further and use another boundary condition (BC). For the checkerboard and the BHZ model we showed that the choice of the two most common BCs had no effect on the existence of surface states. We now check whether we find a similar behavior for the Kane model of strained HgTe changing the BC. Surprisingly, assuming natural boundary condition (NBC) we find a DP solution in the bulk band gap independent of the strain magnitude $\Delta\varepsilon > 0$. Using NBC, the DP energy has a discontinuity switching on the inversion-symmetry breaking parameter C_k: for every finite value of it, the DP jumps out of the bulk states (HH) (see Fig. 6.16 (c)). The energy distance between the HH band edge and DP energy increases with the hybridization parameter. Henceforth the DP is located very close to the HH band edge for realistic values of C_k but never touches it. This is also

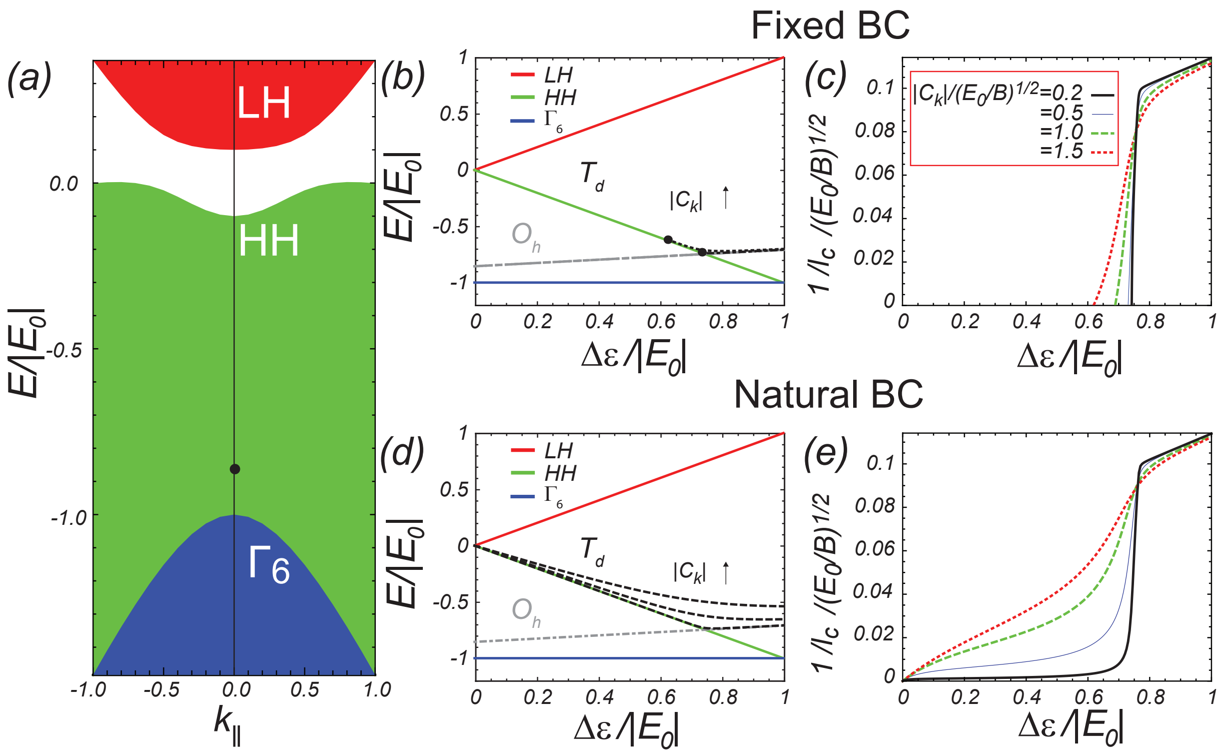

Figure 6.16: The DP is plotted over the strain with FBC (b) and NBC (d) for different values of artificially large C_k. The plotted band edges of the LH, HH and Γ_6 are the one at the BZ center because they are the one which determine the existence of those edge states. In the plots (c) and (e) we show the corresponding decay lengths. The red box shows the chosen parameters set. Panel (a) shows the main surface and the DP.

demonstrated by the fact that the decay length is always finite, independent of the strain magnitude and the actual value of C_k (see Fig. 6.16 (d)).

The behavior in the high strain limit is however equal for both BCs. If we increase the strain the solutions with NBC and FBC merge together and collapse onto the DP energy found in the system with bulk inversion symmetry. In conclusion we can state that there is a fundamental difference in the two commonly used BCs.

7 Summary and outlook

In topological states of matter a global invariant of the bulk theory gives a physical response if one adds to the system a surface or an edge. These surface physical properties can be well described by local long-wavelength theories, such as a Dirac equation. In other words, the global topological property of the bulk has a direct counterpart in a local effect at the boundaries. This dichotomy of local and global properties can be lifted if the bulk theory itself is not global. This seems to be counterintuitive but we have provided in this thesis examples where a long-wavelength continuum theory can be topologically well defined in the bulk and also predict the correct surface properties. In particular, we showed that although the basis manifold of any generic continuum theory does not allow for topologically non-trivial mappings – it corresponds to the real momentum space – there exist loopholes which allows for a proper definition of topological invariants.

We identified two different classes of these topological $\mathbf{k}\cdot\mathbf{p}$ Hamiltonians for Chern insulators. In the first class the basis manifold can be made isomorphic to a sphere. With this one-point compactification, the topological invariants can be defined in the same way as they are defined on a torus, which is the basis manifold (the Brillouin zone) of a lattice Hamiltonian. We also defined another class where the basis manifold is isomorphic to a hemisphere. This is a non-compact manifold with no analog to lattice models. Nevertheless, we showed that even in this case one can still obtain the correct topological properties both in the bulk and on the surfaces. This is a remarkable result showing that the one-point compact models are not the only ones which play a role in the study of topological $\mathbf{k}\cdot\mathbf{p}$ Hamiltonians. The fundamental difference between spherical Chern insulators and hemispherical Chern insulators is that for the latter ingap edge states generally occur far away from the low-energy expansion point.

With this knowledge, we have thereby analyzed the continuum theory of real materials with non-trivial topological properties and concentrated on HgTe. Using the well-known $\mathbf{k}\cdot\mathbf{p}$ Kane model, we analyzed in this work the surface state properties at the different surfaces of this material. Using the fact that the low-energy theory has mirror symmetries, we could identify pseudospin and spin textures of the topological surface states at the material surfaces. The most important result of our study is that at surfaces with symmetry lower than $\mathcal{C}_{2v}$ it exists a strain-driven topological phase transition in the surface state spin textures. In addition, this topological phase transition is stable against inversion symmetry breaking perturbations. Finally we showed that at the highest symmetry surfaces, the existence of a surface Kramer doublet depends sensitively on the boundary conditions. This feature, however, does not contradict the bulk-edge correspondence of strained HgTe. For future work, it would be interesting to study from this low-energy continuum theory perspective, other topological states of matter such as topological semimetals.

A Pauli, Gellmann and Dirac matrices

For a lot of effective models we need an approximate description of internal degrees of freedom like the spin $\hat{\mathbf{S}}$, the sublattice A/B or the total angular momentum $\hat{\mathbf{J}}$.

The eigenvectors which can be realized in these N-component Hamiltonians H are related to each other by an unitary operation V acting like $V^\dagger H V$. The $U(1)$ part of this transformation V defines an equivalence class so that we have to consider the $SU(N)$ only. The generators of this group can be used to describe the Hamiltonian H and its eigenvectors.

Let us start with the simplest Hamiltonian with one internal degree of freedom: the two-band Hamiltonian ($N = 2$). The special unitary group

$$SU(2) = \{\exp(-i\boldsymbol{\alpha} \cdot \boldsymbol{\sigma}/2) | \boldsymbol{\alpha} \in \mathbb{R}^3\}, \tag{A.1}$$

where $\boldsymbol{\sigma} = (\sigma_x, \sigma_y, \sigma_z)$ is a vector of three hermitian 2×2 matrices. These *generators* are called *Pauli matrices* and they can be represented by

$$\sigma_x = \begin{pmatrix} 0 & 1 \\ 1 & 0 \end{pmatrix}, \ \sigma_y = \begin{pmatrix} 0 & -i \\ i & 0 \end{pmatrix} \text{ and } \sigma_z = \begin{pmatrix} 1 & 0 \\ 0 & -1 \end{pmatrix}. \tag{A.2}$$

They can be also written with the letter τ or with Arabic numbers instead of the three coordinate labels. However these Pauli matrices are quite helpful to describe the 2×2 Hamiltonians. The hermitian structure fixes all Hamiltonians to be of the form

$$H(d_0, \mathbf{d}) = d_0 \sigma_0 + \mathbf{d} \cdot \boldsymbol{\sigma} \text{ with } \mathbf{d} \in \mathbb{R}^3, d_0 \in \mathbb{R}, \tag{A.3}$$

where $\sigma_0 = \mathbb{1}_{2\times 2}$. The topological relevant part of the Hamiltonian is simply encoded in the real vector $\mathbf{d}$. A non-zero vector gives us a possibility to clearly distinguish the two bands or levels with the energy $E_\pm = d_0 \pm \sqrt{\mathbf{d} \cdot \mathbf{d}}$. One can go even further. The corresponding *projector* for each band/level $|\pm\rangle$ is given by $P_\pm = \left(\mathbb{1}_{2\times 2} \pm \hat{\mathbf{d}} \cdot \boldsymbol{\sigma}\right)/2$ where $\hat{\mathbf{d}} = \mathbf{d}/|\mathbf{d}|$ is normalized. This shows us that the ground state of every insulating 2×2 Hamiltonian can be represented by a point living on a sphere $\mathbb{S}^2$.

If we want to describe three level quantum systems ($N = 3$) we have to extend this idea by going to the Lie group $SU(3)$ where we have to substitute the three generators σ_i in Eq. (A.1) by eight matrices λ_i. A comprehensive analysis of the pattern of geometric phases arising in those unitary representations of this group is represented in Ref. [109]. The parameter $\boldsymbol{\alpha}$ have to live then in $\mathbb{R}^8$. They are the *Gell-Mann matrices* which can be written as

$$\begin{aligned}
\lambda_1 &= \begin{pmatrix} 0 & 1 & 0 \\ 1 & 0 & 0 \\ 0 & 0 & 0 \end{pmatrix}, \ \lambda_2 = \begin{pmatrix} 0 & -i & 0 \\ i & 0 & 0 \\ 0 & 0 & 0 \end{pmatrix}, \ \lambda_3 = \begin{pmatrix} 1 & 0 & 0 \\ 0 & -1 & 0 \\ 0 & 0 & 0 \end{pmatrix}, \\
\lambda_4 &= \begin{pmatrix} 0 & 0 & 1 \\ 0 & 0 & 0 \\ 1 & 0 & 0 \end{pmatrix}, \ \lambda_5 = \begin{pmatrix} 0 & 0 & -i \\ 0 & 0 & 0 \\ i & 0 & 0 \end{pmatrix}, \\
\lambda_6 &= \begin{pmatrix} 0 & 0 & 0 \\ 0 & 0 & 1 \\ 0 & 1 & 0 \end{pmatrix}, \ \lambda_7 = \begin{pmatrix} 0 & 0 & 0 \\ 0 & 0 & -i \\ 0 & i & 0 \end{pmatrix} \text{ and } \lambda_8 = \begin{pmatrix} \frac{1}{\sqrt{3}} & 0 & 0 \\ 0 & \frac{1}{\sqrt{3}} & 0 \\ 0 & 0 & -\frac{2}{\sqrt{3}} \end{pmatrix}.
\end{aligned} \tag{A.4}$$

Every 3×3 Hamiltonian can be brought therefore in the form (A.3) like in the 2×2 case where we substitute $\sigma \to \lambda$ and define $\lambda_0 = \mathbb{1}_{3\times3}$. The vector $\mathbf{d}$ is then element of $\mathbb{R}^8$. In the 3×3 case it is not easy as in the 2×2 case to distinguish insulating and metallic phases. Following Ref. [110] the projectors for the bands $j = 1, 2, 3$ are given by

$$P_j = \frac{1}{3}(\mathbb{1}_{3\times3} + \sqrt{3}\mathbf{n}_j \cdot \boldsymbol{\lambda}), \tag{A.5}$$

with the vector

$$\mathbf{n}_j = \frac{1}{\gamma_j^2 - 1}(\gamma_j \hat{\mathbf{d}} + \hat{\mathbf{d}} * \hat{\mathbf{d}}) \tag{A.6}$$

and the angle

$$\gamma_j = 2\cos\left(\frac{1}{3}\arccos(\hat{\mathbf{d}} \cdot \hat{\mathbf{d}} * \hat{\mathbf{d}}) + \frac{2\pi}{3}j\right). \tag{A.7}$$

The *star product* $\mathbf{a} * \mathbf{b}$ is defined in Ref. [109]. The important property is that the vector $\mathbf{n}_j$ fulfills the condition $\mathbf{n}_j * \mathbf{n}_j = \mathbf{n}_j$ restricting the vector of $\mathbb{R}^8$ to live in a four-dimensional orbit of a $\mathbb{S}^7$ sphere which corresponds to an element of the *complex projective plane* $\mathbb{C}P^2$. This is the difference to the spherical character of the ground state in a two-level quantum systems.

Last but not least we want to consider the $SU(4)$ treatment which is used to characterize time-reversal invariant topological insulators as a minimal model. This is a four level quantum system. In $SU(4)$ we have 15 generators as 4×4 matrices. If we use the identity $\mathbb{1}_{4\times 4}$ and the two sets of *Dirac matrices*

$$\delta_i^{(1)} = \sigma_0 \otimes \sigma_i \text{ or } \delta_i^{(2)} = \sigma_i \otimes \sigma_0, \tag{A.8}$$

we can build up a new basis of hermitian and traceless generators next to the identity to describe 4×4 Hamiltonians with

$$\Gamma_{ij} = \delta_i^{(2)} \delta_j^{(1)} \tag{A.9}$$

for $i, j = 1, 2, 3$. Again only the coefficients in front of the 15 generators are relevant for topological issues. If we ask how we can define the projector of each band the problem becomes more complicated, because one has to solve a quartic equation instead of a cubic or quadratic one. This is not enlightening that is why we skip this here.
We want to remark that the original set of matrices used by Dirac to describe free fermions in spacetime $D = 1 + 3$ are given by $\alpha_0 = \Gamma_{00}$, $\alpha_1 = \Gamma_{11}$, $\alpha_2 = \Gamma_{12}$, $\alpha_3 = \Gamma_{13}$ and $\beta = \Gamma_{30}$.

B Conventions of the Chern number

In the study of Chern insulators one finds two different conventions how one can define the Chern number and the corresponding bulk-edge correspondence.

Let us fix therefore first the plane of the Chern system embedded in the physical three-dimensional space. We can use numbers $1, 2, 3$ to label the unit vectors of a Cartesian coordinate system which we can identify with the three directions x, y, z. Without loss of generality we assume that we can define a right-handed Cartesian coordinate system. By using the wedge product notation of differential forms we can identify the differential form $dk_1 \wedge dk_2 = dk_x \wedge dk_y$ with the plane. The two conventions of the Chern number $\nu_j^{(\pm)}$ are then defined like

$$\nu_j^{\pm} = \pm \frac{i}{2\pi} \int_{\mathcal{M}} \mathrm{Tr}(P_j \wedge dP_j \wedge dP_j) = \pm \int_{\mathcal{M}} dk_x \wedge dk_y \, \Omega_j(k_x, k_y), \tag{B.1}$$

where P_j is the projector of the band with index j, the field $\Omega_j(k_x, k_y)$ is the related Berry curvature and $\mathcal{M}$ is a two-dimensional manifold. There is a conceptional difference in the choice whether we use the positive or the negative sign in front. To understand this we have to add a boundary to the system. Again without loss of generality the line $x = 0$ separates two spaces. Assuming that on one side there is the vacuum with trivial topology we describe the edge with a *decay vector* η pointing in the half space not occupied by the vacuum. We can have two possibilities to define now an edge using the half-space treatment: either $\eta = \mathbf{e}_x$ $(x > 0)$ or $\eta = -\mathbf{e}_x$ $(x < 0)$. The difference gives a minus sign in the definition of the Chern number. An other point is that there are two different ways to look on the material – two viewing directions: either one is inside the non-trivial material and looks outwards or one looks on the material from the trivial outside. The decay vector is the same for both directions.

Let us assume that we have fixed $\eta = \mathbf{e}_x$ so that its in-plane orthogonal partner of the right-handed system (here: k_y) defines the *propagation direction* of possible edge modes with a positive Fermi velocity. Looking from inside out we have to take the definition ν^+. The sign of the Fermi velocity is then directly related to sign of the Chern number and the absolute value of the Chern number tells us how many chiral edge states are there.

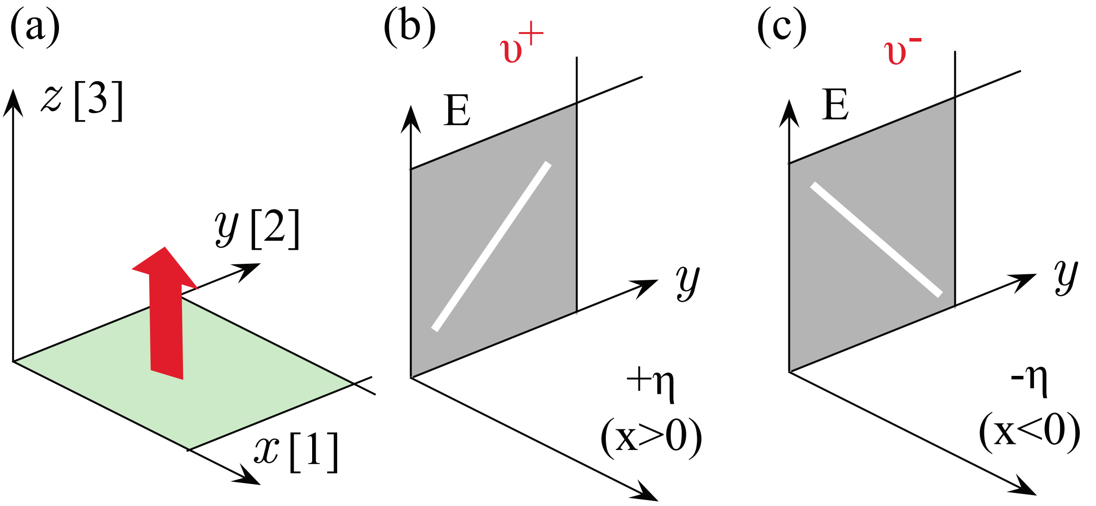

Figure B.1: The setting is shown in (a) which leads to different descriptions of the edge spectrum corresponding to two different conventions (b) and (c) of the Chern number.

The energy is the third part of the tripod. If we look instead on the material from the outside, the η points in the opposite direction. To cancel the additional minus sign it is more convenient to use the definition ν^{-}. The different conventions are also illustrated in Fig. (B.1).

If we make a cyclic permutation of the defined system we can reach all other relevant configurations where we have switched the boundary from $x > 0$ to $x < 0$ or choose an other definition of the plane.

C The extended Kane model

To describe quantum systems with a zinc-blende structure (point group T_d) like the textbook TI HgTe or some ternary Heusler compounds [117], which have a qualitatively similar band structure and low-energy excitations close to the Γ-point, we can use the *extended Kane model* [84]. The zincblende structure (Tab. C.1) has a tetrahedral coordination – two atom types form two interpenetrating face-centered cubic (fcc) lattices. A special structure is the diamond structure where we have only one type of atoms so that we have an additional inversion symmetry. Its crystallographic point group is denoted by O_h.

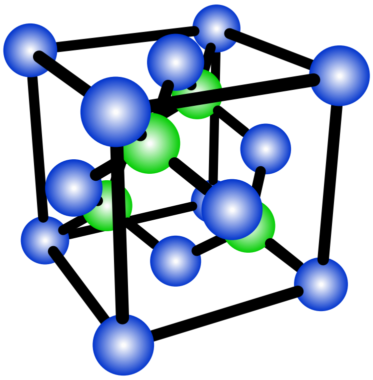

Figure C.1: The zinc-blende structure is shown. Blue and green spheres correspond to two different sorts of atoms/elements.

The underlying idea of the extended Kane model is based on the invariant expansion of a multi-band Hamiltonian in the point group T_d. Analyzing its *double-group representations* (see Tab. C.1) one find three building blocks which are denoted Γ_6, Γ_7 and Γ_8 representing spin-full fermions. While the first two have a two-component representation based on spin $j = 1/2$, Γ_8 has four components which are based on spin $j = 3/2$ fermions. The spin-orbit interaction gives rise to this description with new quantum numbers which are related to the eigenvalues of the total angular momentum $\hat{\mathbf{J}}^2 = (\hat{\mathbf{L}} + \hat{\mathbf{S}})^2$ which is the sum of the angular momentum and spin.

There exist now a lot of different possibilities to create an effective Hamiltonian by including more and more valence and conduction bands by combining an arbitrary number of these irreducible representations $\Gamma_{6,7,8}$ to describe the physics close to Brillouin zone center

Table C.1: Character table for the double group T_d with the notation $(\bar{\cdot})$ for the rotation by 2π, $S_n = C_n \otimes i$ where C_n is the n-fold rotation and i is the inversion, and σ_d for the reflection in a diagonal plane. This table is adapted form Ref. [105] and Ref. [118].

	E	$\bar{E}$	$8C_3$	$8\bar{C}_3$	$3C_2$, $3\bar{C}_2$	$6S_4$	$6\bar{S}_4$	$6\sigma_d$, $6\bar{\sigma}_d$
Γ_1	$+1$	$+1$	$+1$	$+1$	$+1$	$+1$	$+1$	$+1$
Γ_2	$+1$	$+1$	$+1$	$+1$	$+1$	-1	-1	-1
Γ_3	$+2$	$+2$	-1	-1	$+2$	±0	±0	±0
Γ_4	$+3$	$+3$	±0	±0	-1	$+1$	$+1$	-1
Γ_5	$+3$	$+3$	±0	±0	-1	-1	-1	$+1$
Γ_6	$+2$	-2	$+1$	-1	±0	$+\sqrt{2}$	$-\sqrt{2}$	±0
Γ_7	$+2$	-2	$+1$	-1	±0	$-\sqrt{2}$	$+\sqrt{2}$	±0
Γ_8	$+4$	-4	-1	$+1$	±0	±0	±0	±0

better and better. The accurate description [84] of the band-structure close to the fundamental gap is given by a 14×14 matrix including Γ_6^c, $\Gamma_7^{c/v}$ and $\Gamma_8^{c/v}$ where the superscripts c/v stand for the conduction and valence bands. Nevertheless, it is often convenient to consider smaller $\mathbf{k} \cdot \mathbf{p}$ models. In our work for HgTe we use the eight-band Kane model

$$\mathcal{H} = \begin{pmatrix} \mathcal{H}^{6c,6c} & \mathcal{H}^{6c,8v} & \mathcal{H}^{6c,7v} \\ \cdot & \mathcal{H}^{8v,8v} & \mathcal{H}^{8v,7v} \\ \cdot & \cdot & \mathcal{H}^{7v,7v} \end{pmatrix} \tag{C.1}$$

or the *Luttinger model* which is only the part $\mathcal{H}^{8v,8v}$. The superscript will be neglected from now on because there is no way for confusion. It is quite easy to see that there is a hierarchy of $\mathbf{k} \cdot \mathbf{p}$ Hamiltonians by successively reducing the size of matrices (*size hierarchy*). The effect of the ignored bands leads to a *renormalization* of the parameters of the expansion due to *Löwdin partitioning* that is why the Luttinger model has effectively reduced parameters than the simply bare theory coming from cutting out the parameters of a larger Kane matrix. An one-to-one correspondence between the parameters is only given if the irrelevant bands are infinitely large separated from the relevant part of the Hamiltonian. Another point is the hierarchy induced by symmetry (*symmetry hierarchy*). Bulk semiconductors with diamond-structure are a sub-class of one with zincblende-structure. Lipardi and Baldareschi [119] showed that

$$T_d \subset O_h \subset \mathcal{R}, \tag{C.2}$$

where $\mathcal{R}$ is the full rotation group, so that the Hamiltonian can be written as

$$H = H_{\mathcal{R}} + \Delta H_{O_h} + \Delta H_{T_d}, \tag{C.3}$$

with ΔH_{O_h} containing only the additional terms allowed by the symmetry O_h from going from $\mathcal{R}$ to O_h and the same for ΔH_{T_d} by going from O_h to T_d. This symmetry hierarchy is a very general aspect and can be extended by reversing its meaning. Starting with a T_d Hamiltonian we can split it into three parts: one which is diamond-like but have an axial approximation, a part which captures the terms missing to complete O_h and the rest is in the third part. We can write $H = H_{ax} + \Delta H_{O_h} + \Delta H_{T_d}$. This splitting is quite useful. One example is the growing of zinc-blende HgTe on CdTe. The axial symmetry is here around the growth direction providing a simplified model to study. The quantization axis can be chosen to be the crystallographic direction (001) without loss of generality. The Hamiltonian with full axial approximation around $\hat{z}$ is defined by the condition

$$e^{i\alpha J_z} H_{ax}(\mathcal{R}_{\hat{z}}(\alpha)\mathbf{k}) - H_{ax}(\mathbf{k}) e^{i\alpha J_z} = 0 \text{ for all } \alpha, \tag{C.4}$$

where J_z is the z-component of the total angular momentum and $\mathcal{R}_{\hat{z}}(\alpha)$ is the related rotation matrix

$$\mathcal{R}_{\hat{z}}(\alpha) = \begin{pmatrix} \cos\alpha & -\sin\alpha & 0 \\ \sin\alpha & \cos\alpha & 0 \\ 0 & 0 & 1 \end{pmatrix} \tag{C.5}$$

around $\hat{z}$ by the angle α. To become more explicit we have to fix the basis for the expansion. The basis states can be written as

$$\begin{aligned} |\Gamma_6, \pm 1/2\rangle &= |S\rangle \,|\uparrow / \downarrow\rangle , \\ |\Gamma_8, \pm 3/2\rangle &= \mp \frac{1}{\sqrt{2}} |X \pm iY\rangle \,|\uparrow / \downarrow\rangle , \\ |\Gamma_8, \pm 1/2\rangle &= \frac{1}{\sqrt{6}} (2\,|Z\rangle \,|\uparrow / \downarrow\rangle \mp |X \pm iY\rangle \,|\downarrow / \uparrow\rangle) \text{ and} \\ |\Gamma_7, \pm 1/2\rangle &= -\frac{1}{\sqrt{3}} (\pm |Z\rangle \,|\uparrow / \downarrow\rangle + |X \pm iY\rangle \,|\downarrow / \uparrow\rangle), \end{aligned} \tag{C.6}$$

where $|\downarrow / \uparrow\rangle$ correspond to the two spin eigenstates of the spin operator S_z with the eigenvalues $\pm 1/2$, $|S\rangle$ is the s-orbital $|l = 0, m_l = 0\rangle$ in the basis of L^2 and L_z describing the angular momentum and $|X/Y/Z\rangle$ are the related p_x, p_y and p_z orbitals. More popular names in the context of semiconductors concerning the normal ordering of these state as in CdTe is to name the states $|\Gamma_8, \pm 1/2\rangle$ *light hole* bands (LH) and $|\Gamma_8, \pm 3/2\rangle$ *heavy hole* bands (HH). With these states we can fix the Kane Hamiltonian in axial approximation H_{ax}. All the terms without strain are listed in Tab. C.2 with the common notation. The strain part is discussed extensively in the main text of this thesis. E_0 describes the energetic difference between the degenerate Γ_8 bands and the degenerate Γ_6 at $|\mathbf{k}| = 0$ and Δ_0 between Γ_8 and Γ_7. The parameters $F, \gamma_1, \gamma_2, \gamma_3$ describe the quadratic coupling to the remote bands while P describes a linear coupling. They are all material-specific parameters. To fulfill the axial condition we substituted γ_2 and γ_3 by their arithmetic mean $\bar{\gamma}$.

Table C.2: Expressions of the un-strained Kane model with diamond-like structure in the axial approximation. Here $\{A, B\}$ denotes the anti-commutator for the A, B operators, *c.p.* cyclic permutations of the preceding term and we defined $\gamma_0 = 2F + 1$ and $B = \hbar^2/(2m_0)$ with m_0 the free electron mass.

blocks	$\mathbf{k} \cdot \mathbf{p}$ interactions
$\mathcal{H}^{6,6}$	$E_0 + B\gamma_0\mathbf{k}^2$
$\mathcal{H}^{6,8}$	$\sqrt{3}P\,\mathbf{T} \cdot \mathbf{k}$
$\mathcal{H}^{6,7}$	$-\frac{1}{\sqrt{3}}\,P\,\boldsymbol{\sigma} \cdot \mathbf{k}$
$\mathcal{H}^{8,8}$	$-B\gamma_1\mathbf{k}^2 + 2B\overline{\gamma}\left[\left(J_x^2 - \frac{J^2}{3}\right)k_x^2 + c.p.\right]$
	$+B\overline{\gamma}\left[\{J_x, J_y\}\{k_x, k_y\} + c.p.\right]$
$\mathcal{H}^{8,7}$	$6B\overline{\gamma}\left[\left(T_{xx}^{\dagger}k_x^2 + c.p.\right) + \left(T_{xy}^{\dagger}\{k_x, k_y\} + c.p.\right)\right]$
$\mathcal{H}^{7,7}$	$-\Delta - B\gamma_1\mathbf{k}^2$

The appearing matrices are expressed in terms of the usual Pauli matrices $\sigma_{x,y,z}$, the $J = 3/2$ angular momentum matrices

$$\begin{aligned}
J_x &= \sqrt{3}/2\,\mathbb{1}_{2\times2} \otimes \sigma_x + (\sigma_x \otimes \sigma_x + \sigma_y \otimes \sigma_y)/2, \\
J_y &= \sqrt{3}/2\,\mathbb{1}_{2\times2} \otimes \sigma_y + (\sigma_y \otimes \sigma_x - \sigma_x \otimes \sigma_y)/2 \text{ and} \\
J_z &= \sigma_z \otimes \mathbb{1}_{2\times2} + \mathbb{1}_{2\times2} \otimes \sigma_z/2,
\end{aligned} \tag{C.7}$$

and the following T_i matrices

$$T_x = \frac{1}{3\sqrt{2}} \begin{pmatrix} -\sqrt{3} & 0 & 1 & 0 \\ 0 & -1 & 0 & \sqrt{3} \end{pmatrix}, \quad T_y = \frac{-i}{3\sqrt{2}} \begin{pmatrix} \sqrt{3} & 0 & 1 & 0 \\ 0 & 1 & 0 & \sqrt{3} \end{pmatrix},$$
$$T_z = \frac{\sqrt{2}}{3} \begin{pmatrix} 0 & 1 & 0 & 0 \\ 0 & 0 & 1 & 0 \end{pmatrix}, \quad T_{xx} = \frac{1}{3\sqrt{2}} \begin{pmatrix} 0 & -1 & 0 & \sqrt{3} \\ -\sqrt{3} & 0 & 1 & 0 \end{pmatrix},$$
$$T_{yy} = \frac{1}{3\sqrt{2}} \begin{pmatrix} 0 & -1 & 0 & -\sqrt{3} \\ \sqrt{3} & 0 & 1 & 0 \end{pmatrix}, \quad T_{zz} = \frac{\sqrt{2}}{3} \begin{pmatrix} 0 & 1 & 0 & 0 \\ 0 & 0 & -1 & 0 \end{pmatrix},$$
$$T_{yz} = \frac{i}{2\sqrt{6}} \begin{pmatrix} -1 & 0 & -\sqrt{3} & 0 \\ 0 & \sqrt{3} & 0 & 1 \end{pmatrix}, \quad T_{zx} = \frac{1}{2\sqrt{6}} \begin{pmatrix} -1 & 0 & \sqrt{3} & 0 \\ 0 & \sqrt{3} & 0 & -1 \end{pmatrix} \text{ and} \tag{C.8}$$
$$T_{xy} = \frac{i}{\sqrt{6}} \begin{pmatrix} 0 & 0 & 0 & -1 \\ -1 & 0 & 0 & 0 \end{pmatrix}.$$

The missing parts to restore T_d symmetry are listed in Tab. C.3. The parameter κ is the only parameter destroying axial symmetry in the point group O_h. The parameters $c(= C_k), B_8^{\pm}(= B_{8v}^{\pm})$ and $B_7(= B_{7v})$ describe the bulk-inversion asymmetry (BIA) of the zinc-blende structure. The leading order term is characterized by c which goes linear in $\mathbf{k}$. The origin of this c term in HgTe is the second-order interaction between Γ_8 and the $5d$ core levels [120, 121]. This term leads to a splitting of the HH and the LH bands linear along (110) given by

$$\Delta E_{LH} = \frac{\sqrt{3}}{2} c k_{(110)} + \mathcal{O}(k_{(110)}^2) \text{ and } \Delta E_{HH} = \frac{3\sqrt{3}}{2} c k_{(110)} + \mathcal{O}(k_{(110)}^2), \tag{C.9}$$

where $k_{(110)}$ is the $\mathbf{k}$-component along (110). By fitting the Kane model to experimental data or using a direct access by ab-inito calculations we get access to these parameters. The band structure parameters for a 6×6 Hamiltonian of HgTe (excluding the Γ_7 block) are given in Tab. C.4. For this description we assume that $\Delta \to \infty$. This corresponds to the idea that the Γ_7-block is large enough separated from the physically relevant part and so its weight in the wavefunction is 0.

Table C.3: Corrections to the Kane model to restore the full O_h and T_d symmetry with the same notations like in Tab. C.2, $\kappa = (\gamma_2 - \gamma_3)/2$ and the BIA parameters $c, B_8^{\pm}$ and B_7.

blocks	$\mathbf{k} \cdot \mathbf{p}$ interactions
$\Delta\mathcal{H}_{O_h}^{8,8}$	$2B\kappa\left[\left(J_x^2 - \frac{J^2}{3}\right)k_x^2 + c.p.\right]$
	$-B\kappa\left[\{J_x, J_y\}\{k_x, k_y\} + c.p.\right]$
$\Delta\mathcal{H}_{O_h}^{8,7}$	$6B\kappa\left[\left(T_{xx}^{\dagger}k_x^2 + c.p.\right) - \left(T_{xy}^{\dagger}\{k_x, k_y\} + c.p.\right)\right]$
$\Delta\mathcal{H}_{T_d}^{6,8}$	$\frac{\sqrt{3}}{2}iB_8^{+}(T_x\{k_y, k_z\} + c.p.)$
	$+\frac{\sqrt{3}}{2}iB_8^{-}\left[(T_{xx} - T_{yy})(k_z^2 - k^2/3) - T_{zz}(k_x^2 - k_y^2)\right]$
$\Delta\mathcal{H}_{T_d}^{6,7}$	$-\frac{i}{4\sqrt{3}}B_7(\sigma_x\{k_y, k_z\} + c.p.)$
$\Delta\mathcal{H}_{T_d}^{8,8}$	$\frac{1}{\sqrt{3}}c\left[\{J_x, J_y^2 - J_z^2\}k_x + c.p.\right]$
$\Delta\mathcal{H}_{T_d}^{8,7}$	$-i\sqrt{3}c(T_{yz}^{\dagger}k_x + c.p.)$

Table C.4: The band structure parameters for inversion-symmetric HgTe of Ref. [47] at $T = 0K$, the BIA parameters from Ref. [120] and Ref. [92]

E_0	F	P^2/B	γ_1	γ_2	γ_3	c	B^-	$B^+ \approx B_7$
−0.3 eV	0	18.8 eV	4.1	0.5	1.3	−74.6 meVÅ	1 eVÅ^2	−20 eVÅ^2

D Mirror and spin operators

All the topological aspects are discussed mostly within the three generic symmetries. Nevertheless there exists a richer periodic table of TIs and superconductors if we include lattice symmetries. They are called *topological crystalline insulators* [122]. These are symmetry-protected topological phases including crystal symmetries. It is true that they are weakly protected, but they can also give us insights in the symmetry classes of the generic symmetries. The analysis of the crystallographic point groups T_d and O_h exhibit mirror planes. Those planes are for instance useful for studying Hg-based chalcogenides[112]. In this chapter of the appendix we want to fix those mirror operators which are defined for a plane with normal vector $\mathbf{n}$ as

$$M_{\mathbf{n}} = \mathcal{I}\mathcal{R}^{orb}_{\mathbf{n}}(\pi)\mathcal{R}^{spin}_{\mathbf{n}}(\pi) f_{\mathbf{n}}, \tag{D.1}$$

where $\mathcal{I}$ is the matrix part of the inversion, $\mathcal{R}^{orb}_{\mathbf{n}}(\pi)$ is the one of the orbital rotation by π around the normal vector, the spin-rotation $\mathcal{R}^{spin}_{\mathbf{n}}(\pi) = i\mathbf{n}\cdot\boldsymbol{\sigma}$ acts on the spin space and $f_{\mathbf{n}}$ flips the sign of the $\mathbf{k}$ component parallel to $\mathbf{n}$. A tetrahedron is invariant under 6 mirror operations while a cube has 9. The (100), (010) an (001) planes are the three lost mirror planes going from a diamond structure to the zinc-blende structure. First of all we want to determine the three mirror planes $\mathbf{e}_{x,y,z}$ in the context of the extended 8×8 Kane model. The rotation of the orbital part leaves all states invariant except for a sign flip of the states $|j\rangle$ which are not aligned to $\mathbf{e}_i$ ($j \neq i$). This behavior can be written as $\mathcal{R}^{orb}_{\mathbf{e}_i}(\pi) = \mathcal{I}\mathcal{F}_{\mathbf{e}_i}$ where $\mathcal{F}_{\mathbf{e}_i}$ is the operator changes $|i\rangle \to -|i\rangle$ and

$$\mathcal{I} = \begin{pmatrix} \mathbb{1}^{\Gamma_6\Gamma_6} & \mathbb{0}^{\Gamma_6\Gamma_8} & \mathbb{0}^{\Gamma_6\Gamma_7} \\ . & -\mathbb{1}^{\Gamma_6\Gamma_6} & \mathbb{0}^{\Gamma_8\Gamma_7} \\ . & . & -\mathbb{1}^{\Gamma_7\Gamma_7} \end{pmatrix} \tag{D.2}$$

is the inversion matrix. The mirror operator can be brought in the form $M_{\mathbf{e}_i} = 2i\mathcal{F}_{\mathbf{e}_i} S_i f_{\mathbf{e}_i}$ using the 8×8 representation $\mathcal{R}^{spin}_{\mathbf{e}_i} = 2iS_i$ with the spin operators $[S_i, S_j] = i\varepsilon_{ijk}S_k$. They can be written explicitly in the block form

$$2S_i = \begin{pmatrix} \sigma_i & \mathbb{0}_{2\times 6} \\ \mathbb{0}_{6\times 2} & 2s_i \end{pmatrix} \tag{D.3}$$

using Pauli matrices for the Γ_6 bands and the spin matrices with the small letters for the Γ_7 and Γ_8 bands. Those 6×6 matrices are given by the three components

$$s_x = \begin{pmatrix} 0 & \frac{1}{2\sqrt{3}} & 0 & 0 & \frac{1}{\sqrt{6}} & 0 \\ . & 0 & \frac{1}{3} & 0 & 0 & \frac{1}{3\sqrt{2}} \\ . & . & 0 & \frac{1}{2\sqrt{3}} & -\frac{1}{3\sqrt{2}} & 0 \\ . & . & . & 0 & 0 & -\frac{1}{\sqrt{6}} \\ . & . & . & . & 0 & -\frac{1}{6} \\ . & . & . & . & . & 0 \end{pmatrix},$$

$$s_y = \begin{pmatrix} 0 & -\frac{i}{2\sqrt{3}} & 0 & 0 & -\frac{i}{\sqrt{6}} & 0 \\ . & 0 & -\frac{i}{3} & 0 & 0 & -\frac{i}{3\sqrt{2}} \\ . & . & 0 & -\frac{i}{2\sqrt{3}} & -\frac{i}{3\sqrt{2}} & 0 \\ . & . & . & 0 & 0 & -\frac{i}{\sqrt{6}} \\ . & . & . & . & 0 & \frac{i}{6} \\ . & . & . & . & . & 0 \end{pmatrix} \tag{D.4}$$

and the z component

$$s_z = \begin{pmatrix} \frac{1}{2} & 0 & 0 & 0 & 0 & 0 \\ . & \frac{1}{6} & 0 & 0 & -\frac{\sqrt{2}}{3} & 0 \\ . & . & -\frac{1}{6} & 0 & 0 & -\frac{\sqrt{2}}{3} \\ . & . & . & -\frac{1}{2} & 0 & 0 \\ . & . & . & . & -\frac{1}{6} & 0 \\ . & . & . & . & . & \frac{1}{6} \end{pmatrix}.$$

The mirror operators are then fixed to be

$$M_x = i \begin{pmatrix} \sigma_x & \mathbb{0}_{2\times 4} & \mathbb{0}_{2\times 2} \\ \mathbb{0}_{4\times 2} & \sigma_x \otimes \sigma_x & \mathbb{0}_{4\times 2} \\ \mathbb{0}_{2\times 2} & \mathbb{0}_{2\times 4} & -\sigma_x \end{pmatrix}, M_y = i \begin{pmatrix} \sigma_y & \mathbb{0}_{2\times 4} & \mathbb{0}_{2\times 2} \\ \mathbb{0}_{4\times 2} & -\sigma_x \otimes \sigma_y & \mathbb{0}_{4\times 2} \\ \mathbb{0}_{2\times 2} & \mathbb{0}_{2\times 4} & -\sigma_y \end{pmatrix} \tag{D.5}$$

related by $M_y = e^{i\pi/2J_z} M_{-x} e^{-i\pi/2J_z}$ and

$$M_z = i \begin{pmatrix} \sigma_z & \mathbb{0}_{2\times4} & \mathbb{0}_{2\times2} \\ \mathbb{0}_{4\times2} & \sigma_0 \otimes \sigma_z & \mathbb{0}_{4\times2} \\ \mathbb{0}_{2\times2} & \mathbb{0}_{2\times4} & -\sigma_z \end{pmatrix}. \tag{D.6}$$

For the other 6 directions (illustrated in Fig. D.1) we can use a rotation matrix connecting the mirror operators. They are the diagonal planes in a cubic description. The vectors point in the direction: (110), $(\bar{1}10)$ and in all equivalent directions following out of a cyclic permutation of those two planes defined by a $2\pi/3$ or $4\pi/3$ rotation around the axes (111). To fix the normal vectors of the planes we chose a right-handed system connecting

$$M_x \to M_{(110)} \to M_y \to M_{(\bar{1}10)} \to M_{-x} \tag{D.7}$$

by rotations around the z-axis with the angle $\pi/4$. We can write

$$M_{(110)} = e^{-i\pi/4J_z} M_x e^{+i\pi/4J_z} \text{ and } M_{(\bar{1}10)} = e^{-i\pi/4J_z} M_y e^{+i\pi/4J_z}. \tag{D.8}$$

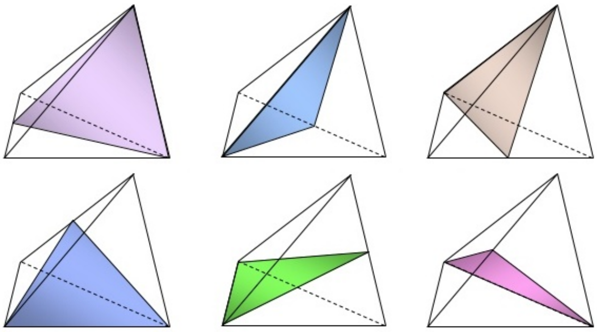

Figure D.1: A tetrahedron represents the symmetry group T_d with 6 mirror planes.

Bibliography

[1] A. Hatcher. *Algebraic Topology.* Cambridge University Press, 2002.

[2] J. K. Pachos and S. H. Simon. Focus on topological quantum computation. *New J. Phys.*, 16(6):065003, 2014.

[3] A. Kitaev. Periodic table for topological insulators and superconductors. *AIP Conf. Proc.*, 1134:22, 2009.

[4] J. C. Y. Teo and C. L. Kane. Topological defects and gapless modes in insulators and superconductors. *Phys. Rev. B*, 82:115120, 2010.

[5] C. Nash. Ch. 12 - Topology and Physics – a Historical Essay. In I.M. James, editor, *History of Topology*, pages 359–415. North-Holland, Amsterdam, 1999.

[6] A. W. W. Ludwig. Topological phases: classification of topological insulators and superconductors of non-interacting fermions, and beyond. *Phys. Scr.*, 2016(T168):014001, 2016.

[7] A. Altland and M. R. Zirnbauer. Nonstandard symmetry classes in mesoscopic normal-superconducting hybrid structures. *Phys. Rev. B*, 55:1142, 1997.

[8] M.R. Zirnbauer. Riemannian symmetric superspaces and their origin in random matrix theory. *J. Math. Phys.*, 37:4986, 1996.

[9] A. P. Schnyder, S. Ryu, A. Furusaki, and A. W. W. Ludwig. Classification of topological insulators and superconductors in three spatial dimensions. *Phys. Rev. B*, 78:195125, 2008.

[10] S. Ryu, A. P. Schnyder, A. Furusaki, and A. W. W. Ludwig. Topological insulators and superconductors: tenfold way and dimensional hierarchy. *New J. Phys.*, 12(6):065010, 2010.

[11] W. P. Su, J. R. Schrieffer, and A. J. Heeger. Solitons in Polyacetylene. *Phys. Rev. Lett.*, 42:1698, 1979.

[12] R. Jackiw and C. Rebbi. Solitons with fermion number 1/2. *Phys. Rev. D*, 13:3398, 1976.

[13] K. v. Klitzing, G. Dorda, and M. Pepper. New Method for High-Accuracy Determination of the Fine-Structure Constant Based on Quantized Hall Resistance. *Phys. Rev. Lett.*, 45:494, 1980.

[14] D. J. Thouless, M. Kohmoto, M. P. Nightingale, and M. den Nijs. Quantized Hall Conductance in a Two-Dimensional Periodic Potential. *Phys. Rev. Lett.*, 49:405, 1982.

[15] M. Kohmoto. Topological invariant and the quantization of the Hall conductance. *Ann. Phys.*, 160(2):343, 1985.

[16] C. F. Lo. A gauge-independent formulation of the Landau level problem. *Eur. J. Phys.*, 13(3):125, 1992.

[17] W. N. Mei and Y. C. Lee. Harmonic oscillator with potential barriers-exact solutions and perturbative treatments. *J. Phys. A: Math. Gen.*, 16(8):1623, 1983.

[18] M. Abramowitz and I.A. Stegun. *Handbook of Mathematical Functions: with Formulas, Graphs, and Mathematical Tables.* Dover Books on Mathematics. Dover Publications, 2012.

[19] B. I. Halperin. Quantized Hall conductance, current-carrying edge states, and the existence of extended states in a two-dimensional disordered potential. *Phys. Rev. B*, 25:2185, 1982.

[20] R. B. Laughlin. Quantized Hall conductivity in two dimensions. *Phys. Rev. B*, 23:5632, 1981.

[21] T. Neupert, L. Santos, S. Ryu, C. Chamon, and C. Mudry. Noncommutative geometry for three-dimensional topological insulators. *Phys. Rev. B*, 86:035125, 2012.

[22] Douglas R. Hofstadter. Energy levels and wave functions of Bloch electrons in rational and irrational magnetic fields. *Phys. Rev. B*, 14:2239, 1976.

[23] Y. Hatsugai and M. Kohmoto. Energy spectrum and the quantum Hall effect on the square lattice with next-nearest-neighbor hopping. *Phys. Rev. B*, 42:8282, 1990.

[24] A. N. Redlich. Parity violation and gauge noninvariance of the effective gauge field action in three dimensions. *Phys. Rev. D*, 29:2366, 1984.

[25] S. Deser, R. Jackiw, and S. Templeton. Three-Dimensional Massive Gauge Theories. *Phys. Rev. Lett.*, 48:975, 1982.

[26] X.-L. Qi, T. L. Hughes, and S.-C. Zhang. Topological field theory of time-reversal invariant insulators. *Phys. Rev. B*, 78:195424, 2008.

[27] Z. Wang, X.-L. Qi, and S.-C. Zhang. Topological Order Parameters for Interacting Topological Insulators. *Phys. Rev. Lett.*, 105:256803, 2010.

[28] M. Fruchart, D. Carpentier, and K. Gawędzki. Parallel transport and band theory in crystals. *EPL*, 106(6):60002, 2014.

[29] C. L. Kane and E. J. Mele. Quantum Spin Hall Effect in Graphene. *Phys. Rev. Lett.*, 95:226801, 2005.

[30] C. L. Kane and E. J. Mele. Z_2 Topological Order and the Quantum Spin Hall Effect. *Phys. Rev. Lett.*, 95:146802, 2005.

[31] L. Fu and C. L. Kane. Time reversal polarization and a Z_2 adiabatic spin pump. *Phys. Rev. B*, 74:195312, 2006.

[32] H. A. Kramers. Théorie générale de la rotation paramagnétique dans les cristaux. *Proceedings Koninklijke Akademie van Wetenschappen*, 33:959, 1930.

[33] G. H. Wannier. The Structure of Electronic Excitation Levels in Insulating Crystals. *Phys. Rev.*, 52:191, 1937.

[34] R. D. King-Smith and D. Vanderbilt. Theory of polarization of crystalline solids. *Phys. Rev. B*, 47:1651, 1993.

[35] R. Yu, X. L. Qi, A. Bernevig, Z. Fang, and X. Dai. Equivalent expression of $\mathbb{Z}_2$ topological invariant for band insulators using the non-Abelian Berry connection. *Phys. Rev. B*, 84:075119, 2011.

[36] L. Fu, C. L. Kane, and E. J. Mele. Topological Insulators in Three Dimensions. *Phys. Rev. Lett.*, 98:106803, 2007.

[37] L. Fu and C. L. Kane. Topological insulators with inversion symmetry. *Phys. Rev. B*, 76:045302, 2007.

[38] F. Wilczek. Two applications of axion electrodynamics. *Phys. Rev. Lett.*, 58:1799, 1987.

[39] M. M. Vazifeh and M. Franz. Quantization and 2π periodicity of the axion action in topological insulators. *Phys. Rev. B*, 82:233103, 2010.

[40] G. E. Volovik. *The Universe in a Helium Droplet*. International Series of Monographs on Physics. OUP Oxford, 2009.

[41] G. E. Volovik. Topological invariants for standard model: From semi-metal to topological insulator. *JETP Lett.*, 91(2):55, 2010.

[42] J. M. Luttinger and W. Kohn. Motion of Electrons and Holes in Perturbed Periodic Fields. *Phys. Rev.*, 97:869, 1955.

[43] E. O. Kane. Band structure of indium antimonide. *J. Phys. Chem. Solids*, 1(4):249, 1957.

[44] J. M. Luttinger. Quantum Theory of Cyclotron Resonance in Semiconductors: General Theory. *Phys. Rev.*, 102:1030, 1956.

[45] M. G. Burt. The justification for applying the effective-mass approximation to microstructures. *J. Phys.: Condens. Matter*, 4(32):6651, 1992.

[46] R. Eppenga, M. F. H. Schuurmans, and S. Colak. New $k \cdot p$ theory for $\mathrm{GaAs/Ga_{1-x}A1_xAs}$-type quantum wells. *Phys. Rev. B*, 36:1554, 1987.

[47] E. G. Novik, A. Pfeuffer-Jeschke, T. Jungwirth, V. Latussek, C. R. Becker, G. Landwehr, H. Buhmann, and L. W. Molenkamp. Band structure of semimagnetic $\mathrm{Hg}_{1-y}\mathrm{Mn}_y\mathrm{Te}$ quantum wells. *Phys. Rev. B*, 72:035321, 2005.

[48] R. G. Veprek, S. Steiger, and B. Witzigmann. Ellipticity and the spurious solution problem of $\mathbf{k} \cdot \mathbf{p}$ envelope equations. *Phys. Rev. B*, 76:165320, 2007.

[49] M. V. Kisin, B. L. Gelmont, and S. Luryi. Boundary-condition problem in the Kane model. *Phys. Rev. B*, 58:4605, 1998.

[50] D.M. Gitman, I.V. Tyutin, and B.L. Voronov. *Self-adjoint Extensions in Quantum Mechanics - General Theory and Applications to Schrödinger and Dirac Equations with Singular Potentials*. Birkhäuser Boston, 2012.

[51] M. Reed and B. Simon. *Methods of modern mathematical physics - II: Fourier analysis, self-adjointness*. Academic Press, Inc., 1975.

[52] M. T. Ahari, G. Ortiz, and B. Seradjeh. On the Role of Self-Adjointness in the Continuum Formulation of Topological Quantum Phases. *arXiv*, 1508.02682, 2015.

[53] V. V. Enaldiev, I. V. Zagorodnev, and V. A. Volkov. Boundary conditions and surface state spectra in topological insulators. *JETP Lett.*, 101(2):89, 2015.

[54] M. Asorey, A. Ibort, and G. Marmo. Global Theory of Quantum Boundary Conditions and Topology Change. *Int. J. Mod. Phys. A*, 20(05):1001, 2005.

[55] A. Medhi and V. B. Shenoy. Continuum theory of edge states of topological insulators: variational principle and boundary conditions. *J. Phys.: Condens. Matter*, 24(35):355001, 2012.

[56] V. N. Men'shov, V. V. Tugushev, T. V. Menshchikova, S. V. Eremeev, P. M. Echenique, and E. V. Chulkov. Modelling near-surface bound electron states in a 3D topological insulator: analytical and numerical approaches. *J. Phys.: Condens. Matter*, 26(48):485003, 2014.

[57] F. D. M. Haldane. Model for a Quantum Hall Effect without Landau Levels: Condensed-Matter Realization of the "Parity Anomaly". *Phys. Rev. Lett.*, 61:2015, 1988.

[58] X.-L. Qi, Y.-S. Wu, and S.-C. Zhang. Topological quantization of the spin Hall effect in two-dimensional paramagnetic semiconductors. *Phys. Rev. B*, 74:085308, 2006.

[59] S. Konschuh, M. Gmitra, and J. Fabian. Tight-binding theory of the spin-orbit coupling in graphene. *Phys. Rev. B*, 82:245412, 2010.

[60] R. Winkler and U. Zülicke. Invariant expansion for the trigonal band structure of graphene. *Phys. Rev. B*, 82:245313, 2010.

[61] P.-O. Löwdin. Partitioning technique, perturbation theory, and rational approximations. *Int. J. Quantum Chem.*, 21(1):69, 1982.

[62] S. Ryu, C. Mudry, C.-Y. Hou, and C. Chamon. Masses in graphenelike two-dimensional electronic systems: Topological defects in order parameters and their fractional exchange statistics. *Phys. Rev. B*, 80:205319, 2009.

[63] H. Deshpande and R. Winkler. Effective Hamiltonian for edge states in graphene. *arXiv*, 1603.04329, 2016.

[64] J. Li, I. Martin, M. Büttiker, and A. F. Morpurgo. Marginal topological properties of graphene: a comparison with topological insulators. *Physica Scripta*, 2012(T146):014021, 2012.

[65] A. R. Akhmerov and C. W. J. Beenakker. Boundary conditions for Dirac fermions on a terminated honeycomb lattice. *Phys. Rev. B*, 77:085423, 2008.

[66] L. Brey and H. A. Fertig. Electronic states of graphene nanoribbons studied with the Dirac equation. *Phys. Rev. B*, 73:235411, 2006.

[67] L. Cano-Cortés, C. Ortix, and J. van den Brink. Fundamental Differences between Quantum Spin Hall Edge States at Zigzag and Armchair Terminations of Honeycomb and Ruby Nets. *Phys. Rev. Lett.*, 111:146801, 2013.

[68] E. McCann and V. I. Fal'ko. Landau-Level Degeneracy and Quantum Hall Effect in a Graphite Bilayer. *Phys. Rev. Lett.*, 96:086805, 2006.

[69] J. Li, A. F. Morpurgo, M. Büttiker, and I. Martin. Marginality of bulk-edge correspondence for single-valley Hamiltonians. *Phys. Rev. B*, 82:245404, 2010.

[70] G. De Nittis and K. Gomi. Classification of "Real" Bloch-bundles: Topological quantum systems of type AI. *J. Geom. Phys.*, 86:303, 2014.

[71] B. A. Bernevig, T. L. Hughes, and S.-C. Zhang. Quantum Spin Hall Effect and Topological Phase Transition in HgTe Quantum Wells. *Science*, 314(5806):1757, 2006.

[72] B. Zhou, H.-Z. Lu, R.-L. Chu, S.-Q. Shen, and Q. Niu. Finite Size Effects on Helical Edge States in a Quantum Spin-Hall System. *Phys. Rev. Lett.*, 101:246807, 2008.

[73] P. A. M. Dirac. The Quantum Theory of the Electron. *Proc. R. Soc. A*, 117(778):610, 1928.

[74] S.-Q. Shen, W.-Y. Shan, and D. H. Lu. Topological Insulator and the Dirac equation. *SPIN*, 01(01):33, 2011.

[75] W.-Y. Shan, H.-Z. Lu, and S.-Q. Shen. Effective continuous model for surface states and thin films of three-dimensional topological insulators. *New J. Phys.*, 12(4):043048, 2010.

[76] K. Sun, H. Yao, E. Fradkin, and S. A. Kivelson. Topological Insulators and Nematic Phases from Spontaneous Symmetry Breaking in 2D Fermi Systems with a Quadratic Band Crossing. *Phys. Rev. Lett.*, 103:046811, 2009.

[77] K. Sun, W. V. Liu, A. Hemmerich, and S. Das Sarma. Topological semimetal in a fermionic optical lattice. *Nat. Phys.*, 8(1):67, 2012.

[78] C. H. Lee, R. Thomale, and X.-L. Qi. Pseudopotential formalism for fractional Chern insulators. *Phys. Rev. B*, 88:035101, 2013.

[79] D. Pesin and A. H. MacDonald. Spintronics and pseudospintronics in graphene and topological insulators. *Nat. Mater.*, 11(5):409, 2012.

[80] S.-C. Wu, B. Yan, and C. Felser. Ab initio study of topological surface states of strained HgTe. *EPL*, 107(5):57006, 2014.

[81] C. Brüne, C. X. Liu, E. G. Novik, E. M. Hankiewicz, H. Buhmann, Y. L. Chen, X. L. Qi, Z. X. Shen, S. C. Zhang, and L. W. Molenkamp. Quantum Hall Effect from the Topological Surface States of Strained Bulk HgTe. *Phys. Rev. Lett.*, 106:126803, 2011.

[82] C. Bouvier, T. Meunier, P. Ballet, X. Baudry, R. B. G. Kramer, and L. Lévy. Strained HgTe: a textbook 3D topological insulator. *arXiv*, 1112.2092, 2011.

[83] O. Crauste, Y. Ohtsubo, P. Ballet, P. A. L. Delplace, D. Carpentier, C. Bouvier, T. Meunier, A. Taleb-Ibrahimi, and L. Lévy. Topological surface states of strained Mercury-Telluride probed by ARPES. *arXiv*, 1307.2008, 2013.

[84] R. Winkler. *Spin-Orbit Coupling Effects in Two-Dimensional Electron and Hole Systems*. Springer Berlin Heidelberg, 2005.

[85] X. Dai, T. L. Hughes, X.-L. Qi, Z. Fang, and S.-C. Zhang. Helical edge and surface states in HgTe quantum wells and bulk insulators. *Phys. Rev. B*, 77:125319, 2008.

[86] R.-L. Chu, W.-Y. Shan, J. Lu, and S.-Q. Shen. Surface and edge states in topological semimetals. *Phys. Rev. B*, 83:075110, 2011.

[87] A. Kobayashi, O. F. Sankey, and J. D. Dow. Chemical trends for defect energy levels in $\mathrm{Hg}_{(1-x)}\mathrm{Cd}_x\mathrm{Te}$. *Phys. Rev. B*, 25:6367, 1982.

[88] P. Vogl, H. P. Hjalmarson, and J. D. Dow. A Semi-empirical tight-binding theory of the electronic structure of semiconductors. *J. Phys. Chem. Solids*, 44(5):365, 1983.

[89] M. König, S. Wiedmann, C. Brüne, A. Roth, H. Buhmann, L. W. Molenkamp, X.-L. Qi, and S.-C. Zhang. Quantum Spin Hall Insulator State in HgTe Quantum Wells. *Science*, 318(5851):766, 2007.

[90] D. G. Rothe, R. W. Reinthaler, C.-X. Liu, L. W. Molenkamp, S.-C. Zhang, and E. M. Hankiewicz. Fingerprint of different spin–orbit terms for spin transport in HgTe quantum wells. *New J. Phys.*, 12(6):065012, 2010.

[91] B. A. Bernevig and S.-C. Zhang. Intrinsic Spin Hall Effect in the Two-Dimensional Hole Gas. *Phys. Rev. Lett.*, 95:016801, 2005.

[92] R. Winkler, L. Y. Wang, Y. H. Lin, and C. S. Chu. Robust level coincidences in the subband structure of quasi-2D systems. *Solid State Commun.*, 152(23):2096, 2012.

[93] F. Zhang, C. L. Kane, and E. J. Mele. Surface states of topological insulators. *Phys. Rev. B*, 86:081303, 2012.

[94] C. Ortix, J. W. F. Venderbos, R. Hayn, and J. van den Brink. Absence of helical surface states in bulk semimetals with broken inversion symmetry. *Phys. Rev. B*, 89:121408, 2014.

[95] G. L. Bir and G. E. Pikus. *Symmetry and Strain-induced Effects in Semiconductors*. A Halsted Press book. Wiley, 1974.

[96] J. M. Hinckley and J. Singh. Influence of substrate composition and crystallographic orientation on the band structure of pseudomorphic Si-Ge alloy films. *Phys. Rev. B*, 42:3546, 1990.

[97] R. I. Cottam and G. A. Saunders. The elastic behaviour of mercury telluride. *J. Phys. Chem. Solids*, 36(3):187, 1975.

[98] V. Latussek, C. R. Becker, G. Landwehr, R. Bini, and L. Ulivi. Deformation potentials of the semimetal HgTe. *Phys. Rev. B*, 71:125305, 2005.

[99] K. Takita, K. Onabe, and S. Tanaka. Anomalous magnetoresistance and band crossing in uniaxially compressed HgTe. *Physica status solidi (b)*, 92(1):297, 1979.

[100] T. Rauch, S. Achilles, J. Henk, and I. Mertig. Spin Chirality Tuning and Topological Semimetals in Strained $\mathrm{HgTe}_x\mathrm{S}_{1-x}$. *Phys. Rev. Lett.*, 114:236805, 2015.

[101] S. Zaheer, S. M. Young, D. Cellucci, J. C. Y. Teo, C. L. Kane, E. J. Mele, and A. M. Rappe. Spin texture on the Fermi surface of tensile-strained HgTe. *Phys. Rev. B*, 87:045202, 2013.

[102] H. B. Nielsen and M. Ninomiya. The Adler-Bell-Jackiw anomaly and Weyl fermions in a crystal. *Phys. Lett. B*, 130(6):389, 1983.

[103] J. I. Ruan, S.-K. Jian, H. Yao, H. Zhang, S.-C. Zhang, and D. Xing. Symmetry-protected ideal Weyl semimetal in HgTe-class materials. *Nat. Commun.*, 7:11136, 2016.

[104] J. C. Y. Teo, L. Fu, and C. L. Kane. Surface states and topological invariants in three-dimensional topological insulators: Application to $\mathrm{Bi}_{1-x}\mathrm{Sb}_x$. *Phys. Rev. B*, 78:045426, 2008.

[105] M. S. Dresselhaus, G. Dresselhaus, and A. Jorio. *Group Theory - Application to the Physics of Condensed Matter*. Springer-Verlag Berlin Heidelberg, 2008.

[106] P. Y. Yu and M. Cardona. *Fundamentals of Semiconductors*. Springer Berlin Heidelberg, 2010.

[107] F. Virot, R. Hayn, M. Richter, and J. van den Brink. Engineering Topological Surface States: HgS, HgSe, and HgTe. *Phys. Rev. Lett.*, 111:146803, 2013.

[108] M. I. Aroyo, A. Kirov, C. Capillas, J. M. Perez-Mato, and H. Wondratschek. Bilbao Crystallographic Server. II. Representations of crystallographic point groups and space groups. *Acta Cryst. A*, 62(2):115, 2006.

[109] G. Khanna, S. Mukhopadhyay, R. Simon, and N. Mukunda. Geometric Phases for $SU(3)$ Representations and Three Level Quantum Systems. *Ann. Phys.*, 253(1):55, 1997.

[110] R. Barnett, G. R. Boyd, and V. Galitski. SU(3) Spin-Orbit Coupling in Systems of Ultracold Atoms. *Phys. Rev. Lett.*, 109:235308, 2012.

[111] A. Delin. First-principles calculations of the II-VI semiconductor β-HgS: Metal or semiconductor. *Phys. Rev. B*, 65:153205, 2002.

[112] Q.-Z. Wang, S.-C. Wu, C. Felser, B. Yan, and C.-X. Liu. Spin texture and mirror Chern number in Hg-based chalcogenides. *Phys. Rev. B*, 91:165435, 2015.

[113] M. Legner, A. Rüegg, and M. Sigrist. Surface-State Spin Textures and Mirror Chern Numbers in Topological Kondo Insulators. *Phys. Rev. Lett.*, 115:156405, 2015.

[114] L. Fu. Hexagonal Warping Effects in the Surface States of the Topological Insulator $\mathrm{Bi}_2\mathrm{Te}_3$. *Phys. Rev. Lett.*, 103:266801, 2009.

[115] D. L. Bergman and G. Refael. Bulk metals with helical surface states. *Phys. Rev. B*, 82:195417, 2010.

[116] U. Fano. Effects of Configuration Interaction on Intensities and Phase Shifts. *Phys. Rev.*, 124:1866, 1961.

[117] S. Chadov, X. Qi, J. Kübler, G. H. Fecher, C. Felser, and S. C. Zhang. Tunable multifunctional topological insulators in ternary Heusler compounds. *Nat. Mater.*, 9(7):541, 2010.

[118] G. Dresselhaus. Spin-Orbit Coupling Effects in Zinc Blende Structures. *Phys. Rev.*, 100:580, 1955.

[119] N. O. Lipari and A. Baldereschi. Angular Momentum Theory and Localized States in Solids. Investigation of Shallow Acceptor States in Semiconductors. *Phys. Rev. Lett.*, 25:1660, 1970.

[120] M. Cardona, N. E. Christensen, and G. Fasol. Terms Linear in k in the Band Structure of Zinc-Blende-Type Semiconductors. *Phys. Rev. Lett.*, 56:2831, 1986.

[121] S.-H. Wei and A. Zunger. Role of metal d states in II-VI semiconductors. *Phys. Rev. B*, 37:8958, 1988.

[122] L. Fu. Topological Crystalline Insulators. *Phys. Rev. Lett.*, 106:106802, 2011.

Zusammenfassung auf Deutsch

Diese Arbeit beschäftigt sich mit topologischen Isolatoren (TI) und deren effektive Beschreibung mit Hilfe von $\mathbf{k} \cdot \mathbf{p}$ Hamiltonians am Beispiel von einfachen topologischen Modellen und Queckersilbertellurid (HgTe). Die Beschreibung der physikalisch-relevanten Phänomene erfolgt dabei nur effektiv mit langreichweitigen Niedrig-Energie-Anregungen und trägt einen lokalen Charakter in Potenzen von Diffentialoperatoren ∂_i. Die dabei auftretenden topologischen Aspekte sind jedoch globale Eigenschaften des Systems. Diese Dichotomie zwischen lokalen und globalen Eigenschaften gibt Anlass sich zu fragen, ob eine gewisse effektive Beschreibung den korrekten topologischen Inhalt in sich trägt. Anders formuliert könnte man fragen, ob die Gitter-Theorie die topologischen Informationen in eine approximative Theorie vererbt oder nicht.

Im ersten Teil beschäftigen wir uns mit den topologischen Isolatoren im Allgemeinen. Hierbei betrachten wir illustrative Beispiele, die uns verdeutlichen sollen was eine effektive Beschreibung leisten muss, um hinsichtlich ihres topologischen Aspekts relevant zu sein. Daraus folgt die Idee, dass wir sicherstellen müssen, dass jeder effektiven Theorie ein topologischer Aspekt innewohnen muss, um Aussagen zu treffen. Durch das Studium von 2-Band Systemen können wir eine neue Klasse von effektiven Hamiltonians neben den schon häufig-verwendeten kompakten Theorien von topologischen Hamiltonians identifizieren. Der Unterschied liegt nicht nur allein in der Kompaktheit dieser Modelle, sondern auch in der Beschreibung der topologischen Invarianten und der dazugehörigen Bulk-Oberflächen-Korrespondenz.

Im weiteren Teil betrachten wir HgTe, welches sich nach epitaxischem Wachsen auf CdTe von einem Halbmetall zu einem starken topologischen Isolator wandelt. Die nicht-topologischen Eigenschaften dieses Materials können sehr gut mit einer Niedrig-Energie-Theorie beschrieben werden. Das Model, welches den langwelligen Teil der Physik beschreibt, ist der sogenannte Kane Hamiltonian. Mit dem in den ersten Kapiteln entdeckten Wissen über den topologischen Ursprung in effektiven Theorien können wir nun sicherstellen, dass unsere Schlussfolgerungen, welche wir aus dieser Theorie ziehen, topologisch d.h. mathematisch haltbar sind. Dies ist ein Aspekt, welcher in vielen Arbeiten komplett ignoriert wird, aber absolut notwendig ist.

Der Vorteil einer effektiven Beschreibung liegt klar auf der Hand: Eine Analyse des Kane Hamiltonians gibt uns die Möglichkeit die topologischen Oberflächenzustände unter der Annahme einer freien Oberfläche direkt analytisch zu ermitteln. Die Fermi-Geschwindigkeit beschreibt hierbei die konstante Änderung der Energie entlang der Propagationsrichtung der chiralen Oberflächenzustände. Die Zerfallslänge gibt an, wie tief dieser Zustand in den TI eindringt kann, wenn er im Kontakt mit dem Vakuum steht. Dabei werden zwei interessante Aspekte besonders betrachtet: Auf der einen Seite sind es die sogenannten Seiten-Oberflächen mit deren Spin-Struktur, welche eine interessante Abhängigkeit unter mechanischer Spannung aufweisen, auf der anderen Seite betrachten wir die Haupt-Oberfläche definiert durch die Heterostruktur-Stapelung. Im Gegensatz zu den Seitenflächen zeigt sich hier, dass der Dirac-Kegel in Bulk-Zuständen eingebettet ist. Wir geben Antwort auf die Frage, was passiert, wenn wir von dem meistverwendeten künstlichen inversionssymmetrischen System zu einem System mit realistischer Zinkblende-Struktur überwechseln, und zeigen, dass die Oberflächen-Potentiale einen sehr starken Einfluss auf die Oberflächenzustände haben. Sie bestimmen maßgeblich die Existenz und die Eigenschaften der niedrig-dimensionalen Dirac-Physik.

Publication List

1. Quantum collapses and revivals of matter wave in dynamics of symmetry breaking.

   F. Kirtschig, J. Rijnbeek, J. van den Brink, and C. Ortix.

   Phys. Rev. B 87, 014304 (2013).

   Abstract: Quantum processes can be described in terms of a quasiprobability distribution (the Wigner distribution) analogous to the phase-space probability distribution of the classical realm. In contrast to the incomplete glimpse of the wave function that is achievable in a single shot experiment, the Wigner distribution, accessible by quantum state tomography, reflects the full quantum state. We show that during the fundamental symmetry-breaking process of a generic quantum system, with a symmetry-breaking field driving the quantum system far from equilibrium, the Wigner distribution evolves continuously with the system undergoing a sequence of revivals into the symmetry-unbroken state, followed by collapses onto a quasiclassical state akin to the one realized in infinite-size systems. We show that generically this state is completely delocalized both in momentum and in real space.

   No part of this work is included in the thesis.

2. Topological classification of $\mathbf{k} \cdot \mathbf{p}$ Hamiltonians for Chern insulators.

   F. Kirtschig, J. van den Brink, and C. Ortix.

   arXiv:1503.07456 (2015).

   Abstract: We proof the existence of two different topological classes of low-energy $\mathbf{k} \cdot \mathbf{p}$ Hamiltonians for Chern insulators. Using the paradigmatic example of single-valley two-band models, we show that $\mathbf{k} \cdot \mathbf{p}$ Hamiltonians that we dub local have a topological invariant corresponding precisely to the Hall conductivity and linearly dispersing chiral midgap edge states at the expansion point. Non-local $\mathbf{k} \cdot \mathbf{p}$ Hamiltonians have a topological invariant that is twice the Hall conductivity of the system. This class is characterized by a non-local bulk-edge correspondence with midgap edge states appearing away from the high-symmetry $\mathbf{k} \cdot \mathbf{p}$ expansion point.

A large part of this publication has been included in Chapter 4 and 5 of this dissertation.

3. Surface-state spin textures in strained bulk HgTe: Strain-induced topological phase transitions.

   F. Kirtschig, J. van den Brink, and C. Ortix.

   Phys. Rev. B 94, 235437 (2016).

   Abstract: The opening of a band gap due to compressive uniaxial strain renders bulk HgTe a strong three-dimensional topological insulator with protected gapless surface states at any surface. By employing a six-band $\mathbf{k} \cdot \mathbf{p}$ model, we determine the spin textures of the topological surface states of bulk HgTe uniaxially strained along the (100) direction. We show that at the (010) and (001) surfaces, an increase in the strain magnitude triggers a topological phase transition where the winding number of the surface-state spin texture is flipped while the four topological invariants characterizing the bulk band structure of the material are unchanged.

   A large part of this publication has been included in Chapter 6 of this dissertation.

4. Dirac physics in the topological surface spectrum of uniaxial strained HgTe.

   F. Kirtschig, J. van den Brink, and C. Ortix.

   unpuplished.

   Abstract: The existence of topological surface states especially Dirac cones are the hallmark for 3D topological insulators and essential for many desired applications in quantum computing. In the paradigmatic example of uniaxial strained HgTe we will show that the existence and the features of those Dirac cones depend crucial on the boundary conditions and their strict topological protection which we can understand by analyzing its Mirror Chern physics.

   Parts of this publication have been included in Chapter 6 of this dissertation.

Acknowledgements/Danksagung

English:
Quite a lot of people have provided me with support, new ideas, answers to open questions, assistance, discussions and spread a good atmosphere during the last years. During my time at the IFW, the most-important person is Carmine Ortix. He always helped me with his enormous knowledge about pretty much everything. Discussions with him were always enlightening and led to new solutions. Carmine always encouraged me to try new paths and I am deeply grateful for his advices and his excellent mentoring. I am especially thankful for Jeroen van den Brink and all other colleagues at the IFW, who provided an inspiring environment. A special thank for my longtime office mates André Fischer, Dai-Ning Cho and Alexander Lau for fruitful conversations.

Deutsch:
An dieser Stelle möchte ich mich bei allen Menschen bedanken, die mich in meinem privaten Umfeld immens bei der Fertigstellung dieser Doktorarbeit unterstützt haben. An erster Stelle stehen natürlich meine Eltern (meine Mutti und mein Vati) ohne Zweifel, welchen ich nun vermutlich lange genug mit meinen Problemen in den Ohren gelegen habe. Dann folgt so gleich mein Bruder Thomas, meine Verlobte Anne und ihre Eltern, die so manche arbeitsame und demotivierende Phase meinerseits erdulden mussten. Dann möchte ich mich ebenfalls bei meinen Alltags-“Helden“ bedanken, welche mir zur Mittagszeit in der Mensa oder in einer kleinen Kaffeepause am Nachmittag mit Rat und Tat zur Seite standen: Tom Scheler, Richard Hentrich, Familie Jentschke und Marie-Kathrin Anders.

Eidesstattliche Erklärung

Hiermit versichere ich, dass ich die vorliegende Arbeit ohne unzulässige Hilfe Dritter und ohne Benutzung anderer als der angegebenen Hilfsmittel angefertigt habe; die aus fremden Quellen direkt oder indirekt übernommenen Gedanken sind als solche kenntlich gemacht. Die Arbeit wurde bisher weder im Inland noch im Ausland in gleicher oder ähnlicher Form einer anderen Prüfungsbehörde vorgelegt.

Die vorliegende Dissertation wurde vom 01.11.2012 bis 31.12.2016 am Leibniz-Institut für Festkörper- und Werkstoffforschung Dresden (IFW Dresden), Institut für theoretische Festkörperphysik (ITF) unter der Betreuung von Prof. Dr. Jeroen van den Brink und Dr. Carmine Ortix angefertigt.

Es haben keine erfolglosen Promotionsverfahren in der Vergangenheit stattgefunden. Die aktuelle Promotionsordnung der Fakultät Mathematik und Naturwissenschaften der Technischen Universität Dresden wird anerkannt.

Frank Kirtschig
Dresden, 31. Januar 2017

Frank Kirtschig

Curriculum Vitae

✉ *f.kirtschig@ifw-dresden.de*

Persönliche Daten

Akad. Grad:	Dipl.-Phys.
Geburtsdaten:	02.10.1987 in Dresden, deutsch

Werdegang

1994–1998	**Grundschule**, *142. Grundschule*, Dresden.
1998–2006	**Gymnasium**, *Marie-Curie-Gymnasium*, Dresden.
2006–2007	**Zivildienst**.
2007–2012	**Hochschulstudium**, *Physik*, TU Dresden, Theoretische Festkörperphysik. Themengebiet: Eisenbasierte Supraleiter
Seit 2012	**Promotionsstudium**, *Physik*, TU Dresden, Kondensierte Materie.

Wissenschaftliche Laufbahn

2008–2010	**Studentische Hilfskraft**, *in der Lehre*, TU Dresden. Mathematik und Physik
2011–2012	**Wiss. Hilfskraft**, *Projektarbeit*, IFW Dresden. Themengebiet: Spontane Symmetriebrechung
2012–2016	**Wiss. Mitarbeiter**, *Doktorand*, IFW Dresden. Themengebiet: Topologische Isolatoren